MATERIALS AND DESIGN STRATEGIES FOR SOLAR MICROCELLS

BY

CHRISTOPHER JAMES CORCORAN

DISSERTATION

Submitted in partial fulfillment of the requirements
for the degree of Doctor of Philosophy in Chemistry
in the Graduate College of the
University of Illinois at Urbana-Champaign, 2014

Urbana, Illinois

Doctoral Committee:

Professor Ralph G. Nuzzo, Chair
Professor John A. Rogers
Professor Angus A. Rockett
Professor Andrew A. Gewirth

Abstract

My thesis describes how photovoltaic performance can be improved by careful engineering and incorporation of optical elements and materials external to the devices. These optical elements and materials include periodically nanostructured semi-transparent metallic reflectors that are integrated below microcells, a light trapping structure on the cell's surface, a down-shifting material that coverts ultraviolet light into visible light, as well as optical elements that can spectrum split light between two subcells of different band gaps. The solar cells studied in this work are Si, InGaP, and GaAs solar microcells. Their fabrication and characterization – along with the rationale behind certain design principles –are discussed.

For the case of the periodically structured backside reflector and the surface light trapping structures, Si solar microcells were studied and I was able to demonstrate that in both instances Fabry-Perot resonances trap impinging light inside the Si slab via excitation of cavity modes and are the main photocurrent enhancement mechanism. This was shown through experimental measurements and compared to computational modeling. For each of these systems, significant absorption enhancements were observed in the near infrared — as shown from simplified quantum efficiency measurements and absorption measurements — that agreed with the computational models. For the metallic backside reflector integrated behind a Si microcell, experimental and computational results show that surface plasmons make no significant contribution to the enhanced photocurrent.

For the project discussing the ultraviolet downshifting material, a Eu-based inorganic complex has beneficial effects on the overall cell performance. Experimental measurements on InGaP microcells showed improved performance in the ultraviolet portion of the spectrum where the down-shifting material is active. The mechanisms by which the down-shifting material affects cell performance are reviewed and further improvements to solar devices implementing down-shifting materials are also discussed.

Optical elements such as prisms and dichroic mirrors have previously been employed in spectrum splitting designs. Working with micro-scale solar cells, chromatic aberration can be used to spectrally split the sunlight. In the last part of my thesis, optical modeling results for a prism lens spectrum splitting configuration as well as an aspheric lens with a high degree of chromatic aberration are discussed. Experimental results are presented that show the aspheric lens can be incorporated into a multijunction spectrum splitting solar cell design. Experimental performances for InGaP and GaAs solar cells in a model spectrum splitting device are examined. Finally, a discussion of future directions of photovoltaic research – particularly with III-V materials – is reviewed.

To my family, friends, as well as the sun: for blessing upon all of us the ability to flourish through its astonishing power. Also, thanks for not consuming us yet.

Acknowledgements

Multiple individuals have helped to make this work come to fruition. I would like to thank my advisor Ralph Nuzzo, John Rogers, my committee, as well as my collaborators and group members for challenging me, providing idea generation, problem solving, and inspiration. More specifically, thank you to those whom I have had the pleasure of collaborating with over the course of my time: Hyun-Joong Chung, Debashis Chanda, Ki Jun Yu, Xing Sheng, Junwen He, Mikayla Anderson, Lanfang Li, Somi Kang, and Ling Shen. I would also like to thank Angus Rockett and Matt Meitl for laying the foundation for my understanding of photovoltaics and Mike Hansen and Glenneys Mensing for their invaluable knowledge in microfabrication. Thank you also to my many wonderful friends and family members for all of their guidance and support. Coming here has made me a better person and I have learned a lot and have also had the pleasure of working with some of the most talented and knowledgeable individuals in their respective fields.

To the Nuzzo Group members – Matthew Smalls, Sergio Sanchez, Miguel Casòn, Jason Goldman, Evan Erickson, Enes Oruc, An-Phong Le, Huaibin Zhang, Eric Brueckner, Yuan Yao, Lu Xu, Audrey Bowen, Lanfang Li, Peixi Yuan, Chris Daily, Joselle McCraken, Marvin Malone, David Wetzel, Brittany Rauzan, Annika Elsen, Adina Badea, and others – I can’t think of a better group of people to share a lab space with. I wish you all the best in your future endeavors.

Table of Contents

Chapter 3: Fabrication and Characterization of InGaP and GaAs Solar Microcells under One Sun and Concentrated Light…………………………………………………......87

Chapter 1

An Overview of Photovoltaics and Transfer Printing

1.1 Solar Energy

Everything uses energy. Energy is the currency to do work. For our energy infrastructure, fossil fuels remain the chief source of energy [1]. There are several other energy sources, however, that are ideal for generating power. Figure 1.1 illustrates the reserves for several of these potential energy resources. As reported in the figure, for non-renewables, fossil fuels such as coal, petroleum, and natural gas have estimated reserve amounts of 900 TeraWatts (TW), 240 TW, and 215 TW, respectively [2]. Another potential avenue for power generation comes from uranium which has between 90 – 300 TW of reserves (Figure 1.1), but this is also a finite resource. These sources can only support energy production for a limited amount of time. With current global demand for energy at roughly 16 TW per year [1], and with the expected demand for energy projected to reach roughly 28-40 TW per year by 2050 [1, 2], finite resources are only sustainable for around 100 years [3]. From Figure 1.1, solar energy is chief among renewables – approximately 23,000 TW of light fall to the earth's surface every year. Additionally, the sun also contributes to the other renewable resources. For the case of hydroelectricity, the water cycle of our planet is powered by evaporation, which is the result of solar heating. The water cycle combined with the earth's rotation creates non-uniformities in our atmosphere to produce wind power. Photosynthesis is the result of using energy from photons to convert carbon dioxide into sugars. Besides using hydroelectricity and wind power, solar energy can be utilized through photovoltaic devices which directly convert light into usable energy.

There are other systems such as photothermal and photoelectrochemical systems, but these are beyond the scope of this thesis. This thesis covers photovoltaic systems. For more in-depth discussions of photothermal and photoelectrochemical systems, readers are encouraged to see references [4, 5]. The sections that follow are a brief overview of the operating principles of photovoltaic devices, transfer printing, and micro-scale solar cells. For more in-depth discussions on particular topics which are related to photovoltaics, readers are encouraged to review references [6-9].

1.2 The Photovoltaic Effect: Solar Cells as Bucket-Feeding Water Wheels

Figure 1.2 illustrates a cross-section of a typical III-V solar cell – in this case composed of GaAs. Most solar cells follow a similar scheme: they have passivation on the surface – in this case, it is an InGaP window layer on the front surface. They have a back-surface field (here a highly doped AlGaAs layer) as well as emitter and base layers that form the p-n junction and also serve for photon collection; they also have contacts that collect the current to provide power to an external load. When a solar cell is exposed to a light source, several steps occur to produce an electrical load: (1) light enters the device to generate electron-hole pairs that (2) traverse the depletion region to become majority carriers. After becoming majority carriers they further move across the device to be (3) collected by their respective contacts and flow into the external circuit to power a device. These might sound like abstract ideas. For an analogy that is more intuitive with everyday experiences, the solar cell can be thought of as a bucket-feeding water wheel – as shown in Figure 1.3. In this bucket-feeding water wheel analogy, rainfall is equivalent to the incident sunlight; the pressure head built up inside of the bucket can be thought of as the solar cell's built-in voltage; the water flow through the nozzle is similar to the current a cell produces; and the water wheel output power is analogous to the power a solar cell produces.

The analogy can be extended even further by taking the bucket to have a few leaks. Sidewall and bottom leakage from the bucket can be thought of as recombination occurring at the surface and bulk of the solar cell, respectively. Surface recombination is a major problem in solar cells and passivation techniques must be implemented in order to achieve superior performance. For III-V devices, this is achieved by growing larger band gap materials around the absorber layer [6-8] (the InGaP window layer and the AlGaAs back-surface field for the case of Figure 1.2); while for silicon, this is achieved by using passivation schemes such as silicon nitride or silicon dioxide [9]. Traditional solar cells are usually macroscopic in scale – Si cells can be 5 inches across. As such, passivation is necessary on the top and bottom surfaces of the device, but sidewall passivation is unnecessary since recombination along the edges is negligible.

This bucket-feeding water wheel analogy can be extended even further. In Figure 1.4 there are three possible out-put cases for the bucket-feeding water wheel. In the first, leftmost, case presented in Figure 1.4, the valve on the nozzle can be completely open. This causes a ton of water (current) to flow out of the nozzle, but very little pressure (voltage) is produced since the pressure head is quickly diminished – as can be seen in the lower diagram. Another possibility is to have a valve that is almost restricted completely. This condition, in turn, produces a ton of pressure but no water flow. The water wheel barely moves in this case and the current-voltage curve has an immense voltage, but very little (if any) current. The balance between these two conditions is shown in the rightmost figure. If the valve is partially restricted, optimal pressure and flow can be achieved and the maximum work is produced. This is what researchers strive for in solar cell research – a balance of the two components. Thermodynamics is at play and therefore a balancing act is in order to maximize the system's work to achieve the maximum amount of power. This will be discussed further in the sections that follow.

1.3 Theoretical Limits for Solar Cell Performance and Choice of Materials

Shockley and Quesseir calculated the theoretical thermodynamic limit for solar cell efficiency using a method known as the method of detailed balance [10]. Neglecting material-specific considerations, this calculation considers the solar cell to be a heat engine such that the calculated upper limit of conversion efficiency is allotted by the second law of thermodynamics. From introductory thermodynamics, every ideal process is reversible such that the energy conversion efficiency for the Carnot heat engine is given by

$$Efficiency = \frac{1-T}{T_s} \quad (1.1)$$

where T and T_s are the temperatures of the working environment – in this case the temperature of the solar cell – and the heat source – the sun. Because an actual solar cell cannot collect all of the light since it has specific band gap that restricts light absorption, the projected efficiency limit is not physically obtainable. For the energy that is available, however, there exist non-reversible requirements that must be met to achieve the highest possible efficiency; these are that (1) no resistive losses must be present throughout the device and that (2) there is no non-radiative recombination occurring inside of the solar cell. That is, radiative recombination is the only loss mechanism. At steady state, detailed balance principles dictate that for each frequency of light the rate of excitation and irradiative decay must be equal. Working under these conditions – along with the premise that all energy greater than the band gap of the semiconductor is collected– the upper efficiency limit is a function of band gap energy. A relation of greatest possible efficiency is plotted as a function of band gap in Figure 1.5a.

Even though there are no photovoltaic materials that meet all of the requirements put forth by Shockley and Queisser, certain materials can come close to the ideal model. In order to have a conversion efficiency that is close to the upper theoretical limit, the material must have large carrier mobilities so that all of the carriers reach their respective contacts. The material must have a high degree of spontaneous emission and be close enough to the optimum band gap given in Figure 1.5b – a band gap that is close to 1.1 eV. The plot in Figure 1.5b details external radiative efficiency (ERE), that is, how often radiative recombination (light emission) occurs, at values of 100% (black), 1% (gold), 0.01% (teal), 0.0001% (purple), and 0.000001% (bronze). This figure also uses the AM 1.5G solar spectrum – a more accurate representation of the solar spectrum that will be discussed in greater detail later – rather than approximating the sun as a black body. (Using this solar spectrum – as opposed to a 6000 K black body is what causes the theoretical upper-limit of efficiency to drop from ~ 42 % to ~ 33 %.) The state-of-the-art efficiencies for various solar cell materials are also plotted in the figure. Crystalline GaAs, which has an extremely high ERE, is the most efficient solar cell material to date. Other crystalline materials – Si, InP, InGaP – are also presented. Although crystalline Si is known to have a low ERE, this material performs better than poly- or amorphous-crystalline materials such as CIGS, CdTe, a-Si and organic systems because Si has very large carrier mobilities. A greater value for ERE is desirable for solar energy conversion as light can be better trapped inside of the solar cell. To put it another way, in order to have a high-performing solar cell, a good solar cell must behave like a good light emitting diode. For this reason GaAs has a better energy conversion efficiency than Si.

1.3.1 Key Solar Cell Parameters

Figure 1.6 is an illustrated current-voltage (I-V) curve of a solar cell under illumination. There are four key performance values that are important to solar cells: current, voltage, fill factor, and the device's energy conversion efficiency. The current of a solar cell is given by the following equation [6]:

$$J = J_0\left(e^{qV/ak_bT} - 1\right) - qg_{op}(L_p + L_n) \quad (1.2)$$

From this equation, the current density, *J*, can be partitioned into two parts: the right part is the diode current while the left part is the photocurrent. The solar cell's dark current is expressed by J_0; the dark current stems from the random generation of electron-hole pairs within the depletion region of the device [11]. Going further into the diode current, q is the charge of the electron/hole, V is the voltage applied across the system, k_b is Boltzmann's constant, T is temperature, and a is the ideality factor. The ideality factor can be thought of as a fitting parameter which describes how closely the behavior of a diode compares to the behavior predicted by theory. For more information on the ideality factor, readers are encouraged to see references [6, 9, 11]. From Equation 1.2, the photocurrent portion of the equation, q, is again, the electron/hole charge, g_{op} is the optical generation rate, and L_p and L_n are the minority carrier diffusion lengths. The minority carrier diffusion lengths are determined mainly by the quality of material, the doping profiles, and the surface properties. In essence, each photon absorbed by the solar cell should produce one electron-hole pair for the current. Although it is possible to have multi-exciton generation with higher band gap materials [12], it is best to assume one electron-hole pair per photon.

The voltage corresponding to zero in Figure 1.6 is known as the open-circuit voltage (V_{oc}). This is represented by Equation 1.3, where [11]:

$$V_{oc} = \frac{nk_bT}{q}\ln\left(\frac{J_{sc}}{J_0} + 1\right) = \frac{nk_bT}{q}\,ln\left\{\frac{L_p+L_n+W}{\left(\frac{L_p}{\tau_p}\right)p_n+\left(\frac{L_n}{\tau_n}\right)n_p}g_{op} + 1\right\} \quad (1.3)$$

Here, a, k_b, T, q, L_p, and L_n, represent the aforementioned terms in Equation 1.2. The new terms, p_n, n_p, τ_p, τ_n, and W are the minority carrier concentrations and life times for the different carriers, and W is the width of the junction, respectively. A more interesting and meaningful relation to voltage is shown in Equation 1.4 [13, 14]:

$$V_{oc} = \frac{E_g}{q}\left(1 - \frac{T}{T_{sun}}\right) + \frac{kT}{q}\left\{ln\left(\frac{\Omega_{emit}}{\Omega_{sun}}\right) + ln\left(\frac{4n^2}{I}\right) - ln(QE)\right\} \quad (1.4)$$

where this equation is partitioned into parts. These different parts represent different loss mechanisms for the voltage. For example, why does the champion silicon solar cell of ~ 25% efficiency [15] only have an open-circuit voltage of 0.77 V as opposed to being closer to 1.1 V – silicon's band gap? Equation 1.4 can explain the reasons for these discrepancies. The first part of this equation explains how the band gap of the semiconductor (E_g) can be related to voltage losses that are based upon Carnot's theorem. Here, T is temperature of the cell and T_{sun} is the temperature of the sun, as discussed previously. There is roughly a 12% loss in voltage based upon this expression. The next expression containing Ω_{emit} and Ω_{sun} explain an increase in entropy for the system upon absorption and emission of light. Ω_{emit} and Ω_{sun} are the emission angle of light from the solar cell and absorption angle for light coming from the sun, respectively. Based upon Kirchoff's law, a substance that absorbs light can also emit light [16, 17]. Because most of the light absorbed by a solar cell usually comes from direct photons that have a very specific emission angle (~ 0.25°) [18] from the sun, once photons can be emitted from the device, they can be emitted from 360 degrees. Thus, an increase in entropy in the system is produced. The loss associated here can be considered the "loss of directivity information" and is associated with up to a 300 mV penalty [14]. The next portion associates voltage losses with incomplete light trapping. The $4n^2$ term in the numerator, where n is the refractive index of the material, is the maximum number of passes light can have inside of a solar cell before escaping. This $4n^2$ term is known as the Yablonovitch limit and for silicon it is taken to be roughly 50 [19]. The term in the denominator, I, is the intensity of light inside the solar cell. Once the $4n^2$ term approaches the possible allotted amount of sunlight for light trapping, this fraction goes to unity and little to no loss in voltage occurs. Because all of the light can never perfectly be trapped, however, there are associated losses. The loss can be up to 100 mV, but is usually not this significant [14].

The last part of this equation, QE, represents the radiative emission quantum efficiency of the device. More specifically, this last term accounts for losses in V_{oc} that are due to non-radiative processes. The quantum efficiency, QE, for radiative recombination is defined to be $QE = R_{rad} / (R_{rad} + R_{non\text{-}rad})$ where the R_{rad} and $R_{non\text{-}rad}$ terms are radiative and non-radiative recombination rates, respectively. Aspects such as material purity must be considered here. These processes occur because of traps in the bulk of the device as well as other effects such as recombination at the surface and other interfaces that can result from crystallographic defects or impurities inside of the device. More on this will be discussed in the *Solar Cell Loss Mechanisms* section. If a solar cell, for example, is not of high-material quality or does not have adequate surface passivation (think of it as a very leaky bucket), the voltage can be lowered significantly – by as much as 300 mV [14]. Solutions to these problems include working with materials of electronic-grade purity as well as very highly luminescent materials – such as GaAs. This is one reason why Si – indirect bandgap of 1.1 eV – cannot exceed an energy conversion efficiency of over 25%. The QE of Si is typically well below 10% whereas a material like GaAs has a much higher QE and, therefore, can offer greater improvement. For example, GaAs has always had its V_{oc} stuck at ~1.0 V. More recently, from incorporating improved light-trapping designs in conjunction with GaAs devices and exploiting its extremely high luminescence, its V_{oc} has been improved by 100 mV – a very substantial improvement [20].

The above was a discussion of the open-circuit voltage. The voltage at which a solar cell operates at its maximum power, known as the operating voltage, is given in the equation below [6]:

$$V_{op} \sim V_{oc} - \frac{kT}{q} \ln\left(\frac{qV_{oc}}{k_b T}\right) \quad (1.5)$$

where V_{op} is the operating point voltage and all the terms listed above have already been discussed. The $ln(qV_{oc}/k_bT)$ term is around 100 mV. This term can be thought of as the energy that must be given up in order to have the electron-hole pairs move through the solar cell to the contacts. This is thermodynamics at work and all this equation explains is that you cannot have everything. A solar cell cannot have its highest possible voltage and current simultaneously. Think of the bucket analogy discussed in the previous section. There is a balance between voltage and current occurring at the maximum power point. The $ln(qV_{oc}/k_bT)$ term strikes a compromise with the system so that it generates the most power and from this point, the performance can only get worse – Figure 1.6).

Another parameter, known as the fill factor of a solar cell, is the ratio of a device's maximum power point to its open-circuit voltage and short-circuit current. Since the aforementioned terms are rooted in thermodynamics, the fill factor also has a thermodynamic background. This ratio can be thought of as a thermodynamic parameter rather than an electrical parameter. Because it is a thermodynamic parameter, it will never exactly be 1, but it can come very close. Some of the best lab cells to date have fill factors in the mid to upper 80s [21].

The last parameter associated with solar cells is the device's energy conversion efficiency – which is given as

$$efficiency = \frac{maximum\ power\ point}{illumination \times area} = \frac{FF \times V_{oc} \times J_{sc}}{illumination \times area} \qquad (1.6)$$

Where the power output by the solar cell, the cell's fill factor (*FF*), V_{oc}, and J_{sc} are divided by the illumination power and the area being measured. For standard test conditions in a lab with flat-plate devices, the AM1.5G spectrum is used. This spectrum has an input power density of ~1,000 W/m^2.

1.3.2 Solar Cell Loss Mechanisms

Despite the method of detailed balance suggesting that single junction solar cells can be capable of achieving energy conversion efficiencies greater than 30%, real-world devices experience unavoidable losses that limit performance. Figure 1.7 is an illustration of an energy band diagram of a p-n junction solar cell with all of the major energy conversion losses outlined. The major loss mechanisms are the following [6, 7]:

1. Non-absorption of photons below the band gap of the solar cell.
2. Thermalization losses that arise due to the photons possessing an energy greater than the band gap of the solar cell.
3. Junction voltage losses from the band edge to the quasi-Fermi level.
4. Voltage loss as a consequence of the contacts being in higher or lower energy than the semiconductor.
5. Recombination losses such as Auger, Shockley-Read-Hall, or radiative recombination.

Processes 1 and 2 are a consequence of the cell's band gap not being the same energy as that of the photon. Processes 3 and 4 are voltage losses associated with going from the band edge to the quasi-Fermi level and can be measured with the ratio of V/E_g [22]. Process number 5 consists of the mechanisms which dictate the open-circuit voltage of the device and consist of three loss mechanisms. Processes 1, 2, and radiative recombination associated with process 5 are all intrinsic and cannot be overcome.

For the short-circuit current of a solar cell, the two main losses for achieving the highest possible theoretical current come from optical and recombination losses. The optical losses include an imperfect anti-reflection coating and incomplete absorption of light from below band-gap photons. For the recombination losses, which are the losses that limit a cell's open-circuit voltage, there are Auger, Shockley-Read-Hall, or radiative recombination. Shockley-Read-Hall recombination occurs when there are defects in the semiconductor. For this process, a carrier becomes trapped in a forbidden energy state in the band structure as a result of a defect. These defects can occur through doping, not using a single crystalline material, or from the surface and sidewalls of the cell having dangling bonds resulting from inadequate passivation. Radiative recombination is prevalent in direct band gap materials and is the process governing the operation of light-emitting diodes. In this process an electron from the conduction band directly recombines with a hole that is in the valence band causing a photon to be released. This emitted photon is similar in energy close to the band gap of the semiconductor and is only, therefore, weakly absorbed. For Auger recombination, an electron and a hole recombine. Rather than emitting the energy as photon – as in the case of radiative recombination – or as heat, the energy is transferred to another carrier that is close by. For example, this energy can be transferred to an electron. After transfer of the excess energy, this electron will be in a higher state and thermalize back down to the band edge of the semiconductor. Methods for overcoming these problems include working with thin-film materials of high purity as well as adding light trapping structures to extend the path length of light inside of the cell as demonstrated by the Yablonovitch group [23]. The amount of recombination going on in a particular material can be estimated with a calculator from reference [7].

1.4 Sunlight and Laboratory Testing Conditions

The sun at the center of our solar system has an emission spectrum that can be roughly approximated as a blackbody at 6,000K [9]. As sunlight travels from space to our atmosphere, portions of the spectrum are absorbed from the molecules in the air. For example, the UV light is filtered by the ozone and the higher-energy photons are more effectively scattered as a result of Rayleigh scattering. The solar intensity in the middle of the day at the equator is taken as a reference point with an intensity of roughly 1,000 W/m^2. A global average was created that is known as the AM 1.5 G solar spectrum (Figure 1.8a); this spectrum takes into account both direct and diffuse photons. Depending on the panels position on the planet, it can see different fluxes of direct and diffuse photons, however, to a rough approximation, on a clear day, 30% of sunlight is in the form of diffuse photons while 70% of sunlight is from direct photons. Another spectrum has been developed known as the AM 1.5 D spectrum which only has direct sunlight. Because diffuse photons cannot be focused, for testing concentrator systems, the AM 1.5D spectrum is typically employed. For testing devices in a laboratory environment, sun light is typically simulated with a Xenon arc lamp. This small light source typically consists of well-collimated light with proper air mass filters to help closely mimic the sun’s spectral emission. The simulated AM1.5 G spectrum is plotted in Figure 1.8b. Current density-voltage measurements reported in this thesis were made under air mass 1.5D or 1.5G illumination under standard test conditions that were calibrated to 1000 W/m^2 (Oriel, Model 91192) at room temperature (~25°C) with a source meter (Keithley, model 2400) using a Si reference cell for calibration of the simulator (Newport-Oriel, model 91150V). For our particular similar, the light size is 10.2 x 10.2 cm^2 in area. The collimation of the simulator is +/- 4° which is ideal for testing flat plate devices.

1.5 The Value of Improved Solar Cell Conversion Efficiency – The Nominal Cost of Solar Electricity

Despite solar energy being the most abundant renewable energy resource, energy production from photovoltaics represents only a small fraction of the overall energy landscape. Worldwide installation capacity of solar energy is nearly at 100 GWp (giga watt-peak) when it was virtually non-existent back in 1992 [24]. (Note: Wp, or Watt-peak, is the amount of energy a photovoltaic system can produce under standard test conditions as discussed above.) The main reason for solar cells not having a large share of the energy landscape – albeit the market is growing rapidly with each passing year – is that the cost of generating electricity from solar cells is still typically higher than from traditional energy sources such as coal and natural gas. There will most likely be some point in the future where grid parity can be reached given the fact that the retail cost of conventional electricity is rising while the cost for solar electricity continues to fall [8, 25]. In order to compare costs of energy from different sources, the leveled cost of electricity (LCOE), which gauges the lifetime energy production and system costs, is used to compare various energy sources. The most basic equation links the LCOE with several factors as represented by the equation [20]:

$$Cost\ of\ electricity\ \propto \frac{cost_{module}+cost_{balance-of-system}}{insolation \times efficiency} \times finance + operating \quad (1.7)$$

Here $cost_{module}$ is the cost of the module; $cost_{balance\text{-}of\text{-}system}$ are the costs such as wiring and other parts directly related to the module; insolation is the amount of sunlight falling on the system; efficiency is the energy conversion efficiency of the device; finance are financing options that are available; and operating are the costs associated with operating the system over its lifetime. As we can see from Equation 1.7, insolation and efficiency are inversely related to the cost of electricity. Therefore, there is improved benefit in increasing the energy conversion efficiency of photovoltaic devices. Insolation, on the other hand, various by region of where the panel is installed; for example, there will be more light per year in Tucson, AZ than in Chicago, IL. A more through treatment can be used to give a more accurate picture of LCOE. The LCOE is defined as [26]

$$LCOE = \frac{PCI - \sum_{n=1}^{N} \frac{DEP + INT}{(1+DR)^n} TR + \sum_{n=1}^{N} \frac{LP}{(1+DR)^n} + \sum_{n=1}^{N} \frac{AO}{(1+DR)^n}(1-TR) - \frac{RV}{(1+DR)^n}}{\sum_{n=1}^{N} \frac{\text{Initial kWh} \times (1-SDR)^n}{(1+DR)^n}} \quad (1.8)$$

Included in Equation 1.8, but not in Equation 1.7 are factors such as PCI, which is the project cost minus any investment tax credit or grants; DEP is depreciation, INT is interest paid, LP represents loan payment, TR is the tax rate, DR is the discount rate, AO is annual operations costs, RV is the residual value, and SDR is the system degradation rate. Traditionally, a system can degrade in efficiency each year depending on where the device is installed [27]. Using Equation 1.8, Darling et. al. used Monte Carlo simulations to estimate the LCOE for photovoltaic panels in Chicago, Boston, and Sacramento. Table 1.1 lists the mean, median, standard deviation, and variance. These results are quite thorough and shed light on the cost of electricity for the lifetime of a device. As a general rule-of-thumb to estimate current costs, Si PV modules cost ~8 cents/kWh. Prices will continue falling annually. As pointed out by Richard Swanson of SunPower, the price of photovoltaic modules drops by ~20% for every doubling of product shipped [25]. The price of a silicon module has already dropped below \$1.00/W_p [24, 28]. Methods for reducing the costs of these panels further exist. For example, using less material or further improvements in energy conversion efficiency will lower the cost of photovoltaic panels. These are the main goals of research into solar energy: finding methods to (1) reduce the cost of solar while maintain or (2) exceed current device performance.

1.6 Transfer Printing of Micron-Sized Inorganic Electronic Elements

Transfer printing is a technique whereby a viscoelastic stamp is used to transfer elements from a donor substrate onto a receiving substrate and has practical application in solar energy and the electronics industry as a whole. More specifically, for application in solar energy, solar cells can be processed on a wafer and undercut to be transferred to foreign substrates. Here, a viscoelastic stamp is brought into conformal contact with the electronic elements and removed from the host substrate to be transfer printed. The stamp most typically used is polydimethylsiloxane (PDMS, Dow Corning Sylgard 184). This polymer is commercially purchasable and can be made within hours. After synthesis, it has a very long shelf-life; from personal experience, the stamps can be reused multiple times and can last for years. Transfer printing with a stamp relies upon van der Waals interactions in order for the electronic elements to adhere to the stamp. Studies have been performed to investigate the competing modes of fracture for device/PDMS/donor- and receiving-substrate systems [29, 30]. The adhesion between electronic elements and the stamp is dependent upon the rate at which the stamp is removed from the donor substrate. For example, if a high peeling velocity is applied to the stamp/device system, adhesion between these two interfaces is strong enough to lift the electronic elements off of the donating wafer. Once the “inked” stamped is brought into contact with a receiving substrate, a lower peeling velocity can be applied to generate weaker adhesion between the stamp/device to transfer the electronic elements off of the stamp. When the stamp is initially peeled away from either substrate at a speed *v*, there is a characteristic energy release rate, *G*, governed by [29]:

$$G = \frac{F}{w} \quad (1.9)$$

where *F* is the peel force and w is the width of the element. This equation takes into account the interfacial bond breaking as well as the viscoelastic dissipation along the tip of the fracture [29]. The fracture propagates once *G* reaches some critical energy release rate such that two competing fracture paths occur: either pick-up off of the donating substrate or printing onto the receiving substrate.

The critical energy release rate for the interface at the element/substrate is given as $G_c^{element/substrate}$, which is a property of the material of this interface and is not influenced by the peeling velocity. The critical energy release rate $G_c^{stamp/element}$ for the stamp/element interface, however, is dependent upon the peeling velocity and is given as

$$G_c^{stamp/element} = G_c^{stamp/element}(v) \quad (1.10)$$

Device pick-up off of the donor substrate occurs when the forces for pick-up are greater than the forces for printing such that

$$G_c^{stamp/element} > G_c^{element/substrate} \quad (1.11)$$

The process for transfer printing occurs when the forces for printing are greater than the forces for pick-up

$$G_c^{stamp/element} < G_c^{stamp/element} \qquad (1.12)$$

In actual practice, anchors of some sort hold the substrate to be transferred onto the donating substrate, so these forces must be taken into account as well. Regardless, it is possible to achieve lift-off from the donating substrate with photoresist and other anchors by tailoring stress focusing for controlled fracture [31]. For transferring objects to receiving substrates, if the back-surface of the element to be transferred and the top surface of the receiving substrate are flat enough – usually on the order of atomic roughness – van der Waals forces can adhere the substrates together. Functionalizing the surfaces to form covalent bonds [32] can also improve adhesion. In practice, because most surfaces being transfer printed to are not atomically flat, commercially available organic adhesives – such as SU-8 and NOA (Norland Optical Adhesive) – are often employed for placing elements on receiving substrates. It is also possible to tune the adhesive properties of the stamp by chemically treating it in ultra-violet/ozone or oxygen plasma to make the surface more "glassy" or by having microscopic structures on the stamp that can weaken the adhesive forces between the PDMS stamp and inked devices [33, 34].

1.7 Micro-Scale Solar Cells

Traditional photovoltaic technologies tend to be macroscopic in size. Silicon solar cells in modules are inches in diameter and laboratory test cells tend to be on the order of centimeters [21]. Traditional technologies are usually on the order of hundreds of microns in thickness. When the thickness of a solar cell is reduced, collection of the free carriers is improved. For example, there are decreases in instances of bulk recombination with thin-film solar cells.

Provided that there is adequate absorption of light, thinner cells lead to better short-circuit current and open-circuit voltage parameters – improving the overall energy conversion efficiency. Recently, investigations have turned to micro-scale solar cells [35-38]. The solar technologies examined in my research as well as a good body of work coming out of the University of Illinois have explored III-V devices and silicon solar microcells. Miniaturization of these devices is attractive due to more efficient materials utilization as well as their potential achieve high energy conversion efficiencies. Additional benefits from these devices are their ability to be mechanically flexible and lightweight which opens up opportunities for new and unconventional applications with novel fabrication and integration techniques. In the realm of concentrators, working with thin-film, micro-scale devices uses such little material and offers improvements in thermal management over conventional concentrator systems – making it unnecessary to install heatsinks on solar cells [39-41]. All of these advantages lead to high-performing devices that have lower costs than traditional concentrator systems.

There are also drawbacks for having micro-scale (length and width) devices. Without adequate surface and sidewall passivation, the increased cell surface-area-to-volume ratio will result in more recombination events along the surface and side walls of the device. Going back to the bucket-feeding water wheel analogy, this cell will behave as a leakier bucket – when compared to cells of greater area – compromising the energy conversion efficiency. There is some optimum size that offers a balance between these competing mechanisms [42] as well as remedies to these problems. For silicon, passivation on the surface and sidewalls with silicon dioxide or silicon nitride reduces carrier recombination and will solve issues with surface recombination [9]. For thin-film, compound semiconductors like GaAs grown by metal-organic chemical vapor deposition, passivation on the front and back surfaces of the cell is already accomplished with wider band gap materials [6-8]. For sidewall passivation, reports have shown that monolayers of organic molecules can reduce the number of dangling bonds so there is less compromise to performance [43]. In concentration systems where the cells can be potentially working in the high-carrier injection limit; that is, when the amount of generated carriers is greater than the background dopant concentrations, the primary method of recombination becomes Auger recombination and sidewall recombination becomes negligible. For this reason, micro-cells under concentrated sunlight are an attractive alternative to their bulkier counterparts. From this discussion, by careful engineering of the cell with adequate passivation and paying careful attention to the surface-area-to-volume ratio of the device, micro-cells can be an excellent source for power generation.

1.8 Concentration Photovoltaics

From earlier discussions, some of the work in this thesis involves cells under concentration. Therefore, a brief overview of concentration is necessary. Higher energy conversion efficiencies can be obtained when solar cells are exposed to concentrated sunlight. From Equation 1.2, the photocurrent of a solar cell is proportional to the intensity of light; and from Equation 1.3, the open-circuit voltage increases logarithmically with light intensity. A modified version of Equation 1.3 can be represented as [6]

$$V_{oc} = \frac{nk_bT}{q}\ln\left(\frac{XJ_{sc}}{J_0}+1\right) = \frac{nk_bT}{q}\left[\ln\left(\frac{J_{sc}}{J_0}+lnX\right)\right] = V'_{oc} + \frac{nk_bT}{q}lnX \qquad (1.13)$$

Here X is the concentration level represented in suns. This equation states that the power produced from a solar cell rises linearly under concentrated sunlight and, therefore, the efficiency of the solar cell increases as well. Under lower levels of concentrated sunlight the *FF* increases with concentration because of the higher V_{oc} values. At much greater levels of concentrated sunlight, however, resistive effects occur and begin to limit *FF* values. These resistive losses are proportional to the second power of the photocurrent since

$$Power = I^2R \quad (1.14)$$

Where I is the current and R is the resistance.

There is also the problem with heat dissipation for solar cells in concentrated sunlight. It is known that the operating temperature increases for solar cells in a concentration system. The band gap energy of a semiconductor decreases with increasing temperature, as described by an empirical expression outlined by Varshni [44]. The numerical expression for the a given band gap (E_g) as a function of temperature is

$$E_g(T) = E_g(0) - \frac{\alpha T^2}{T+\beta} \quad (1.15)$$

Where $E_g(0)$, α, and β are material constants. From this expression, the short-circuit current density marginally increases with elevated temperature, but the open-circuit voltage and fill factor decrease. As a result of these trends under higher temperatures, overall device energy conversion efficiency decreases [45, 46].

The idea for concentrating light onto solar cells has been around for a very long time [47]. In a concentrator system, only a small area of material is used and the large collecting area originally taken up by a flat-plate module is replaced by cheaper concentrating optics. Therefore concentration has the benefit of (1) using a smaller amount of solar material and (2) improving cell efficiencies. These aspects also allow for the use of higher efficiency cells that would otherwise be cost-prohibitive in flat-plate modules. For example, it is now possible to operate at concentration ratios of 500 or even 1100 suns and the most efficient modules to date are rated at

35.5% power conversion efficiency [48]. Figure 1.9 shows images of two types of concentrators where the module in (a) uses a large, reflective dish to focus light onto the cell and the module in (b) uses Fresnel lenses to focus sunlight onto the cells. These are the two main types of optical elements – that is, reflective and refractive – used for concentration in commercially available systems. There exist other types of concentrating elements – such as the compound parabolic concentrator and other ideas proposed by the non-imaging optics community [18] as well as luminescent dye concentrators [49-51] which are able to capture both direct and diffuse photons. The luminescent dye concentrators are still more academic concepts and have only been able to produce modest concentration results.

Because concentrators only collect the direct irradiance, the modules have to track the sun with a high degree of accuracy. This has the added benefit of always getting the maximum power output from solar cells and these systems are also able to meet peak power demands as shown in Figure 1.10. (Note: flat-plate modules can also achieve this feat since peak load to the grid occurs around noon – the time when the sun is generally above flat-plate modules. Concentrators, however, have the added benefit of always actively tracking the sun.) Additionally, for the case of very sunny climates, this figure demonstrates another benefit from concentrator systems: two-axis tracking concentrators produce a greater amount of power than their flat-plate counterparts [52]. While only collecting the direct irradiance, concentrators can still produce a good amount of power even in somewhat cloudy environments. For example, it was found that concentrator systems receive ~80% of the insolation of flat plate modules in Boston, a place known for having a moderately cloudy climate [47]. As solar cell efficiencies continue to improve, the LCOE will continue to fall and concentrators will begin to have a market. Devices utilizing concentrators will never be the entire photovoltaic business, as flat-plate modules will never be the entire photovoltaic business. Concentrators using high-efficiency solar cells will never be beaten for low-cost and medium to large-scale power for areas with a high degree of insolation [47].

1.9 Overview of Dissertation

This chapter has been an extremely brief overview of photovoltaics. Photovoltaic devices are an appealing alternative energy source and the fundamental physics of light extraction and electronic performance have been discussed. Chapter 2 will discuss how light trapping techniques can be applied with backside reflectors and surface light-trapping structures to increase the absorption of light and produce better-performing silicon-based solar cells. Chapter 3 presents fabrication strategies for GaAs and InGaP solar micro-cells by using the epitaxial lift-off technique and the guiding principles with which to design these compound semiconductor microcells and their results. Chapter 4 demonstrates how down-shifting can be used to improve photon management in solar cells. Chapter 5 discusses spectrum splitting as a means for improving overall module performance by more effectively managing light to ensure that light selectively hits solar cells that have an optimum band gap for energy conversion.

1.10 Figures and Tables

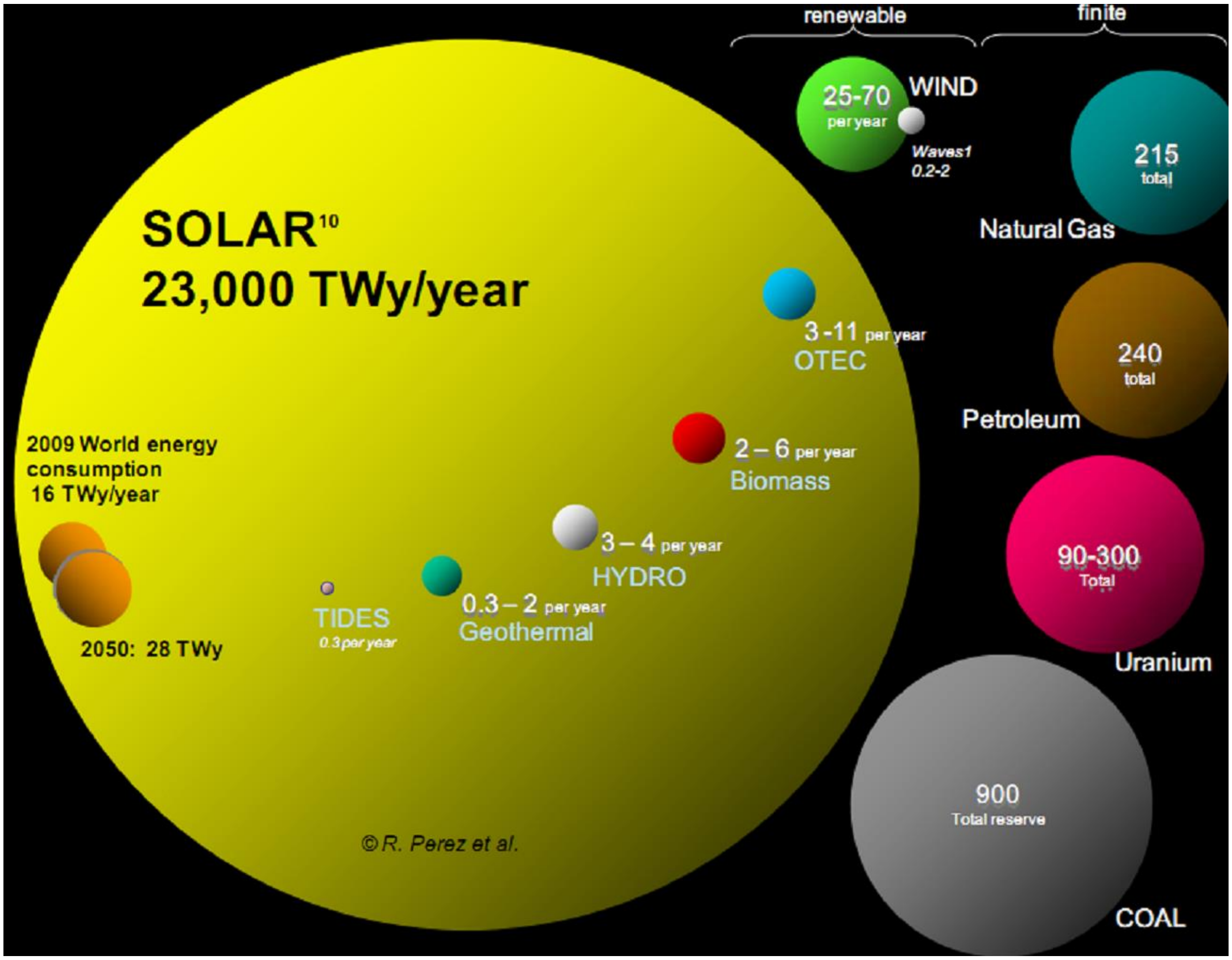

Figure 1.1 World energy consumption from 2009 and projected energy consumption in 2050 (bronze circles) in comparison with various renewable and non-renewable energy sources. Figure is adapted from reference [1].

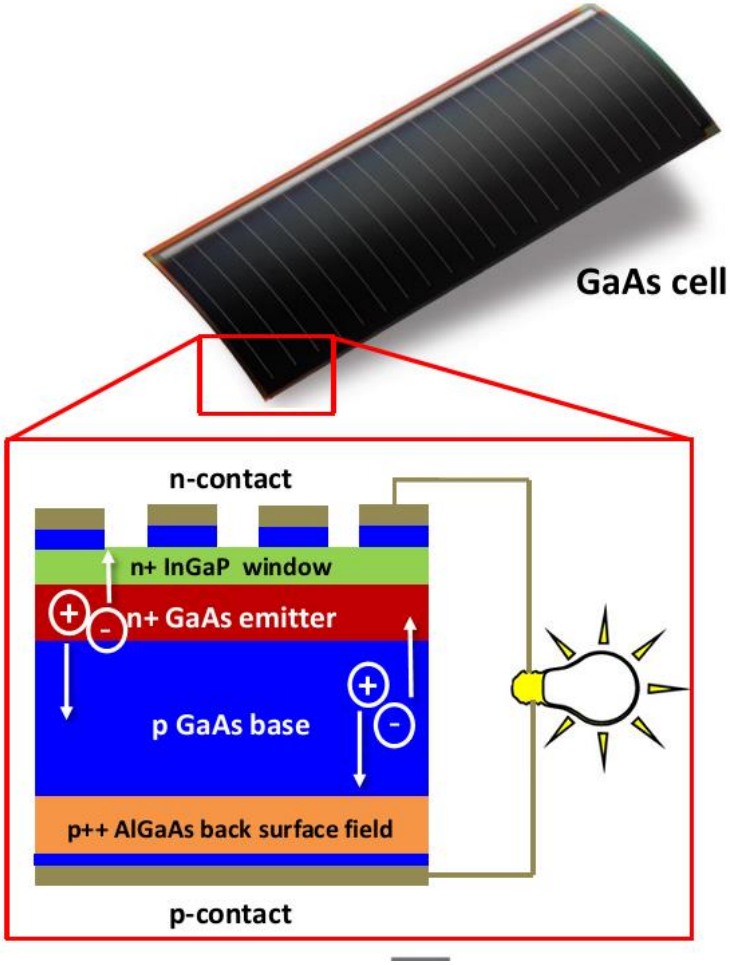

Figure 1.2 Image of a mini solar module as well as the schematic of a solar cell outlining the contacts, window, emitter, base, and back-surface field layers of the solar cell. Image of the mini solar cell is adapted from reference [53].

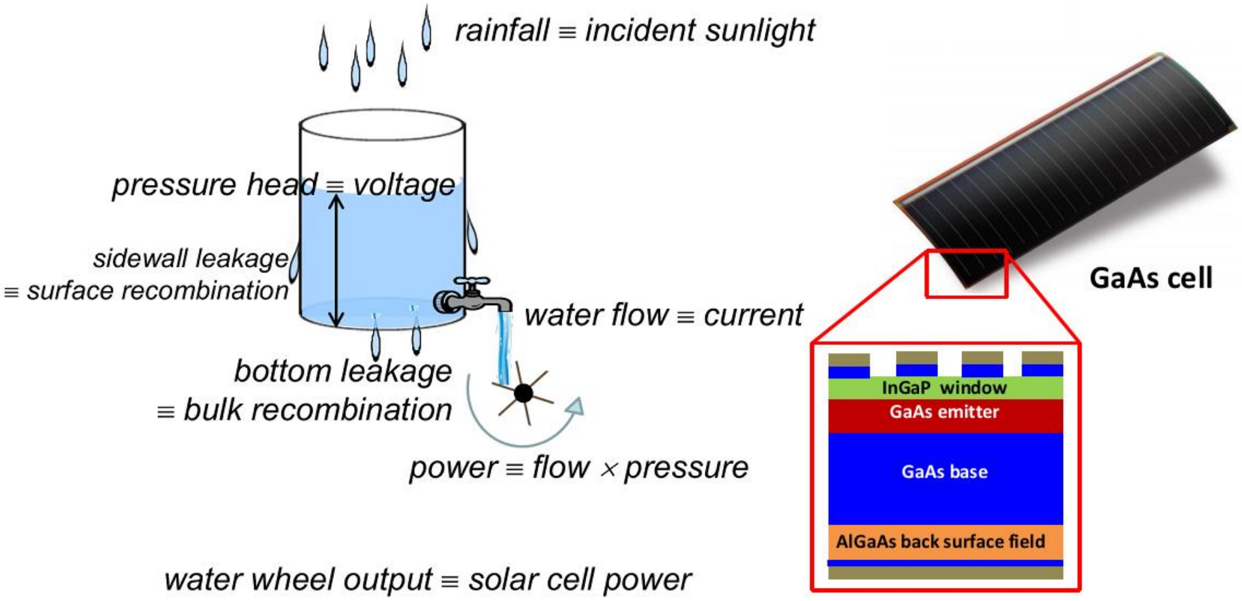

Figure 1.3 Outline of a solar cell as a bucket-feeding water wheel. Image is adapted from references [20, 53].

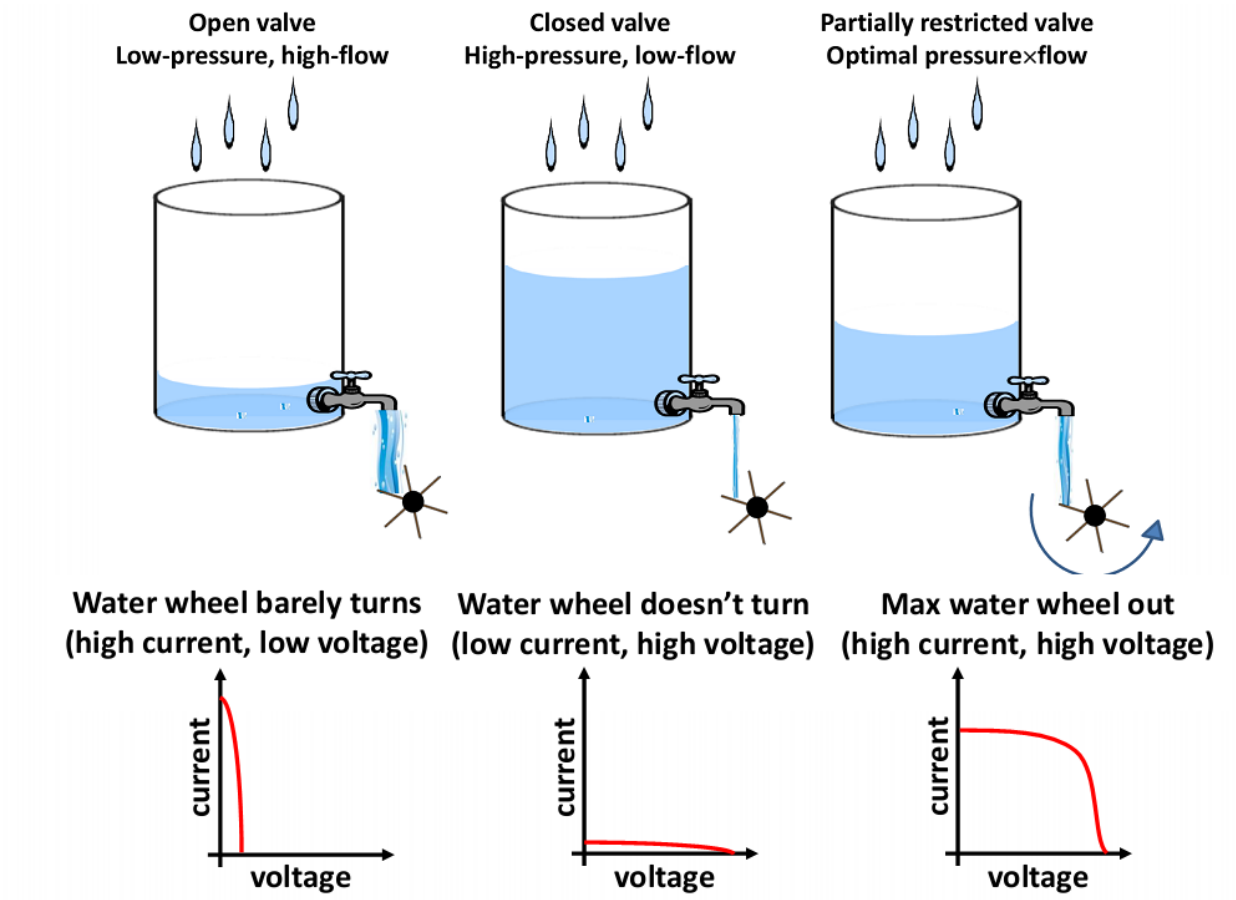

Figure 1.4 The solar cell bucket-feeding water wheel analogy extended further showing the three possibilities with their respective current-voltage curves: high current and low voltage (far left), low current and high voltage (center), and high current and high voltage (right). Image is adapted from reference [20].

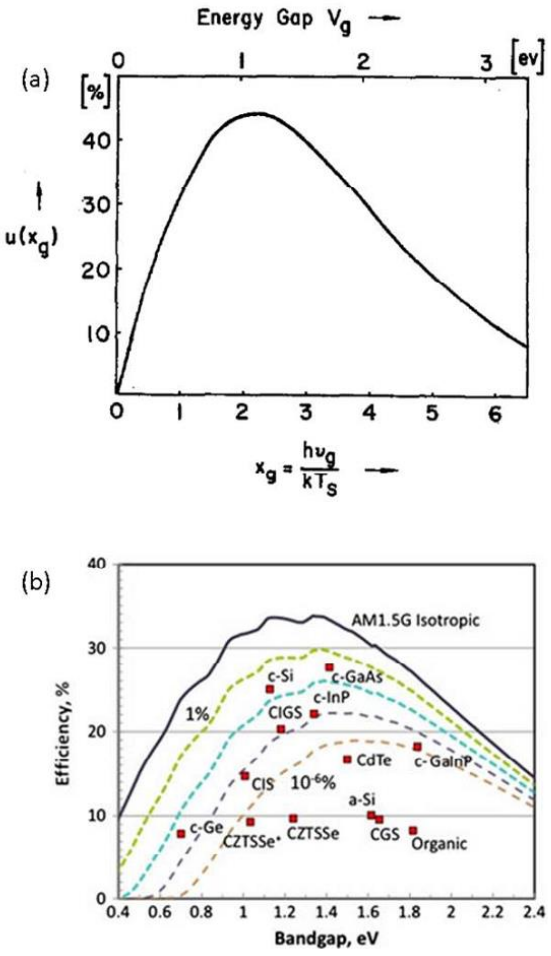

Figure 1.5 Thermodynamic limits for energy conversion efficiency of solar cells at various band gaps as defined by the Shockley-Queisser limit (a) and Shockley–Queisser limits on the efficiency of conventional single-junction cells as well as limits for cells of 1% (gold), 0.01% (teal), 0.0001% (purple), and 0.000001% (bronze) external radiative efficiency values. Figure is adapted from references [10, 54].

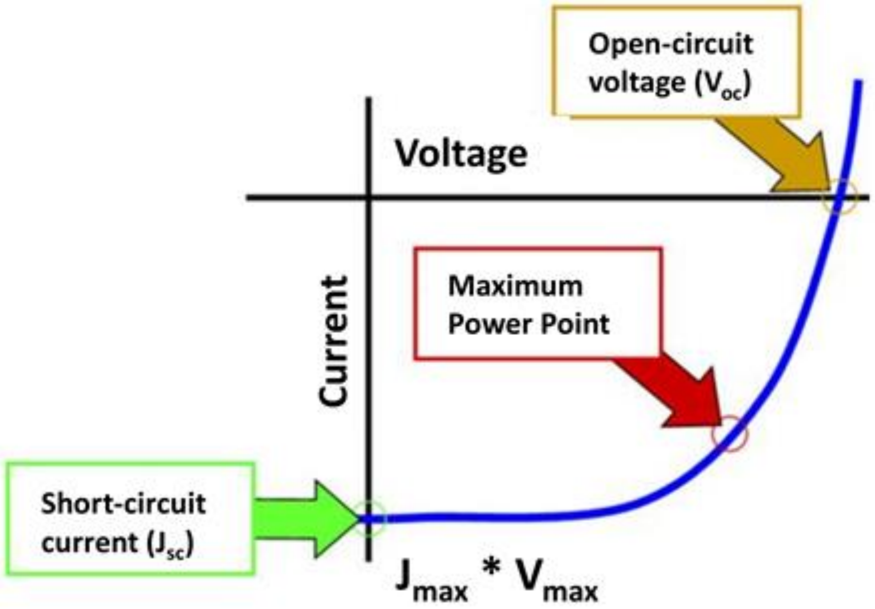

Figure 1.6 Solar Cell I-V curve depicting the short-circuit current (green), the open-circuit voltage (bronze), and the maximum power point (red). Figure is adapted from reference [55].

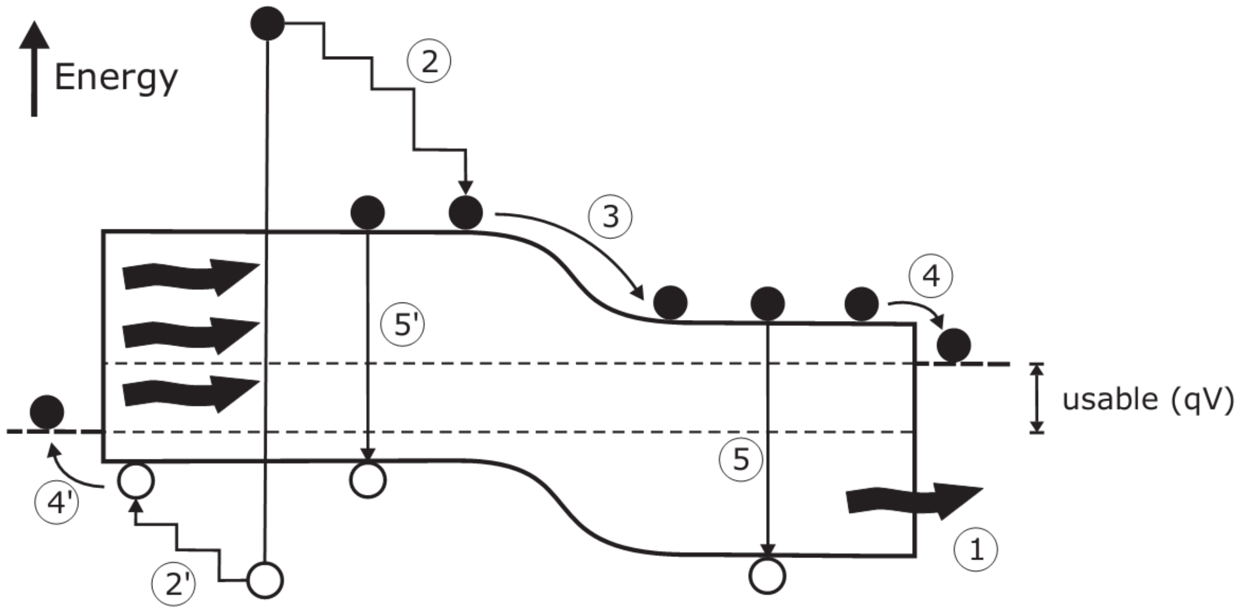

Figure 1.7 Energy conversion loss processes outline for a one-junction solar cell where the losses are due to lattice thermalization (1), junction losses (2), contact losses (3), recombination losses (4), and insufficient capture of photons below the cell’s band gap (5). Figure taken from reference [22].

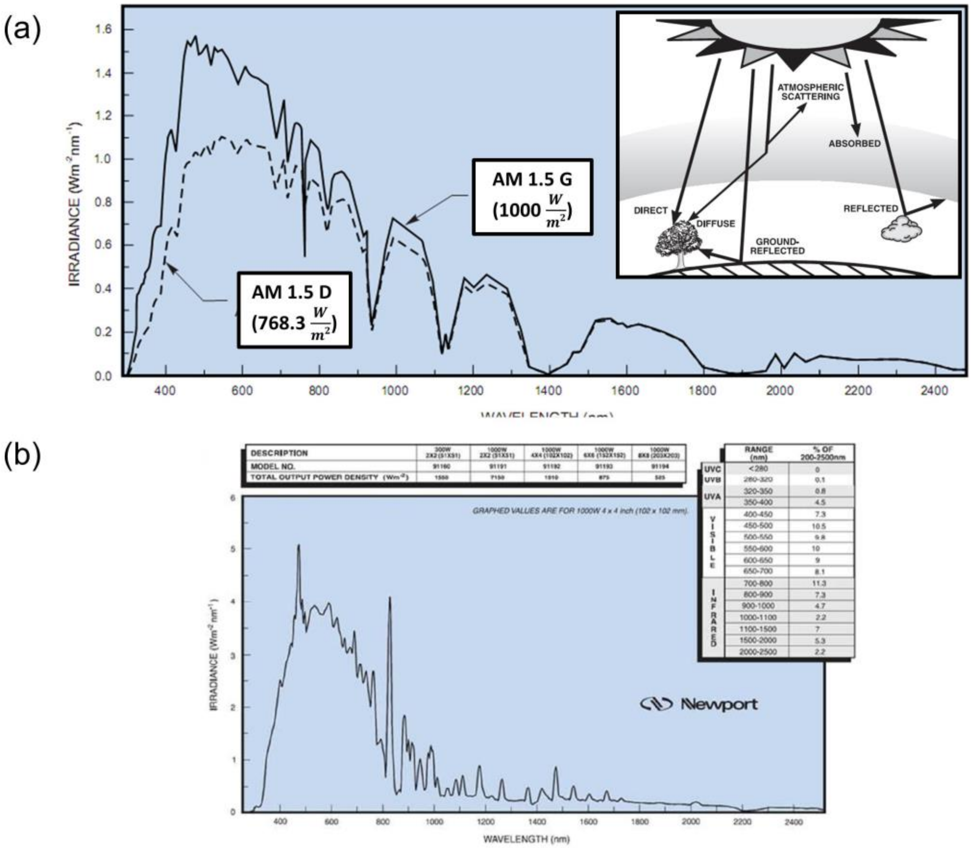

DESCRIPTION	300W 2X2 (51X51)	1000W 2X2 (51X51)	1000W 4X4 (102X102)	1000W 6X6 (152X152)	1000W 8X8 (203X203)
MODEL NO.	91160	91191	91192	91193	91194
TOTAL OUTPUT POWER DENSITY (Wm⁻²)	1550	7150	1910	875	585

	RANGE (nm)	% OF 200-2500nm
UVC	<280	0
UVB	280-320	0.1
UVA	320-350	0.8
	350-400	4.5
VISIBLE	400-450	7.3
	450-500	10.5
	500-550	9.8
	550-600	10
	600-650	9
	650-700	8.1
INFRARED	700-800	11.3
	800-900	7.3
	900-1000	4.7
	1000-1100	2.2
	1100-1500	7
	1500-2000	5.3
	2000-2500	2.2

Figure 1.8 The AM 1.5 G and 1.5 D solar spectrums used for characterizing solar cells (a) and a reference spectrum from a solar simulator using a xenon bulb (b). Figures are taken from reference [56].

Parameter	Boston	Chicago	Sacramento
Mean	9.3	9.7	6.9
Median	9.1	9.4	6.7
Std. Dev.	2.7	2.8	2.0
Variance	7.1	7.8	3.8

Table 1.1 Statistics from LCOE output calculations for three different cities (all units are ¢/kWh). Table is adapted from reference [26].

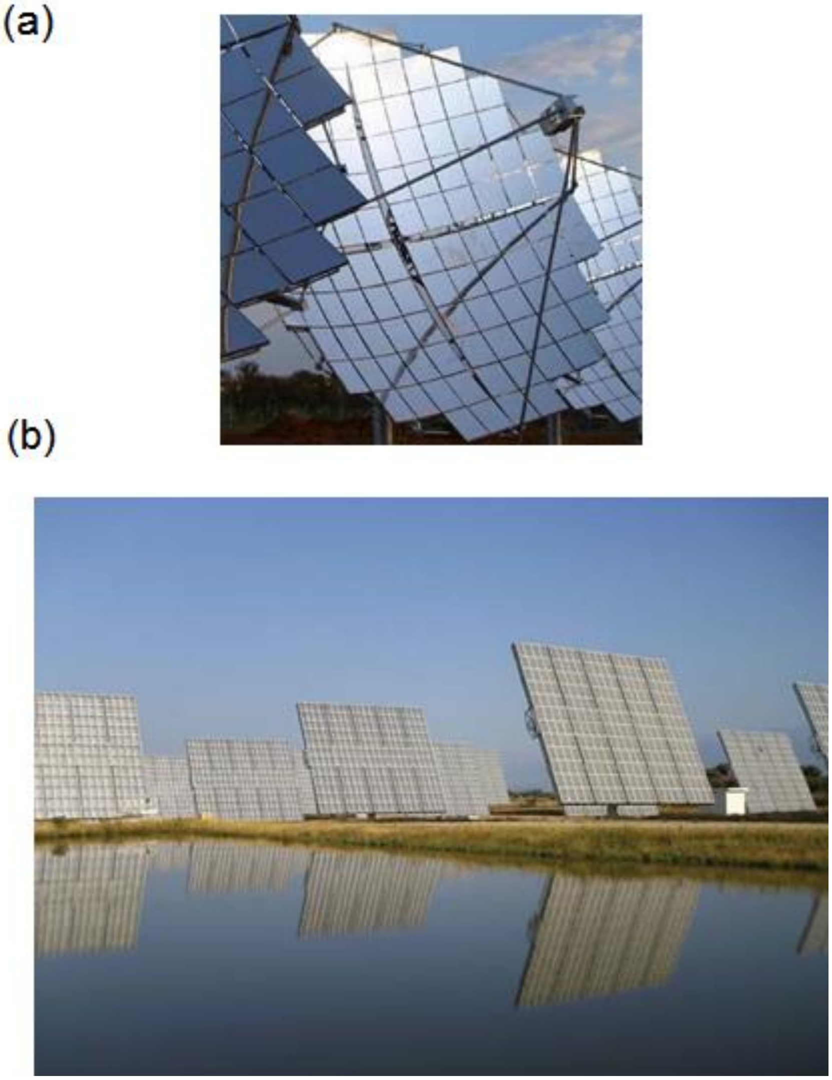

Figure 1.9 A concentrator photovoltaic system using a large reflective dish to focus the light onto an array of solar cells (a) and another type of concentrator system which utilizes Fresnel lens technology to focus the light onto an array of solar cells (b). Figures were adapted from reference [8, 46]

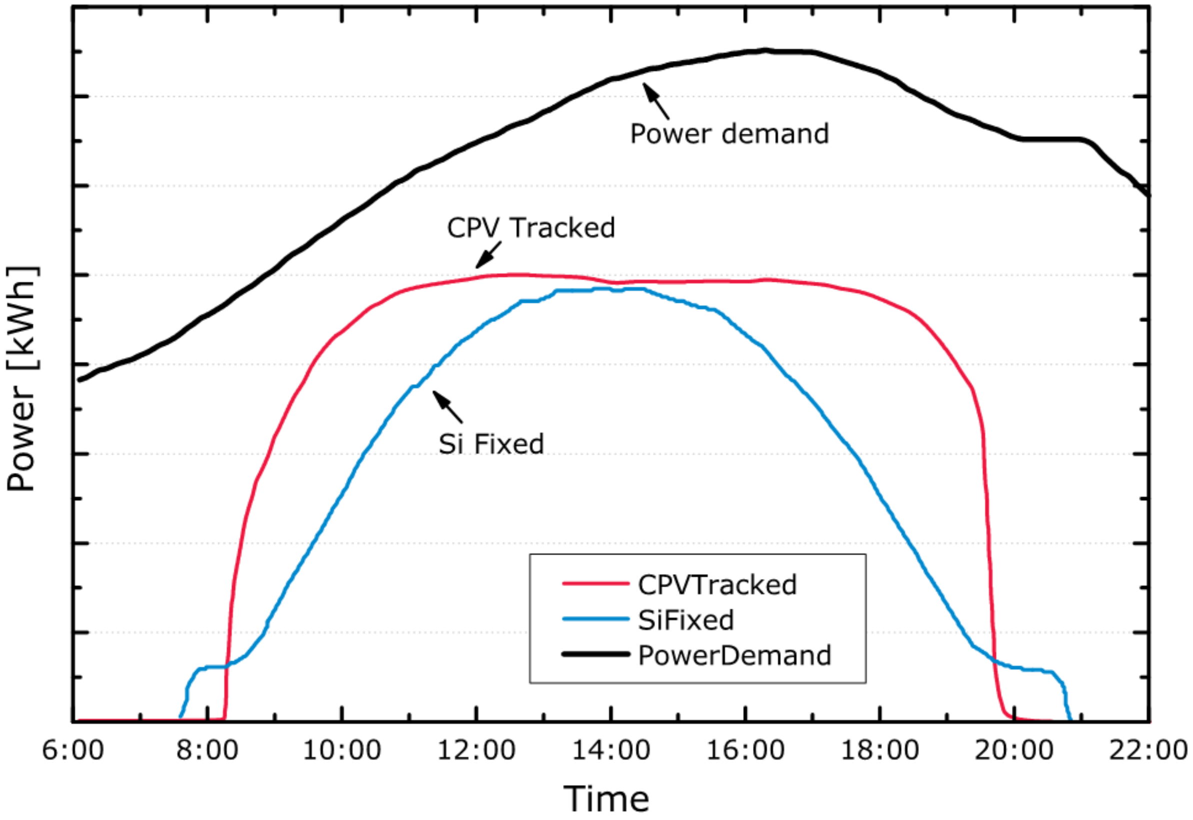

Figure 1.10 A comparison of the daily power generation tracked by a two-axis concentrator system compared to a fixed-angle silicon photovoltaic system. These data were acquired in Seville, Spain on 1 May 2008, and power the demand curve of California grid on 6 August 2008. Figure is adapted from reference [57].

1.11 References

1. *Energy Information Administration: Annual Energy Outlook*. 2014, US Department of Energy, Washington DC.

2. Perez, R. and M. Perez, *A Fundemental Look at Energy Reserves for the Planet.* SHC Solar Update, 2009. **50**(2).

3. Lewis, N.S. and D.G. Nocera, *Powering the planet: Chemical challenges in solar energy utilization.* Proceedings of the National Academy of Sciences, 2006. **103**(43): p. 15729-15735.

4. Almond, D.P. and P.M. Patel, *Photothermal Science and Techniques*. 1996: Kluwer Academic Publishers.

5. Alkire, R., D. Kolb, and J. Lipkowski, *Photoelectrochemical Materials and Energy Conversion Processes*. 2011: Wiley-VCH.

6. Honsberg, C. and S. Bowden. *http://pveducation.org/*. 2013 [cited 2014 2-10].

7. Altermatt, P. *pvlighthouse.com.au*. [cited 2014 2-10].

8. Luque, A. and S. Hegedus, eds. *Handbook of Photovoltaic Science and Engineering -- 2nd Ed.* 2011, John Wiley & Sons: West Sussex.

9. Nelson, J., *The Physics of Solar Cells (Properties of Semiconductor Materials)*. 2003, London: Imperial College Press.

10. Shockley, W. and H.J. Queisser, *DETAILED BALANCE LIMIT OF EFFICIENCY OF P-N JUNCTION SOLAR CELLS.* Journal of Applied Physics, 1961. **32**(3): p. 510-&.

11. Streetman, G. and S. Banerjee, *Solid State Electronic Devices -- 6th Ed.* 2000, Upper Saddle River, NJ: Prentice Hall.

12. Semonin, O.E., et al., *Peak External Photocurrent Quantum Efficiency Exceeding 100% via MEG in a Quantum Dot Solar Cell.* Science, 2011. **334**(6062): p. 1530-1533.

13. Hirst, L.C. and N.J. Ekins-Daukes, *Fundamental losses in solar cells.* Progress in Photovoltaics, 2011. **19**(3): p. 286-293.

14. Polman, A. and H.A. Atwater, *Photonic design principles for ultrahigh-efficiency photovoltaics.* Nature Materials, 2012. **11**(3): p. 174-177.

15. Zhao, J., et al., *24 PERCENT EFFICIENT SILICON SOLAR-CELLS WITH DOUBLE-LAYER ANTIREFLECTION COATINGS AND REDUCED RESISTANCE LOSS.* Applied Physics Letters, 1995. **66**(26): p. 3636-3638.

16. Kirchhoff, G., *Ueber das Verhältniss zwischen dem Emissionsvermögen und dem Absorptionsvermögen der Körper für Wärme und Licht.* Annalen der Physik, 1860. **185**(2): p. 275-301.

17. Mihalas, D. and B.W. Mihalas, *Foundations of Radiation Hydrodynamics*. Dover Books on Physics. 2013, Mineola, NY: Dover Publications.

18. Winston, R., J.C. Minano, and P. Benitez, *Non-Imaging Optics*. 2005, Burlington, MA: Elsevier Academic Press.

19. Yablonovitch, E., *STATISTICAL RAY OPTICS.* Journal of the Optical Society of America, 1982. **72**(7): p. 899-907.

20. Yablonovitch, E. *The Physics Behind the New Solar Cell Efficiency Record*. 2012 [cited 2014 2-10]; Available from: http://energyseminar.stanford.edu/node/369.

21. Green, M.A., et al., *Solar cell efficiency tables (version 43).* Progress in Photovoltaics, 2014. **22**(1): p. 1-9.

22. Green, M.A., *Third Generation Photovoltaics*. 2006, Heidelberg: Springer.

23. Miller, O.D., E. Yablonovitch, and S.R. Kurtz, *Strong Internal and External Luminescence as Solar Cells Approach the Shockley-Queisser Limit.* Ieee Journal of Photovoltaics, 2012. **2**(3): p. 303-311.

24. *PVPS Report A Snapshot of Global PV 1992-2012* 2012, IEA International Energy Agency.

25. Swanson, R.M., *A vision for crystalline silicon photovoltaics.* Progress in Photovoltaics: Research and Applications, 2006. **14**(5): p. 443-453.

26. Darling, S.B., et al., *Assumptions and the levelized cost of energy for photovoltaics.* Energy & Environmental Science, 2011. **4**(9): p. 3133-3139.

27. Moore, L.M. and H.N. Post, *Five years of operating experience at a large, utility-scale photovoltaic generating plant.* Progress in Photovoltaics, 2008. **16**(3): p. 249-259.

28. Feldman, D., et al., *Photovoltaic (PV) Pricing Trends: Historical, Recent, and Near-Term Projections* U.S.D.o. Energy, Editor. 2012: Washington D.C.

29. Feng, X., et al., *Competing fracture in kinetically controlled transfer printing.* Langmuir, 2007. **23**(25): p. 12555-12560.

30. Meitl, M.A., et al., *Transfer printing by kinetic control of adhesion to an elastomeric stamp.* Nature Materials, 2006. **5**(1): p. 33-38.

31. Meitl, M.A., et al., *Stress focusing for controlled fracture in microelectromechanical systems.* Applied Physics Letters, 2007. **90**(8).

32. Carlson, A., et al., *Transfer Printing Techniques for Materials Assembly and Micro/Nanodevice Fabrication.* Advanced Materials, 2012. **24**(39): p. 5284-5318.

33. Carlson, A., et al., *Active, Programmable Elastomeric Surfaces with Tunable Adhesion for Deterministic Assembly by Transfer Printing.* Advanced Functional Materials, 2012. **22**(21): p. 4476-4484.

34. Kim, S., et al., *Microstructured elastomeric surfaces with reversible adhesion and examples of their use in deterministic assembly by transfer printing.* Proceedings of the National Academy of Sciences of the United States of America, 2010. **107**(40): p. 17095-17100.

35. Sheng, X., et al., *Doubling the Power Output of Bifacial Thin-Film GaAs Solar Cells by Embedding Them in Luminescent Waveguides.* Advanced Energy Materials, 2013. **3**(8): p. 991-996.

36. Corcoran, C.J., et al., *Mechanisms of Enhanced Optical Absorption for Ultrathin Silicon Solar Microcells with an Integrated Nanostructured Backside Reflector.* Acs Applied Materials & Interfaces, 2013. **5**(10): p. 4239-4246.

37. Yoon, J., et al., *Flexible concentrator photovoltaics based on microscale silicon solar cells embedded in luminescent waveguides.* Nature Communications, 2011. **2**.

38. Baca, A.J., et al., *Compact monocrystalline silicon solar modules with high voltage outputs and mechanically flexible designs.* Energy & Environmental Science, 2010. **3**(2): p. 208-211.

39. Burroughs, S., et al., *A New Approach For A Low Cost CPV Module Design Utilizing Micro-Transfer Printing Technology.* AIP Conference Proceedings, 2010. **1277**(1): p. 163-166.

40. Ghosal, K., et al., *Performance of a micro-cell based transfer printed HCPV system in the South Eastern US.* AIP Conference Proceedings, 2012. **1477**(1): p. 327-330.

41. Furman, B., et al. *A high concentration photovoltaic module utilizing micro-transfer printing and surface mount technology*. in *Photovoltaic Specialists Conference (PVSC), 2010 35th IEEE*. 2010.

42. Algora, C. and V. Díaz, *Influence of series resistance on guidelines for manufacture of concentrator p-on-n GaAs solar cells.* Progress in Photovoltaics: Research and Applications, 2000. **8**(2): p. 211-225.

43. Sheldon, M.T., C.N. Eisler, and H.A. Atwater, *GaAs Passivation with Trioctylphosphine Sulfide for Enhanced Solar Cell Efficiency and Durability.* Advanced Energy Materials, 2012. **2**(3): p. 339-344.

44. Varshni, Y.P., *Temperature dependence of the energy gap in semiconductors.* Physica, 1967. **34**(1): p. 149-154.

45. Cotal, H., et al., *III-V multijunction solar cells for concentrating photovoltaics.* Energy & Environmental Science, 2009. **2**(2): p. 174-192.

46. King, R.R. *Raising the Efficiency Ceiling on Multijunction Solar Cells*. in *Stanford Photonics Research Center Symposium*. 2009. Stanford, CA.

47. Swanson, R.M., *The promise of concentrators.* Progress in Photovoltaics: Research and Applications, 2000. **8**(1): p. 93-111.

48. Kanjorski, R. *Semprius' 35.5 Percent Efficiency Sets New Record for Commercially Available Solar Modules*. 2013 [cited 2014 2-13]; Available from: http://www.prweb.com/releases/2013/9/prweb11163684.htm.

49. Saraidarov, T., et al., *Non-self-absorbing materials for Luminescent Solar Concentrators (LSC).* Chemical Physics Letters, 2010. **492**(1–3): p. 60-62.

50. Peters, M., et al., *The effect of photonic structures on the light guiding efficiency of fluorescent concentrators.* Journal of Applied Physics, 2009. **105**(1): p. -.

51. Smestad, G., et al., *The thermodynamic limits of light concentrators.* Solar Energy Materials, 1990. **21**(2–3): p. 99-111.

52. NREL. *Solar Radiation Data Manual for Flat-Plate and Concentrating Collectors*. 2013; Available from: http://rredc.nrel.gov/solar/pubs/redbook/HTML/.

53. AltaDevices, *Technology Bried: Single Solar Cell*. 2013: Sunnyvale, CA.

54. Green, M.A., *Radiative efficiency of state-of-the-art photovoltaic cells.* Progress in Photovoltaics: Research and Applications, 2012. **20**(4): p. 472-476.

55. Rockett, A.A., *Photovoltaics: The Engineering, Technology and Application of Solar Cells*. 2010.

56. *Newport Oriel: Spectral Irradiance Data* 2006: Irvine, CA. p. 7-26.

57. Gombert, A. *FLATCON Concentrator Photovoltaic Technology*. in *Concentrating Solar Technologies and Markets*. 2009.

Chapter 2

Light Trapping in Thin-Film Silicon Solar Microcells

This chapter focuses on fabrication and characterization of silicon microsolar cells incorporating a backside reflector to enhance cell performance as well as a surface light trapping structure that also increases cell performance. Portions of the text, as well as the figures, included herein are reproduced with permission from the following paper: C. J. Corcoran, S. Kang, L. Li, X. Guo, D. Chanda, R. G. Nuzzo, "Mechanisms of Enhanced Optical Absorption for Ultrathin Silicon Solar Microcells with an Integrated Nanostructured Backside Reflector", Applied Materials and Interfaces, 5 (10), pp 4239–4246 (2013). (dx.doi.org/10.1021/am400408g). Some of the figures in this text are modified and taken, with permission, from K.J. Yu, L. Gao, J.S.Park, Y.R. Lee, C. J. Corcoran, R. G. Nuzzo, D. Chanda, J.A. Rogers, "Light Trapping in Ultra-thin Monocrystalline Silicon Solar Cells", Advanced Energy Materials , 3, 1401-1406 (2013). (dx.doi.org: 10.1002/aenm.201370046).

2.1 Abstract

Herein this chapter explains the mechanisms of enhanced light absorption exhibited by ultra-thin Si solar microcells. There are two different methods in which light trapping inside microcells is accomplished: (1) the microcell is integrated above a periodically nanostructured, semi-transparent metallic reflector or (2) the microcell incorporates a light trapping structure on its surface.

The backside reflector comprises periodic nanoscale relief features formed by soft-imprint lithography with a thin (~ 35 nm) coating of Au. The work shows that microcells placed in direct contact above the nanostructured reflector's surface create Fabry-Pérot cavities, which

trap impinging light inside the Si slab via the excitation of cavity modes. Experimental measurements show that the short-circuit current and efficiency values for devices incorporating this thin, semi-transparent backside reflector outperform similar Si microcells integrated with a planer thick (~300 nm) opaque mirror by ~10-15% due to enhanced absorption. Computational modeling that is supported by experimental measurements reveal that the dominant methods of enhancement stem from a complex interplay between backside diffraction/scattering and Fabry-Pérot resonances. These same data demonstrate that plasmonic interactions contribute minimally, if at all, to the optical enhancements seen.

For the surface light trapping structure, 3 µm thick cells were generated from bulk wafers. Cells optimized for maximum absorption with a backside reflector produced energy conversion efficiencies that are greater than cells without the light trapping structure by ~190 %. When the top diffractive pattern is combined with a backside reflector, the reflector induces resonances associated with 0th order diffraction but 1st order diffraction. Additionally, these and other higher diffraction orders remain trapped due to total internal reflection.

2.2 Introduction

Photovoltaic (PV) technologies are playing an increasingly important role in designs for current and future energy infrastructures. As an absorber material, silicon (Si) retains a dominant position in the terrestrial PV market due to its high natural abundance [1], good optical [2] and electronic properties [3], along with its well-established production and processing methods [4]. Silicon-based devices are typically designed to be thick enough to enable full absorption of the solar photon flux up to the limits established by the material's band gap [5]. As a consequence, these optically-opaque devices can be expensive, bulky, and fragile. Engineering thin-film alternatives to conventional devices may reduce system costs as well as enable potentially more effective designs with new capabilities. An example of this comes from previous work performed at the University of Illinois with large-scale arrays of ultra-thin Si solar microcells fabricated from bulk wafers [6]. Other notable advances over the past years include a method for kerf-free production of thin sheets of Si that are ~25 μm in thickness from boules by controlled fracture [7-10]. The thin-film microcell devices demonstrated a high degree of mechanical flexibility, and therefore improved durability, that is unusual to Si. The drawback in reducing the thickness of the active material is that the absorption of photons can be reduced greatly, which reduces device performance. A thin-film cell, however, can perform as well as, or possibly better than, its thicker counterpart if light trapping methods are employed to extend the path length and/or the light intensity is enhanced inside the semiconductor slab.

In recent reports, we have described methods for improved light trapping in thin-Si solar cells, including: using nanostructured relief features on the surface of the device [11], wherein absorption is increased through diffraction and/or scattering; three-dimensional photovoltaic device geometries that enable the capture of more photons [12]; and passive concentration by employing luminescent waveguides [13], which offers the advantage of harvesting both direct and diffuse photons from the surrounding environment.

Several avenues have been investigated for enhancing the absorption of light in thin-film PV devices. Plasmonic optical designs is one active area of research that has attracted considerable attention, with the goal of increasing the absorption cross-section of the active layer by placing metallic sub-wavelength optical elements on the surface, inside, or on the backside of the solar cell [5, 14-19]. It has been demonstrated in this work that PV devices integrated with plasmonic components can yield increased photocurrents, with benefits evidenced in systems based on both inorganic and organic semiconductors. Another technique to increase light absorption via light-trapping involves harnessing whispering-gallery modes [20, 21] as well as textured surfaces [22, 23]. These and other techniques of trapping light inside PV devices have been reviewed in depth in the literature [14, 24]. Processes to integrate light-trapping/management structures in future generation PV technologies are of particular interest, with notable examples illustrating the varying facilities of optical integration at different stages of materials growth [25, 26],device fabrication [16, 27], and module integration [20].

Herein we investigate and characterize design principles for integrated sub-visible wavelength optics that can be used to improve the key operating parameters of PV devices. We specifically examine (1) an embossed "3D plasmonic crystal" from our earlier work [28, 29] for use as a backside reflector which, when integrated with a Si microcell, yields performance gains greater than those observed with a conventional mirror as well as (2) incorporating a light trapping structure on the surface of cells to enhance absorption. For the case of the backside reflector in (1), the complex interactions that occur between this periodically nanostructured reflector (PNR) and the Si microcell are examined in depth in this work.

Our findings compliment and extend those of earlier work on periodically nanostructured metallic or dielectric-based backside reflectors integrated with thin-film amorphous, monocrystalline, and microcrystalline Si solar cells [30-35]. We specifically show that in addition to mechanisms addressed in previous reports, significant enhancements are evidenced that stem from Fabry-Pérot-cavity-type resonances created at the microcell-PNR interface. These cavities are formed when a microcell with a flat backsurface is placed in proximate contact with the PNR. These Fabry-Pérot cavities trap light as standing waves at specific resonant frequencies which in turn serves to enhance the photocurrent [36]. The cavity architecture formed by the compliant contact of the microcell and PNR distinguishes this system from the conformal material coatings – mainly of amorphous Si – used in earlier studies of PV designs incorporating periodically nanostructured and randomly textured backsurfaces, [16, 24, 27, 32, 33] which are complicated due to potential increases in carrier collection from an enlarged active area [37]. The current work also speaks to perplexing issues of the relative importance of design rules, as raised in a recent study showing minimal differences in performance enhancements between a periodically nanostructured reflector from a randomly textured one (despite computational modeling predicting the periodic texture to be superior) [32]. The data and theoretical modeling results reported here highlight an important attribute of PNRs that strongly mediate their performance and further demonstrate that plasmonic enhancement mechanisms do not make a significant contribution to the enhancements seen. The enhanced cross-sections that result from Fabry-Pérot-based mechanisms supported by the PNRs reported here appear to be quite general and we believe might beneficially be extended to a random distribution of cavities of various depths, pitches, and diameters so long as they can couple the light transmitted through Si to cavity modes at wavelengths not absorbed from the first pass through the microcell. We have not carried out steps to optimize the intrinsic performance of the thin microcells used as reported in these studies, adopting instead cells derived from an SOI-based fabrication protocol [12] because of the exceptional smoothness of the backside surface that is required for successful device assembly by an adhesive-free transfer printing protocol [38-40].

For the case of (2), the surface light trapping structure, 3 µm thick microcells were generated from bulk wafers as opposed to SOI wafers. Fabricating cells from bulk wafers offers advantages such as reusing the wafer multiple times – even when considering mechanical polishing –to reduce costs. The method of generating cells from bulk wafers exploits the fact that the Si (111) face is not etched as quickly as the Si (110) face [6, 41, 42]. Incorporating surface/sidewall passivation onto the cells and using anisotropic etchants allows for the creation of these devices. Fabricated cells with the light-trapping structure that have been optimized for maximum absorption produced energy conversion efficiencies that are greater than cells without the light trapping structure by ~190 %. When the top diffractive pattern is combined with an external backside reflector, the reflector induces resonances associated with 0th order diffraction but 1st order diffraction, as revealed by computational modeling. Additionally, these and other higher diffraction orders remain trapped due to total internal reflection. What is most impressive about these results is that ~3 µm thick cells absorb nearly 80% of the AM 1.5D spectrum. This is impressive because Si has an indirect band gap at 1.1 eV, so traditional solar cells are hundreds of microns in thickness. Using such little material will reduce materials and overall module costs as well as allow for the opportunity of flexible form factors.

The PNR, case 1, a metal-coated plasmonic crystal, consists of a semi-transparent (thickness ~35 nm) layer of gold (Au) conformally coating nanowell relief features embossed by soft-imprint lithography [29]. The experimental measurements discussed below show that Si microcells on the PNR have short-circuit current density (J_{sc}) values that exceed the values from the same microcells when placed above flat, opaque mirrors (thickness ~300 nm) of the same metal by ~10-15%, a striking observation given the semi-transparent PNR can outperform a traditional thick opaque mirror. For case 2, the diffractive grating on the surface of the cells is formed by soft-imprint lithography. Finite-difference time domain (FDTD) simulations confirm that the main component of the enhanced absorption seen experimentally in both cases comes from 0th and higher diffraction order Fabry-Pérot resonances. To provide a more quantitative understanding of the mechanisms involved photocurrent measurements with microcells on the PNR are compared to measurements made with microcells above flat, opaque backside reflectors and flat reflectors with an identical semi-transparent thickness of metal. Wavelength dependent measurements demonstrate that the observed enhancements occur at the computationally-predicted wavelengths of light for cavity-mode-based mechanisms. Plasmonic influences were ruled out based upon studies using Al and Ag backside reflectors which suggest no contribution of surface plasmons to the enhancement in the photocurrent.

2.3 Materials and Methods

2.3.1 Fabrication of the Si Microcells from Silicon-on-Insulator Wafers

The fabrication strategy utilizes silicon-on-insulator (SOI; p-type device layer 2 μm ± 0.5 μm; 10-20 ohm-cm; 1 μm thick box; 300 μm thick handle; Ultrasil) wafers in a manner similar to previously published devices[12]. An image outlining the fabrication of the microcells is presented in Figure 2.1. The p-n junction is formed by selective area diffusion of boron (p++) and phosphorous (n++) from solid doping sources (Saint-Gobain Ceramics). Plasma-enhance chemical vapor deposition (PECVD)-grade oxide (~600 nm thick) is used as a doping mask for each diffusion step. Before each doping step the wafers are cleaned with the RCA-1/RCA-2 cleaning process at 70-80°C for ten minutes each. (RCA-1 = 1:1:5 $NH_4OH:H_2O_2:H_2O$ and RCA-2 = 1:1:5 $HCl:H_2O_2:H_2O$.) The conditions for doping are the following: 10 min exposure at 1000°C for phosphorous (n-type dopant) and 30 min exposure at 1000°C for boron (p-type dopant). A photoresist mask (AZ 5214, Clariant) on the surface is applied to define the side-walls, anchors, and trenches of the microcells. The photoresist was spin coated on the wafer at 3000 RPM to produce a uniform film that is ~1.4 μm thick. Inductively coupled plasma reactive-ion etching (STS-ICPRIE, STS Mesc Multiplex Advanced Silicon Etcher) is used to etch these features and generate straight side-walls and corners.

The conditions for ICP-RIE have been reported previously [42]. The parameters are as follows: O_2/SF_6 = 13/130 sccm (for the silicon etching step) and C_4F_8= 110 sccm (for passivation); gas pressure: 94 mTorr, etching power: 600/12 W inductively coupled plasma (ICP)/platen (P), deposition power: 600/0 W for ICP/P, etching duration: 7 s, and deposition duration: 5 s. Thicknesses of the device layer were measured with a profilometer after etching in the ICP-RIE instrument.

To allow for easier retrieval of the microcells, the anchors are anisotropically etched in KOH (Fisher) at 75°C for one minute. This anisotropic etching step creates sharp-angled corners in order to facilitate stress focusing for controlled fracture [43]. A PECVD-grade oxy-nitride mask (~100 nm) on the surface of the wafer serves as a passivation layer during KOH etching. The buried oxide layer is removed with 49% HF (Transene) and the microcells are suspended on the wafer by their anchors. (Note: HF is a highly corrosive and toxic. Users should wear goggles, a lab coat, and natural rubber, neoprene, or Viton® gloves when working with this chemical.) It is also important to cover the samples while submerged in concentrated HF to minimize porous silicon formation [44]. The sample is then placed briefly (~ 3 s) in KOH at 40°C to roughen the surface of the device as well as remove any porous silicon that may have generated during the HF etching step.

2.3.2 Fabrication of the Backside Reflectors

Fabrication of the PNR utilizes soft lithography and follows published procedures [28, 29, 45]. Briefly, large-area (5×5 mm^2) square arrays of sub-wavelength cylindrical depressions were molded onto the surface of a thin layer of a photo-curable epoxy (NOA 73, Norland), wherein a PDMS (10:1 Sylguard 184) mold containing the inverse pattern was pressed into the epoxy and cured under ultraviolet light. Blanket deposition of titania (~8 nm) for a thin adhesion layer and Au (~35 nm) by sputter coating at 5 mTorr completed the PNR. The features for all periodically arrayed reflectors reported herein have a relief depth of ~380 nm, a hole pitch of Λ~740 nm, and a hole diameter of ~440nm, as verified by atomic force microscopy (not shown) and SEM measurements. A thin layer of alumina is then deposited on each backside reflector by atomic layer deposition (ALD; Cabridge Nanotech; sample temperature 80°C; trimethylaluminum/H_2O; 10 sccm N_2, 0.03 s pulse; 0 s exposure/pump valve close length; 65 s pump/length of time between pulses), which acts as a thin insulating layer to prevent direct Si to Au contacts. The thickness of the alumina was verified with an ellipsometer on a reference piece of Si. A fabrication outline of the PNR is given in Figure 2.2.

Not having the insulator on the surface of each reflector was found to decrease J_{sc} values. Figure 2.3 compares J_{sc} values for different materials used as an insulating layer.) To clean the samples for this study, each Au-coated sample was placed under ultraviolet-produced ozone (UVO) for 10 minutes to remove any organics. Some samples were not cleaned (non-UVO cleaned surface) that had a native layer of organic material on the surface. 3-MPTMS was also used as a dielectric. From Figure 2.3, it is observed that alumina performs as the best insulating material.

The decrease in J_{sc} seen in the presence of configurations that involve direct Si-Au reflector contacts can be attributed to enhanced carrier recombination at the Si-metal interface. Si and Au have different work functions and when brought into contact their Fermi levels match at the interface, which results in metal-induced gap states. As these gap states occur deeper in the semiconductor than in the metal[46], an unwanted bottom contact is created that hinders device performance.

This thickness of Au was chosen since it is almost optically opaque in the visible/NIR, where our Si microcells are optically transparent. The periodicity and structure of the PNR were chosen based on experimental measurements with microcells above PNRs with varying hole diameters and pitches. The structure with a pitch of Λ~740 nm and a hole diameter of ~440nm was found to give the greatest enhancements in photocurrent Figure 2.4. Fabrication of Ag- and Al- PNRs and opaque mirrors followed similar ALD deposition and sputter-coating procedures.

2.3.3 Fabrication of Thin-Film Silicon Microcells from Bulk Wafers with a Light-Trapping Structure

Fabrication for microcells from bulk wafers uses a P-type Czochralski Si <111> wafer (1-10 Ω-cm, 450 μm thickness, Virginia Semiconductor) and starts with photolithographically patterning arrays of microbars that are 0.59 mm in length and 25 μm in width and are aligned perpendicular to the Si <110> direction. As with the previous cell fabrication discussed in an earlier section, inductively coupled plasma reactive ion etching (ICP-RIE) in the regions between the bars (strips with 80 μm widths) produces trenches with depths of about 3.3 μm. The cells were doped using solid-state doping of boron (Boron, BN-1250, Saint Gobain) along lengths of L_{p+} = 60 μm and phosphorus (Phosphorus, PH-1000N, Saint Gobain) along lengths of L_{n+} = 0.5 mm, at 1000 °C (25 min) and 950 °C (10 min), respectively, through patterned hard masks of SiO_2 (900 nm). Conformal deposition of SiO_2 (100 nm)/SiN_x (500 nm) by plasma-enhanced chemical vapor deposition followed by annealing at 400 °C for 30 min establishes etch barriers on the top surfaces of the cells, as well as the sidewalls and bottoms of the etched trenches.

Deposition of Cr (100 Å)/Au (1000 Å) by electron beam evaporation (Temescal, FC 1800) at angles of ± 30º coats the sidewalls and top surfaces, to allow for removal of the exposed SiO_2/SiN_x in the trenches by reactive-ion etching (CHF_3 (40 sccm)/O_2 (2 sccm); 50 mtorr, 150 W, 15 min). A solution of KOH (PSE-200, Transene) etches the silicon preferentially along the <110> direction. Beginning at the exposed bottoms of the trenches/edges, thereby producing arrays of freely suspended microbars tethered to the underlying wafer at their ends. Wet etchants remove the Cr/Au layers to expose the SiO_2/SiN_x films. Before each doping step the wafers are cleaned with the RCA-1/RCA-2 cleaning processes at 70-80°C for ten minutes each. (RCA-1 = 1:1:5 $NH_4OH:H_2O_2:H_2O$ and RCA-2 = 1:1:5 $HCl:H_2O_2:H_2O$.). Following metal stripping and the RCA cleaning processing, boron doping (1000 °C for 5 min) using the residual layers of SiO_2/SiNx as a mask yields a back surface field, thereby completing cell fabrication. Figure 2.5 shows a scanning electron microscope cross sectional image of a wafer after partial undercut etching of an array of µ-cells appears on the left, with a magnified view of an individual µ-cell on the right. The lower left figure depicts and image of the diffractive grating on the cell's surface and the figure to the right is a cartoon of an array of microcells and a schematic illustration. Each microcell is 25 µm wide, 0.59 mm long, and ~3 µm thick. The pink, grey, and blue areas in this illustration correspond to boron doped (L_{p+} = 60 µm), un-doped (L_{p-} = 30 µm), and phosphorus doped (L_{p+} = 0.5 mm) regions respectively. The cells are transfer printed on to glass slides coated in NOA (NOA 74, Norland Products Inc.). After transfer printing these cells onto a glass substrate, soft imprint lithography and etching generate the light trapping structure on the cell's surface. The light-trapping structure consists of a hexagonal lattice with a periodicity, diameter, and height of 500 nm, 370 nm, and 120 nm.

2.3.4 FDTD Models

For the FDTD studies, a Drude plus two-pole Lorentzian model for the complex frequency-dependent Au permittivity was employed, with parameters fit to empirical dielectric constant data[47]. The structure was excited with linearly polarized, plane-wave light as described in Ref. 43. Here we used FDTD to ‘fit’ our transmission data, shown in Figure 2.6, and then use that model, with those fitted parameters, to produce the absorption spectra.

Experimental transmission spectra was collected using a × 2.5, 0.07 numerical objective on an optical microscope (Hyperion 2000) coupled to a Fourier transform infrared spectrometer (Vertex 70) and outfitted with a spatial aperture having a diameter of 3.75mm. Transmission spectra were normalized to a glass slide with NOA 73 (Norland Products, Inc.). Variation in the silicon thickness accounts for differences between the experimental and computationally derived spectra.

For the modeled spectra for case (1), the Au thickness parameters are 35 nm on the surface (determined through ellipsometry); 12 nm and 20 nm on the sidewalls and bottoms of the relief features, respectively, as established by transmission electron microscopy measurements reported in a previous publication[28]. The PNR was modeled to have a relief depth of 380 nm, a hole pitch of $\Lambda = 740$ nm, and a hole diameter of 440nm. Each backside reflector was modeled to have 10 nm of alumina above its surface with the 10 nm layer extending along the side walls and bottom of the relief features.

For the modeled spectra in case (2), the light trapping structure on the surface of the cell case, the FDTD model assumes perfect arrays of nanoposts with hexagonal lattice with a periodicity, diameter, and height of 500 nm, 370 nm, and 120 nm, respectively.

2.3.5 Cell Measurements

All current density-voltage (J-V) measurements reported below were made under air mass 1.5D illumination calibrated to 1000 W/m^2 (Oriel, Model 91192) at room temperature with a source meter (Keithley, model 2400) using a Si reference cell for calibration of the simulator (Newport-Oriel, model 91150V). Measurements were performed on individual microcells transfer printed to glass slides, PNRs, and flat mirrors. It was observed that transfer printing the cells to these devices had no degradation on cell performance. This was verified by transferring a cell to a glass substrate, recording the J-V curve, and then transferring it to a backside reflector and back to the respective glass substrate to re-measure the J-V. The J-V curve upon re-measurement on the glass substrate was identical to the earlier J-V curve.

2.3.6 Solar Cell Measurements with Apertures

To accurately characterize the cells in case study (1), and in order to minimize multiple reflections of light around the perimeter of the solar cells [48], an anodized Al cover having an aperture area of 2 x 2 mm^2 was placed over each substrate with another anodized Al backplate placed below the substrate supporting the microcell (Figure 2.7). All measurements reported are based on the area of the microcell. Sample variance in the J-V results was quite large for microcells from different wafer batches. Conversion efficiencies for microcells between different wafers, as measured on a glass slide with the anodized Al backplate, ranged from 1.2% to 1.6%, open-circuit voltage (V_{oc}) values ranged from 390 mV to 450 mV, fill factors varied from 55% to 65%, and J_{sc} values ranged from 4.6 mA/cm^2 to 6.0 mA/cm^2. To overcome sample variance, each microcell was first measured on a glass slide and then transfer-printed to the desired reflector where the measurement was then repeated. This allowed each J-V measurement incorporating a reflector to be normalized to the one made on the glass slide.

The 2 x 2 mm^2 aperture is quite large relative to the area of the microcell (~2.5 x 10^4 μm^2). Experiments were performed wherein microcells on glass were measured with small-area apertures. These small-area apertures had an aperture area of 70 x 520 μm^2 and these J-V results were compared to the 2 x 2 mm^2 aperture results to verify that internal reflections of light were in fact small contributors to the cell's response. We observed a ~5-10% overall decrease in the J_{sc} with the small-area aperture vs. the 2 x 2 mm^2 (large-area) aperture. Excessive light scattering from the backside reflectors is considered to be extremely minor given the height of the microcells as well as band-pass filter measurements on microcells inside the small-area apertures when compared to the large-area aperture results (Figure 2.8). Because the small-area apertures use Au, they correctly match any excessive light scattering seen from backside reflector measurements.

To perform these measurements, microcells were transfer printed to a glass slide coated with SU-8 (SU-8 2002, Microchem) and covered with the anodized Al back cover and 2 x 2 mm2 aperture and had J-V/filter measurements performed. Next Cr/Au (~4 nm / 150 nm) was sputtered on the surface of glass slides with samples covered in AZ 5214. Afterward another PR mask was added to serve as an etch-back mask. An etch-back step was then performed to expose the microcells and the PR mask was removed by emersion in acetone.

The decrease in the J_{sc} in the NIR can be attributed to small amounts of light scattering off of the anodized Al backplate when the microcell is first measured on the glass slide with the large-area aperture vs. the small-area aperture.

Additionally, compared to the large-area aperture measurements, relatively modest enhancements in the photocurrent (~5-10%) were observed in the visible part of the spectrum with the J_{sc} falling off in the NIR. The decrease in the J_{sc} in the NIR can be attributed to small amounts of light scattering off of the anodized Al backplate when the microcell is first measured on the glass slide with the large-area aperture vs. the small-area aperture. Any enhancements in photocurrent reported therefore come mainly from light that passes through the front of the device. Because ~1.7 µm thick Si absorbs all of the photons with wavelengths of ~500 nm or greater in energy [2], absorption enhancements with backside reflectors reported here can come only from longer wavelength photons that were not absorbed after the initial pass through the device. This is discussed in greater detail in the sections that follow.

For the cells with the light-trapping structure on the surface, apertures with a window of 10µm around the perimeter of the solar cell were used during each measurement. An anodized Al backplate was also used for each measurement to minimize internal reflections of light. The apertures consisted of Cr/Au and wet etchants were used to pattern the outside perimeter of the cell to form the apertures.

2.4 Results and Discussion

2.4.1 Microcells on the Backside Reflector

The results and discussion section will first start with the results presented for case 1, microcells above a backside reflector, and then move onto case 2, microcells with a surface light-trapping structure. Figure 2.9a presents a schematic illustration of an individual microcell above the nanostructured surface. The microcells measure 500 µm in length, 50 µm in width, and ~1.7 µm in thicknesses and were fabricated from SOI wafers. Figure 2.9b shows a sparse array of microcells transfer printed to the surface of the PNR with their doping areas outlined in purple (p++) and green (n++). This doping profile places the p-n junction on the top of the microcell. The spacing between the p++ and n++ regions on the surface is 50 μm. This spacing provides a high internal electrical field to efficiently separate photo-generated electron-hole pairs.

To achieve direct contact onto the surface of each backside reflector, the microcells are transfer printed without an adhesive layer. Adhesive-free transfer printing relies on the kinetic control of adhesion between a microcell and a polydimethylsiloxane (PDMS) stamp, where a slow peeling velocity favors adhesion between the microcell and backside reflector and a faster one favors adhesion between the microcell and PDMS stamp. The mechanics involved with transfer printing have been explored in other papers [38-40] and mentioned in the introductory chapter of this thesis. Working with SOI improves transfer printing results since the back surfaces of the microcells are extremely smooth, much more so than results from fabrication schemes used to fabricate microcells using bulk Si wafers. The etching processes used in these cases [6, 42] generates a back surface too rough for standard forms of adhesive-free transfer printing. A scanning electron microscope (SEM) image of a microcell transfer printed to an Au-coated PNR is presented in Figure 2.9c; the inset shows a zoomed-in profile for the Si-PNR interface which demonstrates the direct contact at the backsurface between the reflector and microcell to form the Fabry-Pérot-cavities.

Figure 2.10a depicts the simulated optical absorption for 1.7 μm thick bare Si without any reflector (black), above a 300 nm thick Au mirror (blue), and above the PNR (red). For Si without any backside reflector, the absorption is poor; it absorbs less than 60% of the light at 600 nm and light absorption quickly diminishes further into the NIR region of the spectrum. The peaks seen in all the plots given in the figure can be attributed to Fabry-Pérot resonances. To understand the detailed nature of these resonances we performed 3D FDTD simulations. Figure 2.10b presents FDTD-computed, cross-sectional electric field distributions ($|E(x,z)|^2$) at various wavelengths for both reflectors. The illustrations to the far left of Figure 2.10b are a depiction of each modeled system. As is evident from the data given in Figure 2.10b, at λ~675 nm (point 1 on Figure 2.10a) the absorption for both backside reflectors (opaque and PNR) is characteristic of 0th order Fabry-Pérot resonances, which occur at the same positions as on spectra of Si without a backside reflector (Figure 2.10a). The absorption peak at λ ~675 nm for the Au mirror is marginally stronger than the absorption peak corresponding to the PNR due to total back reflection from the opaque mirror. The same trend persists where Si on the opaque Au mirror absorbs more light than the Si on the Au PNR up to 800 nm. After 800 nm the absorption peaks for Si on the mirror quickly diminish and the PNR case begins to outperform all the way through the NIR part of the spectrum. In the NIR domain, there appear to be intense, broadened peaks in the absorption plot for the Si above the PNR due to the presence of strong steep angle 1st order Fabry-Pérot resonances (other higher (> 1) diffraction orders are negligible due to the combination of the period and the excitation wavelengths) as evident in the cross-sectional images of Figure 10b for λ = 1001 nm and λ = 1075 nm; these two wavelengths clearly show 1st order standing wave interference patterns. This effect is pronounced for the longer wavelength range as the first order angle varies as $\theta_1 = \sin^{-1}[\lambda / n(\lambda)\Lambda]$, and consequently the path length increases with λ; we also identified these Fabry-Pérot resonances as 0th order and 1st order cavity modes through an effective medium calculation. Additional wavelength dependent cross-sectional images are provided in Figure 2.11.

Figure 2.12a depicts the enhancement in J_{sc} for each reflector as a function of insulating layer thickness. The amount of alumina was varied to find the thickness that optimized electrical insulation between Au and the microcell, which was determined to be between 5-10 nm. At 10 nm of alumina on each reflector, Figure 2.12a shows a ~15% enhancement in the photocurrent when the microcell is on the surface of the flat, opaque reflector while there is a ~26% enhancement in the photocurrent when the microcell is on the PNR. We also performed measurements with a 35 nm thick, flat Au BSR and found the enhancement in the J_{sc} to be ~10% relative to the anodized Al back plate. The measured J_{sc} remains constant as the amount of alumina on the Au mirror is increased. A different result is observed for thicker layers of alumina on the PNR. The PNR has an observed drop in enhancement going beyond 10 nm of alumina. From the FDTD computations, we found that the electric field enhancements extend ten nanometers at the edges of the Au nanowells (due to localized surface plasmons) to hundreds of nanometers and all way through the Si slab (corresponding to 0^{th} and higher diffraction order Fabry-Pérot resonances). Figure 2.12b shows representative J-V measurements for microcells prepared on glass (black), above the Au mirror (blue), and above the Au PNR (red) and Table 2.1 gives their key parameters. The microcell on glass has an initial efficiency of 1.40% with FF = 61%, V_{oc} = 410 mV, and J_{sc} = 5.61 mA/cm^2. Once transferred to the PNR, Eff = 1.75%, FF = 60%, V_{oc} = 419 mV, and J_{sc} = 7.02 mA/cm^2. A similar performing microcell was transferred to an Au mirror and had the following characteristics: Eff = 1.59%, FF = 60%, V_{oc} = 417 mV, and J_{sc} = 6.42 mA/cm^2. The slight enhancement in the V_{oc} (relative to the microcell on the glass slide) is to be expected since V_{oc} increases logarithmically with illumination intensity[49]. For the present case we measured almost the same FFs for representative cells above the Au PNR and the Au mirror, indicating negligible changes in the series resistance. We also found that slightly higher efficiencies occur in the PNR case due to the enhanced absorption induced by Fabry-Perot resonances. Because of the large surface-area-to-volume ratio of these microcells, as well as the fact that these devices have no passivation layer (a choice made to simplify the fabrication of thin microcells with the extremely flat back surfaces, as required for adhesive free transfer printing, from the SOI source wafer), carrier recombination at the surface is quite high (as shown by the low V_{oc} values).

We should note that these SOI-derived microcells, although functional, are of relatively low performance as compared to both commercial Si solar cells and microcells we have previously reported [6, 11, 13]. Their use serves solely to facilitate a proof-of-concept on the qualities realized by the precise placement of a PNR in proximate planar contact with the cell. The lower performance of these devices is a well-understood result of the fabrication process [12], which is not optimized. The performance is affected by the lack of a surface passivation layer encapsulating the microcells as well as the microcells not possessing a back-surface field [50, 51]. Additional factors that impact our cell performance include the lack of an anti-reflective coating [50, 51], a highly doped emitter, and having top and bottom surfaces that are nearly atomically flat, which reduces the potential for multiple internal reflections of light. Work has been done into developing improved fabrication methods and integration schemes for ultra-thin cells that mitigate many of these impacts [52].

Photocurrent measurements based on a given wavelength range, up to the material's band gap, as measured by filters placed in front of the solar simulator, are given in Figure 2.12c. The graph is plotted in terms of enhancement factor where measurements for microcells on the PNR are normalized to measurements for microcells on the flat, opaque Au backside reflector (red) with accompanying FDTD results for the Si slab above the PNR normalized to the Si slab above the flat, opaque Au (blue). The horizontal error bars depict the wavelength range measured while the vertical error bars represent measured sample variance. To study the wavelength dependent absorption enhancement, band pass filters were used to measure absorption for specific wavelength ranges. The band-pass filters had the following center wavelengths: 550 nm (FWHM± 37.5 nm), 650 nm (FWHM ± 37.5 nm), and 750 nm (FWHM ± 37.5 nm). A combination of short-pass and long-pass filters had the following center wavelengths 825 nm (FWHM ± 25 nm), 900 nm (FWHM ± 50 nm), 925 nm (FWHM ± 25 nm), 950 nm (FWHM ± 50 nm), 975 nm (FWHM ± 25 nm), and 1050 nm (FWHM ± 50 nm). Similar to the FDTD results, the Au mirror marginally outperforms the PNR up until about 800 nm. After 800 nm the PNR outperforms the opaque backside reflector. The regions for absorption enhancement from the experimental data in Figure 2.12c agree quite well with the FDTD models given in Figure 2.10a. Photocurrent enhancements after 900 nm are the most drastic with the PNR having an enhancement factor ~8 in the NIR.

A few of the cross-sectional images in Figure 2.10b show surface plasmons on the sides of the upper and lower portions of the Au nanowells. In order to rule out any contribution to the enhancement in the photocurrent from surface plasmons, filter measurements were also performed on microcells above Al- and Ag-based PNRs and their respective flat mirrors (Figure 2.13). Ag and Al were studied since Au generates plasmons in the visible, Ag generates plasmons in the visible/NIR, and Al generates plasmons in the ultra-violet [53-55]. The benefit of studying the Al-based system is that no plasmons will be generated since Si absorbs and reflects all the ultra-violet light (where Al is active). The enhancement in the J_{sc} for each PNR and mirror were similar to their Au counterparts ~26% and ~15%, respectively, when compared to the anodized Al backplate. From the filter measurements, a similar trend was observed with the opaque mirror out-performing each metallic PNR in the shorter wavelength range. After 800 nm the PNR outperforms the mirror of the same metal as shown in Figure 2.13. Furthermore, the trends in J_{sc} for each reflector were similar to the reported reflection measurements of each backside reflector (Figure 2.14). These measurements therefore rule out dominating contributions from surface plasmons to the enhancements seen in the photocurrent. For the present PNR design we haven't observed any important contributions from plasmonic effects over the silicon absorption bandwidth.

2.4.2 Surface Light-Trapping Structures

For the second case of Si solar cells with a surface light-trapping structure, Figures 2.15a and 2.15b compare the relative absorption of each type of solar cell with respect to the AM1.5D spectrum. FDTD and experimental optical microscope measurements were performed for 3 μm thick cells with and without the light trapping scheme (bare vs LT as shown in the figures). Experimental absorption measurements are limited to wavelengths between 550 nm and 1100 by the source-detector in the microscope-coupled FTIR system (Bruker Vertex 70-Huperion 1000). The detector begins to have poor response for wavelengths of light smaller than 550 nm. The simulated and experimentally measured absorption values, when integrated over the AM 1.5D spectrum, are 27.6% (Figure 2.15a) and 28% (Figure 2.15b), respectively, for the microcell with no light-trapping structure. For the light-trapping microcell, these values increase to 69% (modeled) and 77% (experimental). Figure 2.15c overlays Figures 2.15a and 2.15b and shows that the absorption peaks match, but the peaks are much greater for the experimental case. This discrepancy will be discussed later in this section. Regardless, there is agreement in the experimental and modeled data. As is expected with silicon, the thin-film silicon with no light trapping structure barely absorbs any light at its band edge. The ultra-thin thickness of these cells lends them to Fabry-Perot cavity resonances, as in the case of the cells with the nanostructured backside reflector. The light trapping structure on the surface of the cell, however, acts as a diffractive grating and greatly enhances absorption. In this case, the top diffractive pattern associated of the light-trapping structure in combination with a flat backside reflector underneath the microcells induces resonances associated with 0^{th} and higher-order modes. These diffraction orders remain trapped due to total internal reflection of light. The FDTD simulation for these studies assumes perfect arrays of nanoposts as the diffractive top surfaces of the microcells and a perfectly flat back-surface. For the model, these structures diffract the incident light as multiple diffraction orders inside the silicon. In fabricated cells, the nano-posts and back-surface are non-ideal surfaces and have slight surface imperfections (Figures 2.15d and 2.15e) that are due to (1) imperfections associated with the lithography and dry etching processes when fabricating the surface light-trapping structure and (2) the wet etching processes leaving the backsurface slightly roughened. These imperfections on the front and back surfaces scatter the light in excess of that expected by diffraction alone (in the FDTD), which leads to additional absorption and further total internal reflection of light inside of the solar microcell. These discrepancies between experimental results and FDTD model are from these surface non-idealities.

Figure 2.16a shows the measured J-V for various microcell designs under AM 1.5D illumination of 1000 W/m^2 at room temperature. Efficiency measurements are taken using the overall area of each cell. From the figure, separate studies isolate the effects of the light-trapping structure (LTS), anti-reflective coatings (ARC), as well as flat backside reflectors (BSR), and their combinations. The samples measured were bare Si, with ARC, with BSR, with BSR +ARC, with LTS, with LTS +ARC, with LTS +BSR and, lastly, with LTS +BSR +ARC. The data in this figure has a ton of information. Because all the cells are fabricated in an identical manner, there doping profiles and other properties should be nearly similar. As a consequence of this certain information can be obtained. Trends in short-circuit current should follow those in the optical generation rate (see Equation 1.2), or, to put another way, how much light the cell "sees". As shown in the table of Figure 2.16b, the short-circuit current of the bare cell and the bare Si with LTS +BSR +ARC are 9.62 mA/cm^2 and 24.57 mA/cm^2 , respectively. The enhancement in the current of the bare cell compared to that of the LT cell (LTS +BSR +ARC) is ~155%, which is consistent with both FDTD-predicted and experimentally-measured enhancements in absorption.

Since the open-circuit voltage is logarithmically proportional to absorption, modest enhancements in the voltage should be expected. The open-circuit voltage for the microcells with bare Si and with LTS +BSR +ARC are 0.45 V and 0.494 V. This corresponds to ~10% increase in V_{oc}, roughly consistent with the expected weak, logarithmic scaling. The fill factors remain quite consistent – between 70.5% and 71.5% – with not much variation. Because these samples were scanned with two probe tips as opposed to a four probe setup, series resistances in the wiring and other factors can skew these results. Albeit, to only modest values. The error in measuring fill factor from using two probe tips is probably ~1% of the fill factor, so the experimentally measured fill factors for each of the cells are then nearly identical. The experimentally derived energy conversion efficiencies are 2.90, 3.7, 4.14, 4.69, 6.13, 6.68, 7.67 and 8.47% for various cases, as tabulated in Figure 2.16b. The cell with the LTS +BSR +ARC (Figure 2.16c) configuration has the greatest energy conversion efficiency, which is consistent with enhancements in J_{sc} (~155%) and V_{oc} (~9.78%). The result is that the efficiency of this microcell is ~190% greater than that of the bare Si cell. Furthermore, what is very impressive is the fact that these unpassivated cells that are three microns in thickness, have an energy conversion efficiency of ~8.5%. This energy conversion efficiency is rather low, given that the cell absorbs nearly 80% of the AM 1.5D solar spectrum. The reason for this lower cell performance is due to inadequate surface passivation, or, to use the bucket-feeding water wheel analogy, there are some leaks in this bucket. Early studies of unpassivated silicon solar cells had energy conversion efficiencies of around 10% [51, 56, 57]. These cells were also hundreds of microns in thickness. Therefore, from this surface light-trapping structure in combination with adequate surface and side-wall passivation, it could be possible to produce Si microcells with energy conversion efficiencies close to 20 percent or greater with the cell's thickness being only ~ 3 μm.

2.4.3 Applications to Commercial Photovoltaic Devices

Solar cells utilizing back contacts, such as point-contact solar cells [58-60], can benefit from the design principles and light management schemes established by this work. The key aspect to enable increased performance occurs when the device is in direct contact with the backside reflector. This allows the device to take advantage of the intense, near-field phenomena that enable a higher absorption cross-section, and therefore, better performance. Outlined in Figure 2.17a is the current cell setup with the PNR and in Figure 2.17b is a modified point-contact solar cell setup that can take advantage of the intense Fabry-Perot resonances from a backside reflector. This could reduce the thickness of silicon required to make a device. Further reductions in absorber material also come from having a surface light-trapping structure above the silicon cell as well. Diffraction gratings on different sides of the cell can be tuned to diffract different parts of the solar spectrum. If it is possible to get 80% of the light absorbed inside a 3 μm thick silicon device, it is feasible to enhance that number to 90% or 95% with a thicker cell and multiple gratings on both sides. Passivation and p-n junction formation with amorphous silicon, as is the case with Sanyo HIT solar cells [61-63], could produce very efficient, thin-film devices that are cheaper to manufacture than current silicon technology.

2.5 Conclusions

To summarize, we report on a semi-transparent backside reflector with nanoscale relief features that can outperform an optically opaque, flat reflector of the same metal due to excitation of higher order Fabry-Pérot resonances as well as light diffraction/scattering. It has also been shown the microcells that are ~3 μm thick can absorb nearly 80% of the solar spectrum once a light trapping structure is added to the surface. The mechanisms that enable enhanced absorption for microcells above the PNR and with the light-trapping structure have been identified and computational modeling reveals that the major component for the increased absorption in both cases stems from higher order Fabry-Pérot resonances. For the PNR case, J-V measurements incorporating filters below the solar simulator show higher photocurrent densities in the red/NIR domain of the spectrum, which agree with our computational model. These experimental results on working devices further support the notion that Fabry-Pérot resonances are the dominant mechanism for the enhanced photocurrent. Filter measurements with Al- and Ag-based PNRs and mirrors show similar trends in the J_{sc} to Au PNRs and mirrors and therefore rule out any possible contribution from surface plasmons to the enhanced absorption.

2.6 Acknowledgements

This work was financially supported by the Department of Energy through Energy Frontier Research Center under award number DE-SC0001293 (subcontract no. 67N-1087758). C.J. Corcoran thanks K.J. Yu, A.-P. Le, H.-J. Chung, M.R. Hansen, G.A. Mensing, and A. A. Rockett for useful discussions; M.W. Cason and E. Brueckner for assistance with SEM images

and solar cell illustrations; J.A. Rogers for computational resources to perform the FDTD simulations; P.V. Braun for use of his optical microscope; and the faculty and staff at the Materials Research Center, Micro and Nanotechnology Laboratory, and the Micro-Nano-Mechanical Systems Cleanroom.

2.7 Figures and Tables

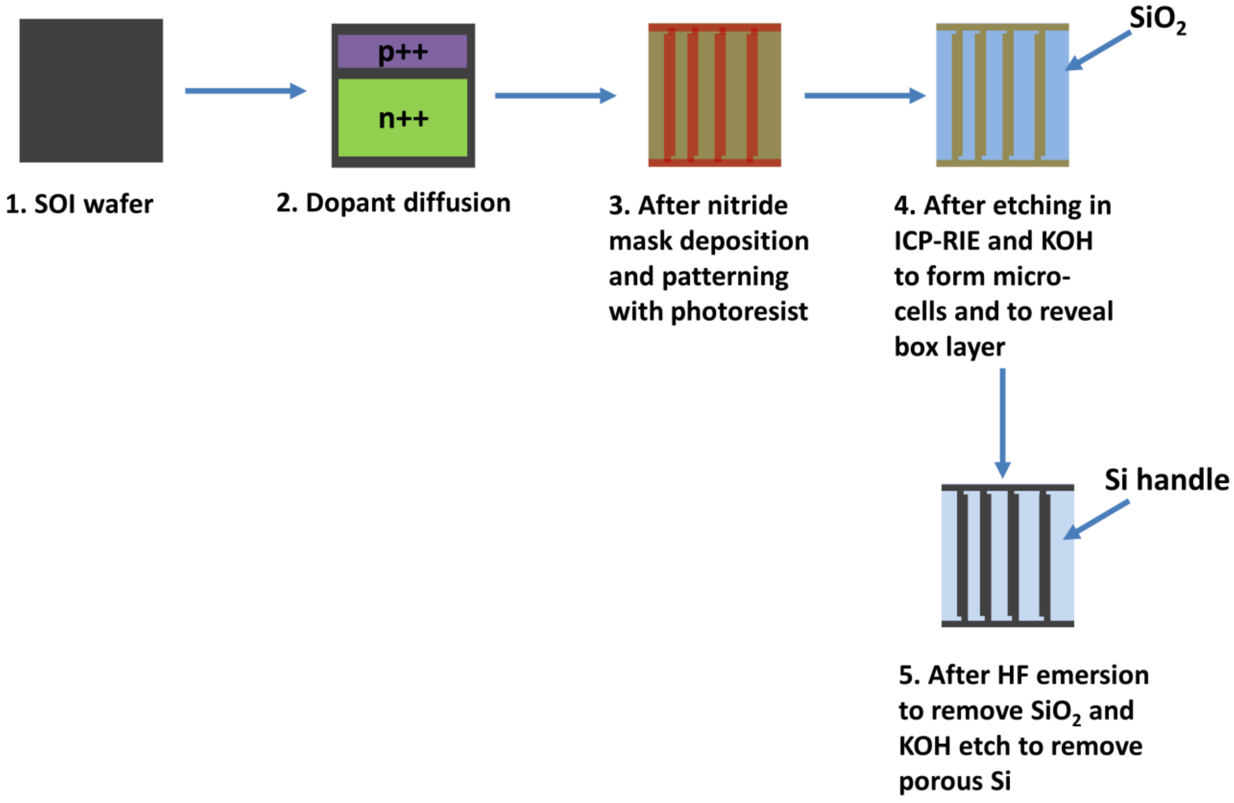

Figure 2.1 Outline of the microcell fabrication process. Further details are given in the experimental section of the paper. The Si handle in part 5 is shown in blue to differentiate it from the Si microcells.

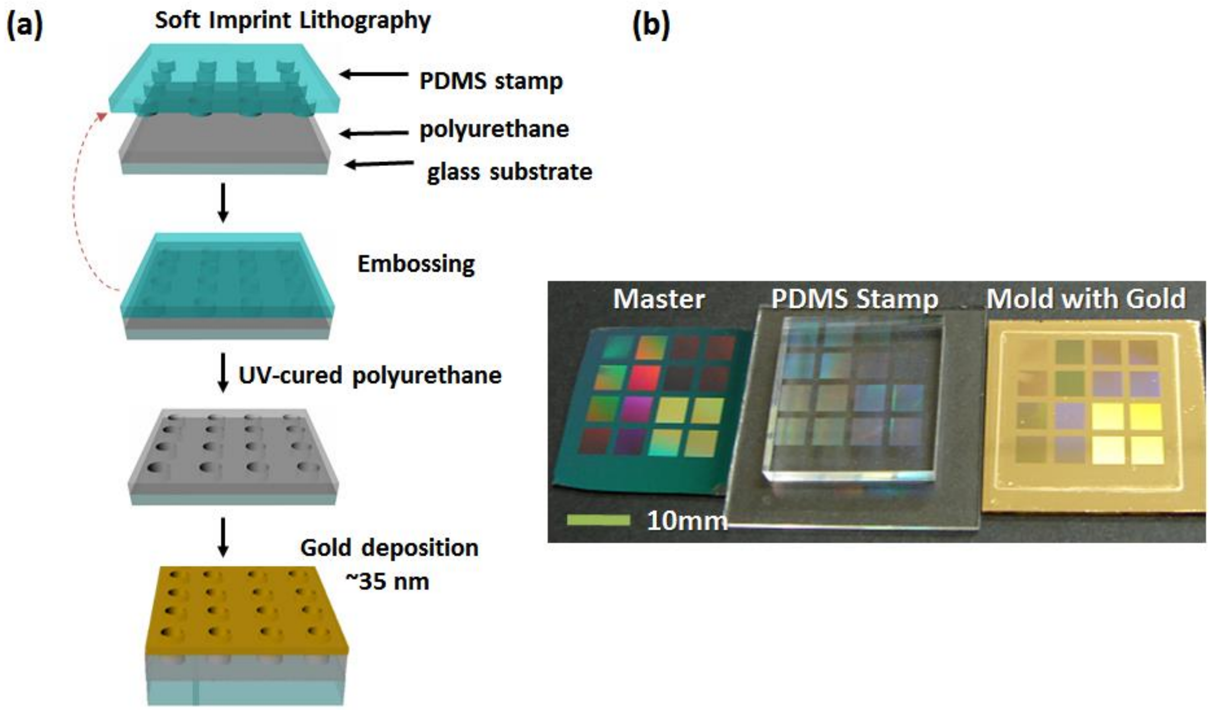

Figure 2.2 Schematic of the soft-imprint lithography process. (a) Creating a hard PDMS stamp from a mold and embossing it to polyurethane. After this step the sample is cured and the stamp is removed. The backside reflector is then coated with Au from sputter-coating. (b) Images of the photoresist master, the PDMS stamp (the inverse of the image), and the final PNR.

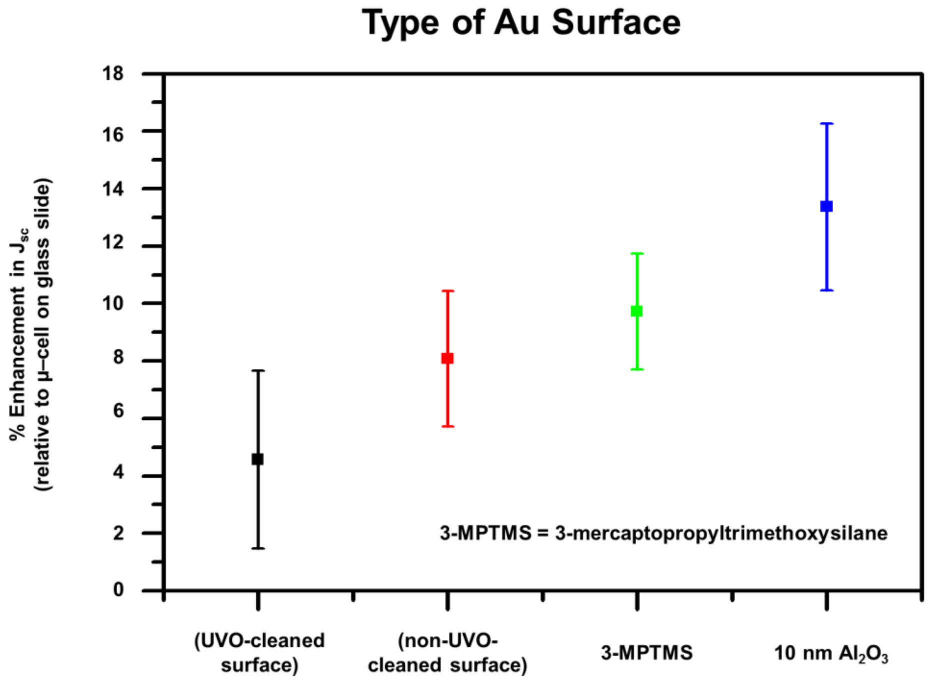

Figure 2.3 Comparison of dielectric insulating layer on J_{sc} for flat, opaque gold backside reflectors.

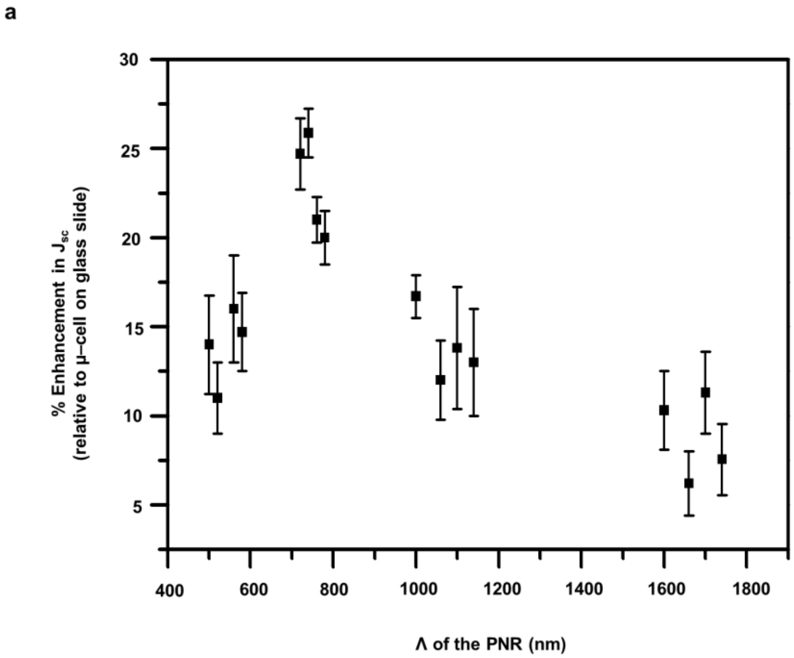

b

D = 240 Λ = 500	D = 280 Λ = 560	D = 420 Λ = 720	D = 460 Λ = 760
D = 260 Λ = 520	D = 300 Λ = 580	D = 440 Λ = 740	D = 480 Λ = 780
D = 600 Λ = 1000	D = 660 Λ = 1100	D = 960 Λ = 1600	D = 1020 Λ = 1700
D = 640 Λ = 1060	D = 700 Λ = 1140	D = 1000 Λ = 1660	D = 1060 Λ = 1740

Figure 2.4 Enhancement in J_{sc} based on PNR pitch (a) and the various PNR pitches and diameters studied (b).

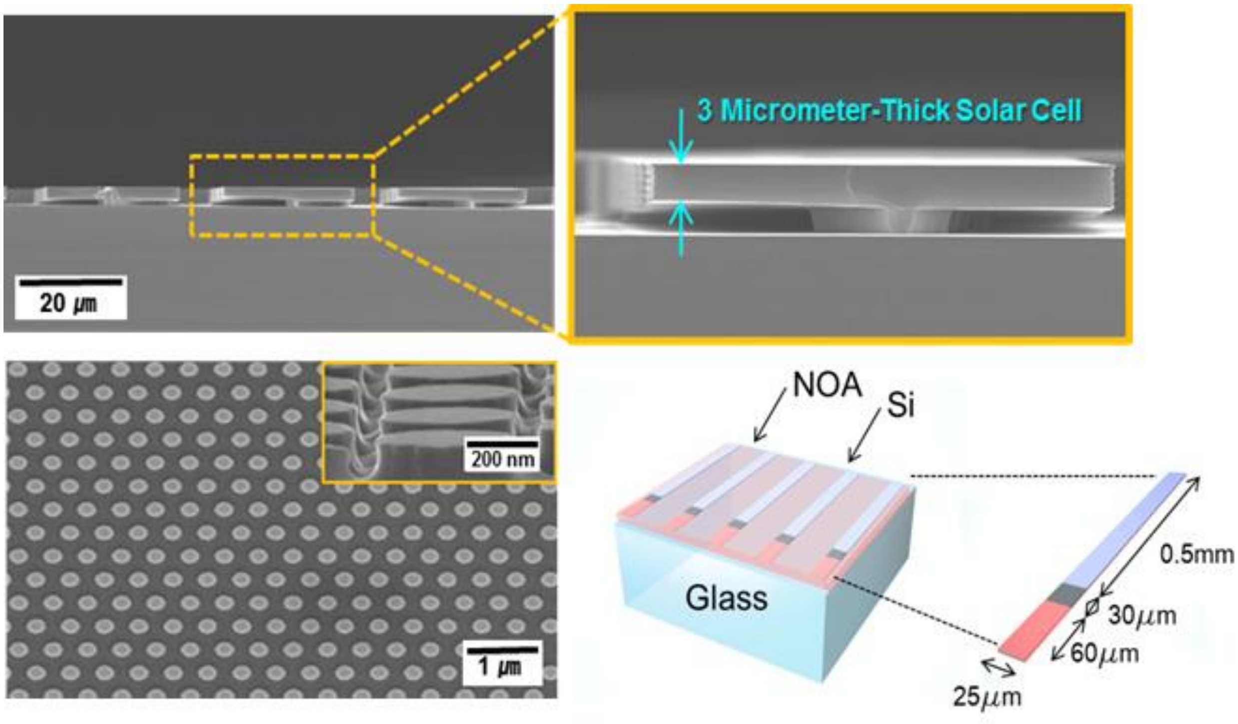

Figure 2.5 SEM images from microcells on bulk wafers. Top left figure shows a small an array of microcells on the wafer partially undercut with a zoomed-in image of a microcell. The lower left figure shows the light trapping structure on the surface that is formed by soft-imprint lithography. The lower right-hand figure is an illustration of a microcell area outlining the cell size and doping regions.

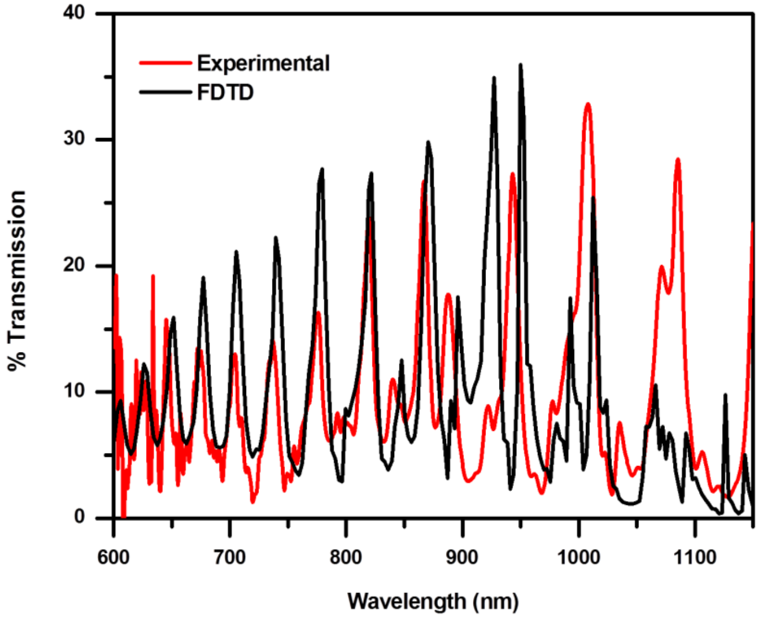

Figure 2.6 Experimental and FDTD of Si on an Au PNR. 0-th order transmission spectra of 1.7 µm thick piece of Si on PNR comparison of experimental (red) and computer-modeled FDTD (black).

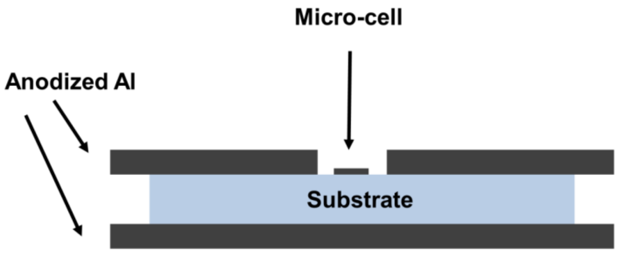

Side view

Top view

Figure 2.7 Anodized Al back cover and aperture set-up.

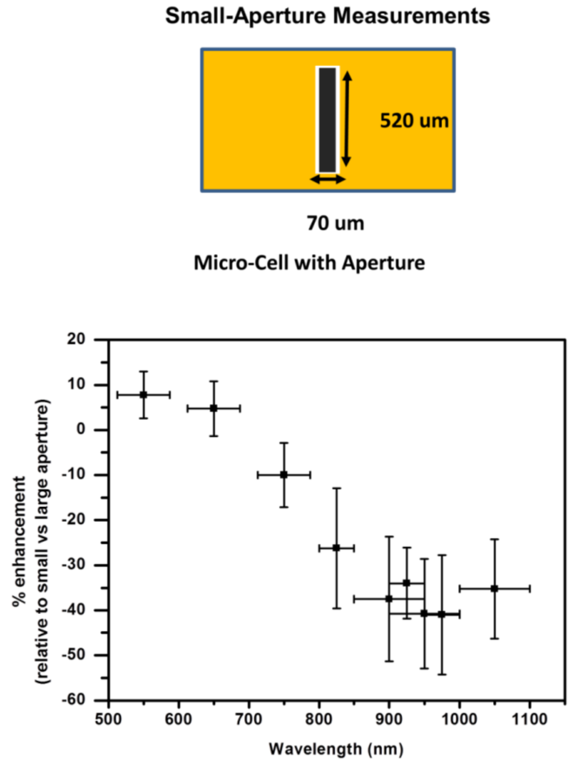

Figure 2.8 Filter measurements with small-area apertures.

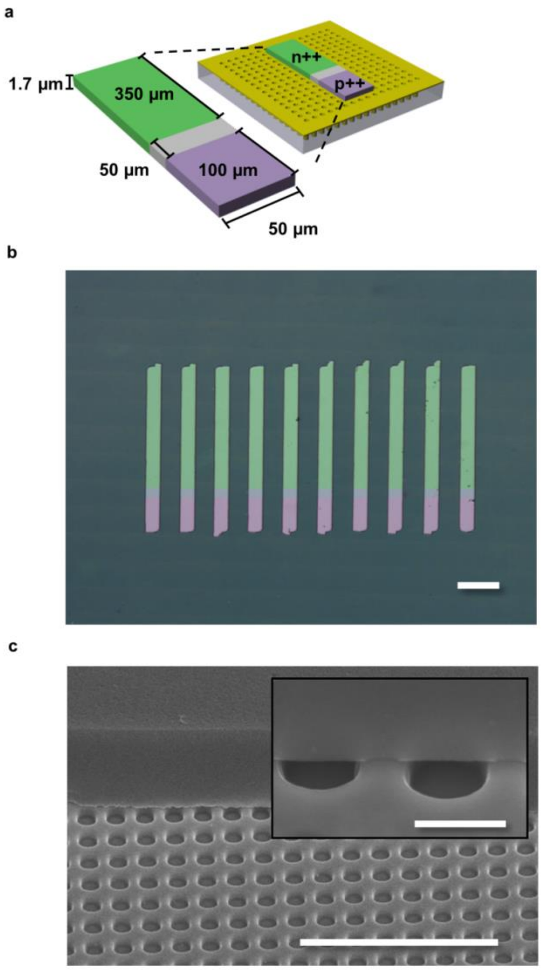

Figure 2.9 Schematic illustration, optical and SEM images of microcells. (a) Illustration of the solar microcell on the surface of the PNR (right) with an enlarged image giving the dimensions of the microcell (left). (b) Images of microcells transferred to the PNR with their doping profiles highlighted in green (n++) and purple (p++). (c) SEM image of a microcell transfer printed to the PNR with the inset showing direct contact of the microcell to the surface of the PNR. White lines in parts (b and c) represents: 100 µm (b); 5 µm (c); and 500 nm (c, insert).

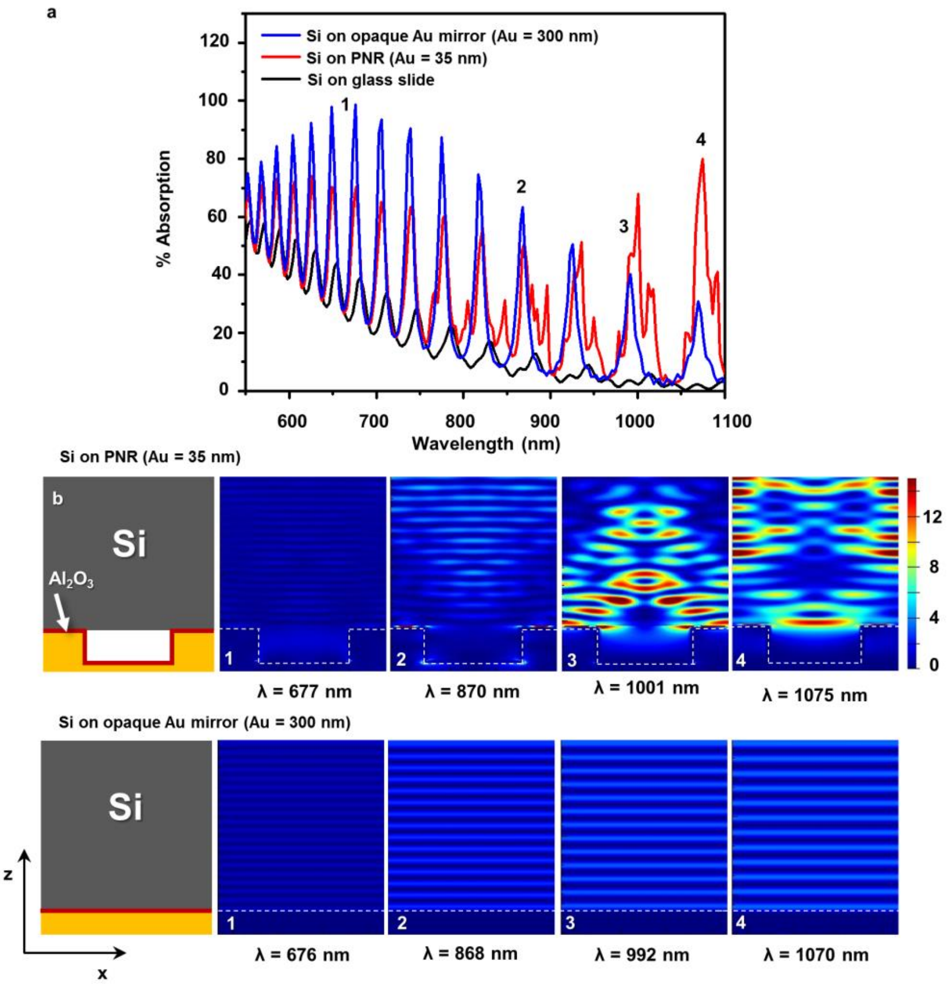

Figure 2.10 FDTD absorption and cross-section images of microcells. (a) FDTD plot depicting the absorption for 1.7 μm thick Si microcell (black), on a 300 nm thick, flat Au backside reflector (blue), and the PNR (red). (b) Illustrations of each modeled system along with cross-sectional (X-Z) images computed with FDTD of the electric field distribution of one unit cell for a microcell on the surface of the PNR (top) and the flat, Au backside reflector (bottom). The simulations were performed with 10 nm of Al_2O_3 (outlined in red in each illustration) between each backside reflector and the microcell. The white region for the PNR case (b) represents an air-gap between the Si microcell and the PNR interface. The PNR was modeled to have a relief depth of 380 nm, a hole pitch of Λ = 740 nm, and a hole diameter of 440nm. Images are shown for wavelengths around 676 nm (point 1), 870 nm (point 2), 1000 nm (point 3), and 1070 nm (point 4).

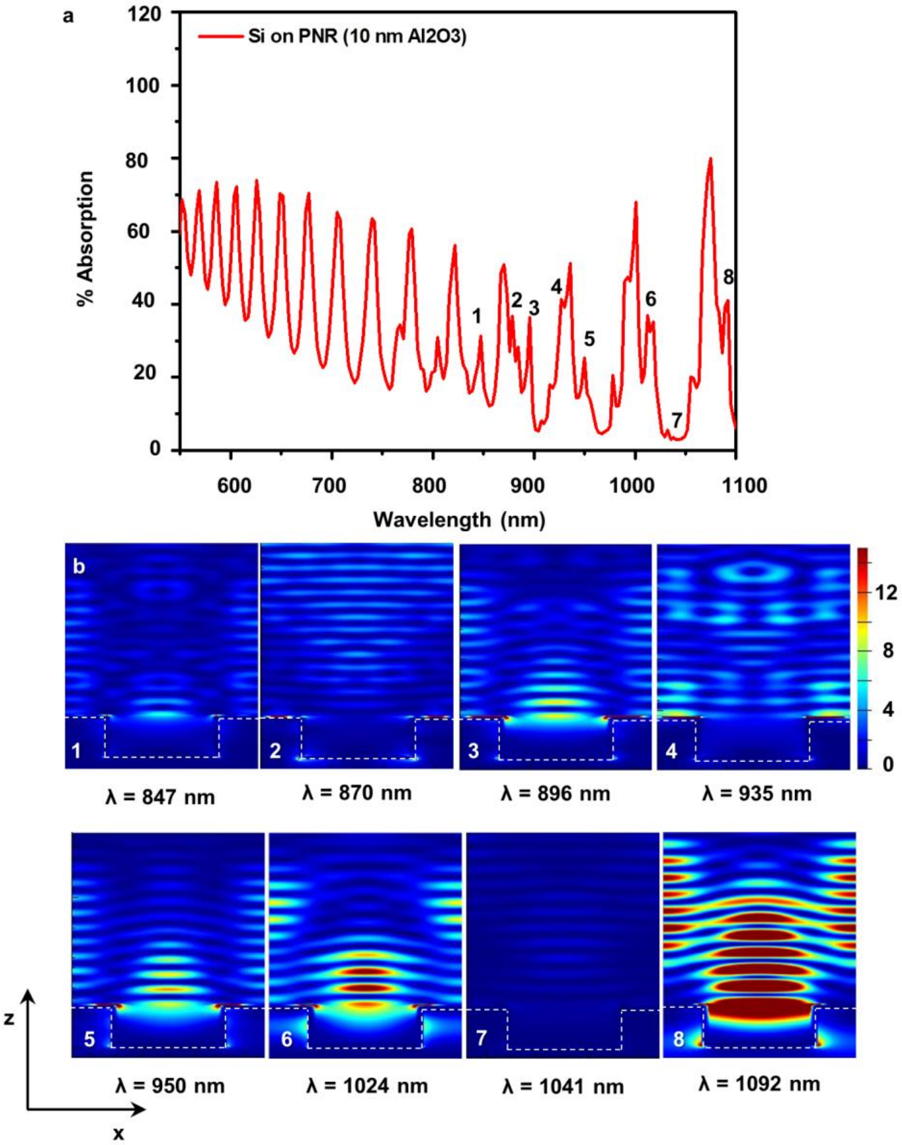

Figure 2.11 FDTD absorption spectra and cross-sectional images. (a) FDTD absorption for silicon on the surface of the PNR with 10 nm of alumina and (b) X-Z cross-sections at 847 (1), 870 (2), 896 (3), 935 (4), 950 (5), 1024 (6), 1041 (7), and 1092 (8) of the silicon on the surface of the PNR. The computational parameters are given in the paper.

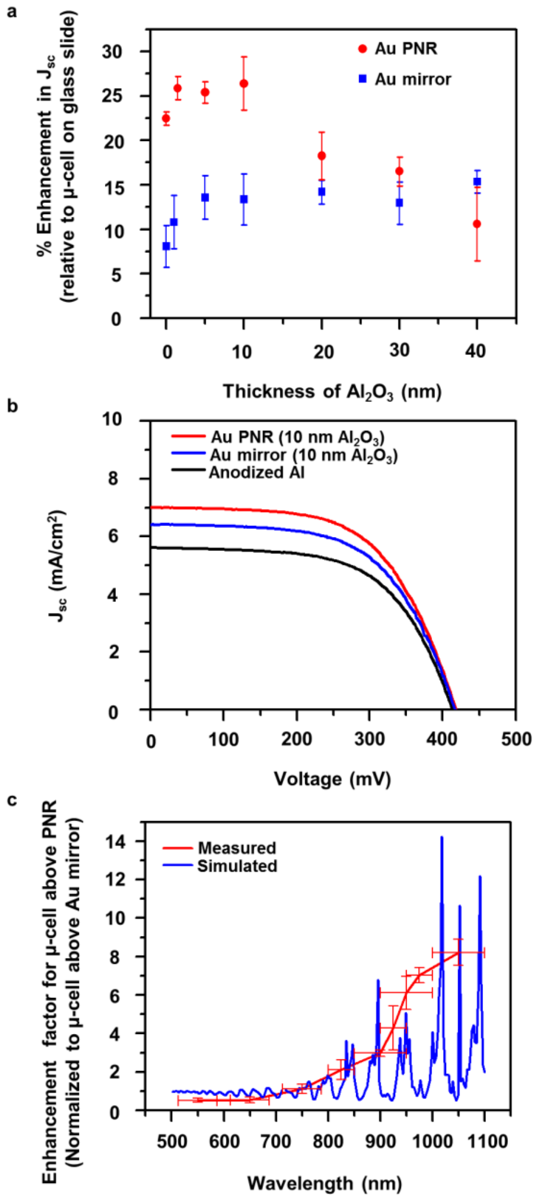

Figure 2.12 J-V measurements of microcells under illumination. (a) Enhancements in the J$_{sc}$ for microcells on the PNR and flat, Au backside reflector as a function Al$_2$O$_3$ spacer layer thickness. Each backside reflector measurement has been normalized to the measurement of the microcell on a glass slide. (b) Representative J-V measurements for microcells on a glass slide (black), PNR (red), and flat Au (blue) with a table giving the important cell parameters. (c) Enhancement factors for filter measurements performed under the solar simulator for microcells on the PNR normalized to microcells on the flat, opaque Au backside reflector (red) with accompanying FDTD results for the Si slab above the PNR normalized to Si slab above the flat, opaque Au (blue). X-axis error bars indicate the wavelength range for the filters while the y-axis error bars indicate sample variance.

Backside Reflector	Eff (%)	V_{oc} (mV)	J_{sc} (mA/cm^2)	FF (%)
Au PNR	1.75	419	7.02	60
Au Mirror	1.59	417	6.42	60
Anodized Al backplate	1.40	410	5.61	61

Table 2.1 Cell Performance as a Function of Backside Reflector

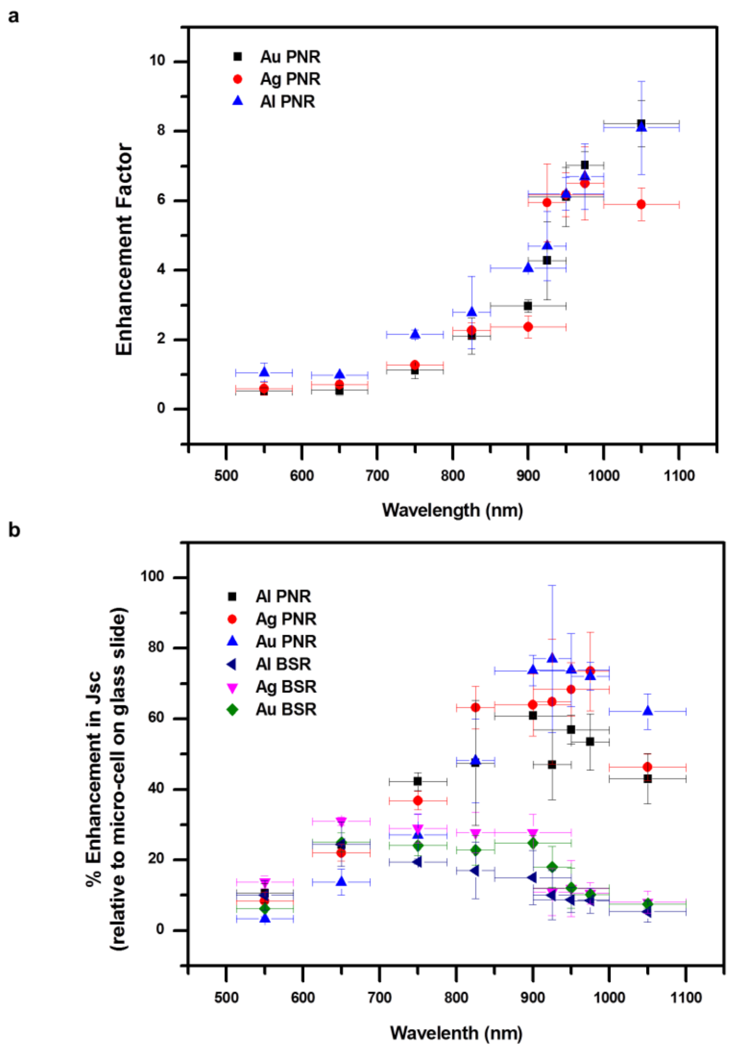

Figure 2.13 Au, Ag, and Al enhancement factor data (a) and PNR and mirror measurements (b).

Filter measurements were performed using the same filters as described in the paper. The decrease in the J_{sc} in the NIR can be attributed to excessive light scattering from the anodized Al backplate when the microcell is first measured on the glass slide. (See supplementary data Fig. S9 for the reflectance spectra of the anodized Al backplate.) The large-area aperture has an opening that enables the anodized Al backplate to scatter more light in the NIR to the microcell when it is on the glass slide. This is in contrast to when the microcell is directly above a metallic backside reflector.

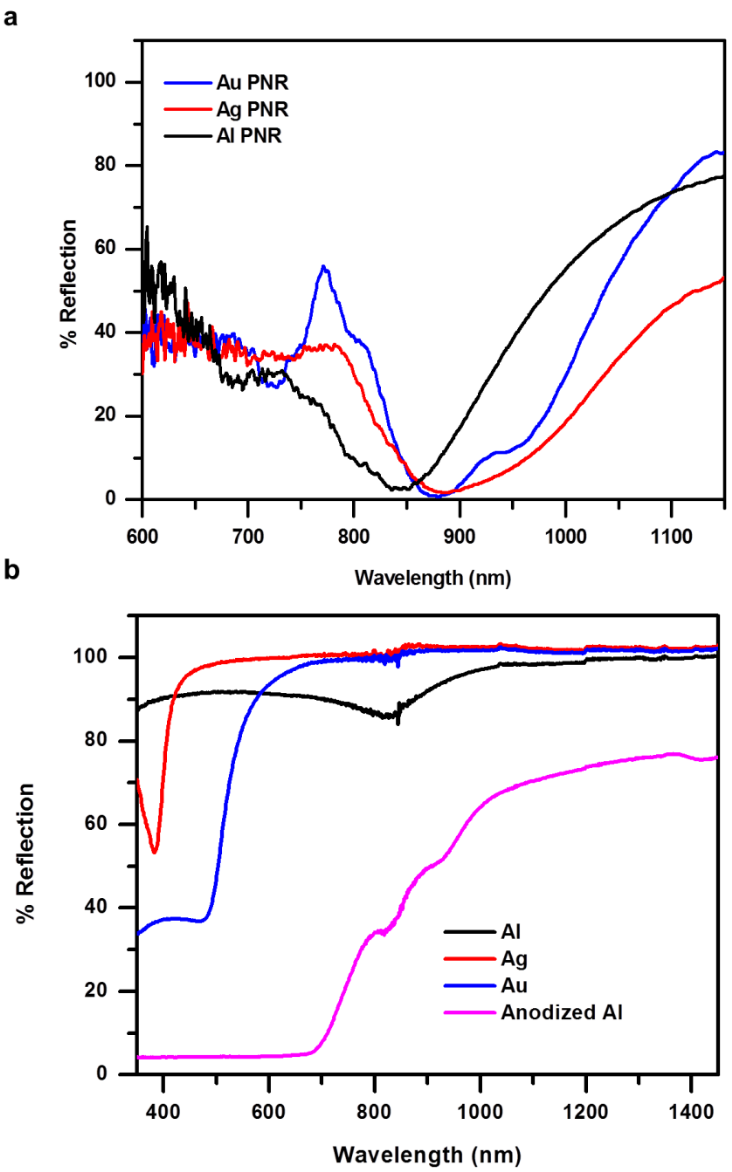

Figure 2.14 Reflection measurements for the mirrors and PNRs. The hole pitch and diameters were all the same and are discussed in the above text. The metals studied were Al, Ag, and Au.

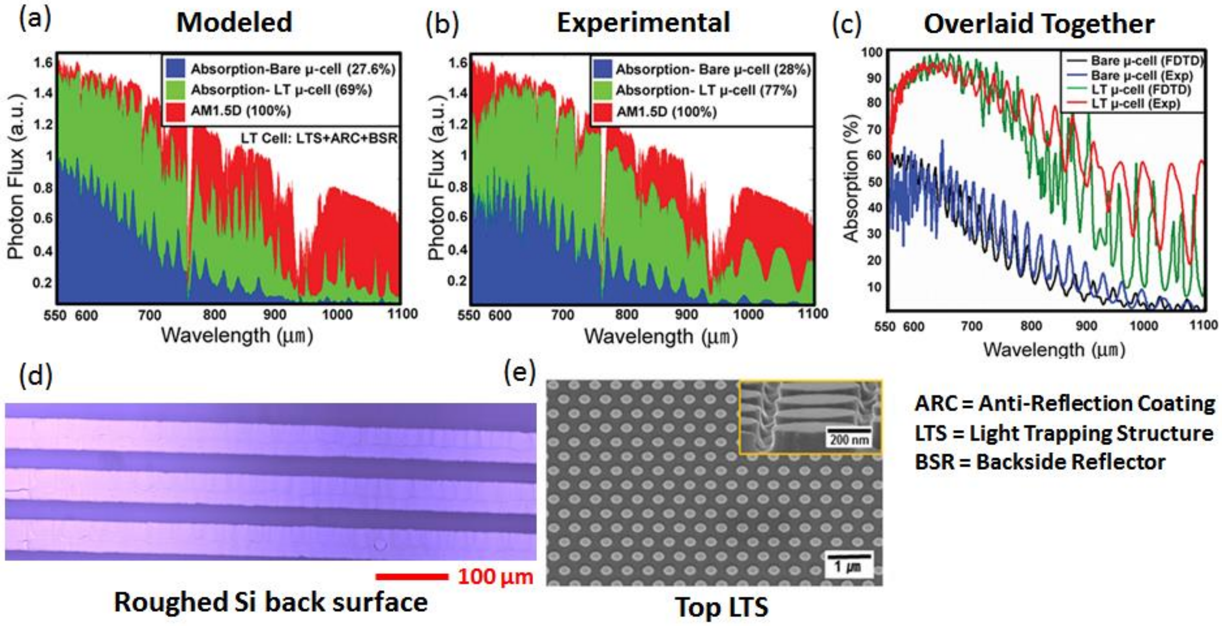

Figure 2.15 Molded (a) and experimental (b) spectra for a bare microcell and a light-trapping (LT) microcell compared to the AM 1.5D solar spectrum. An overlay of the experimental and modeled spectra is given in (c). The cells have imperfections on the back-surface (d) and surface of the light-trapping structure (e) that are a result of the undercutting process and imperfections in the lithography and dry etching steps.

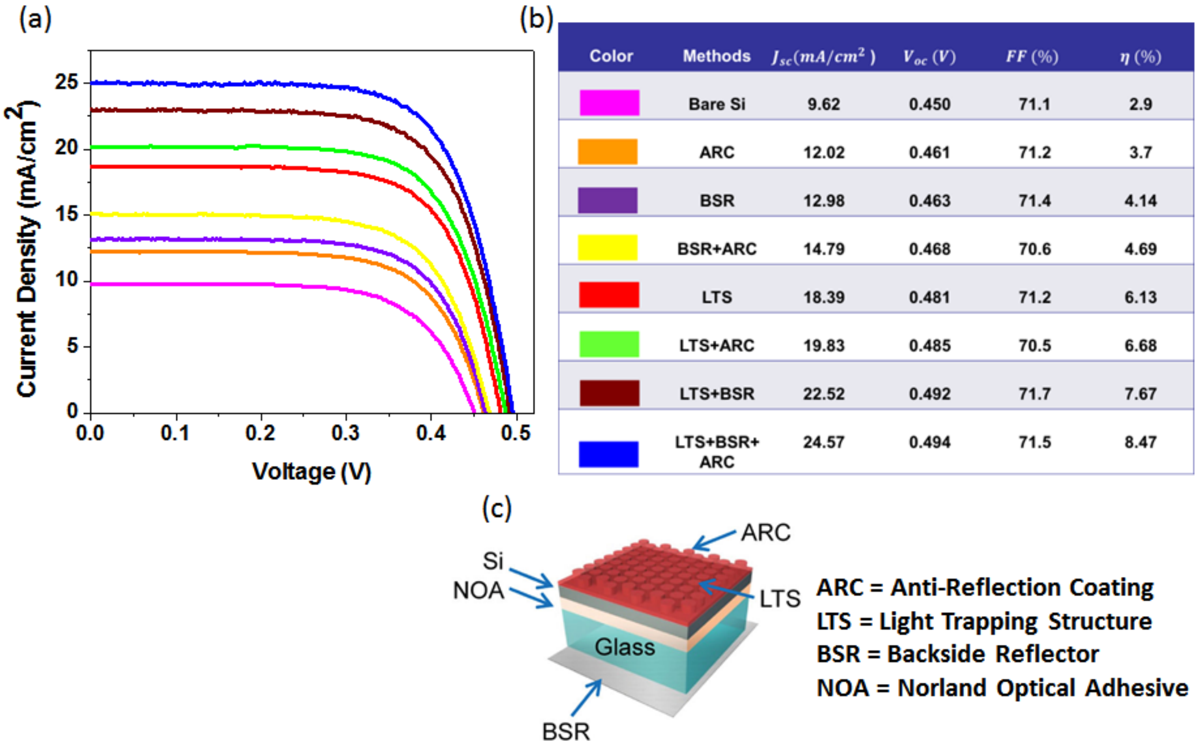

Color	Methods	$J_{sc}(mA/cm^2)$	$V_{oc}\ (V)$	FF (%)	η (%)
🟪	Bare Si	9.62	0.450	71.1	2.9
🟧	ARC	12.02	0.461	71.2	3.7
🟪	BSR	12.98	0.463	71.4	4.14
🟨	BSR+ARC	14.79	0.468	70.6	4.69
🟥	LTS	18.39	0.481	71.2	6.13
🟩	LTS+ARC	19.83	0.485	70.5	6.68
🟫	LTS+BSR	22.52	0.492	71.7	7.67
🟦	LTS+BSR+ ARC	24.57	0.494	71.5	8.47

Figure 2.16 Current-voltage curves (a) and a table listing the key cell parameters (b) for cells with bare Si, an anti-reflective coating (ARC), a backside reflector (BSR), and the light-trapping structure (LTS) as well as combinations of all of these regimes. An image of the microcell with the LTS+BSR+ARC is given in (c).

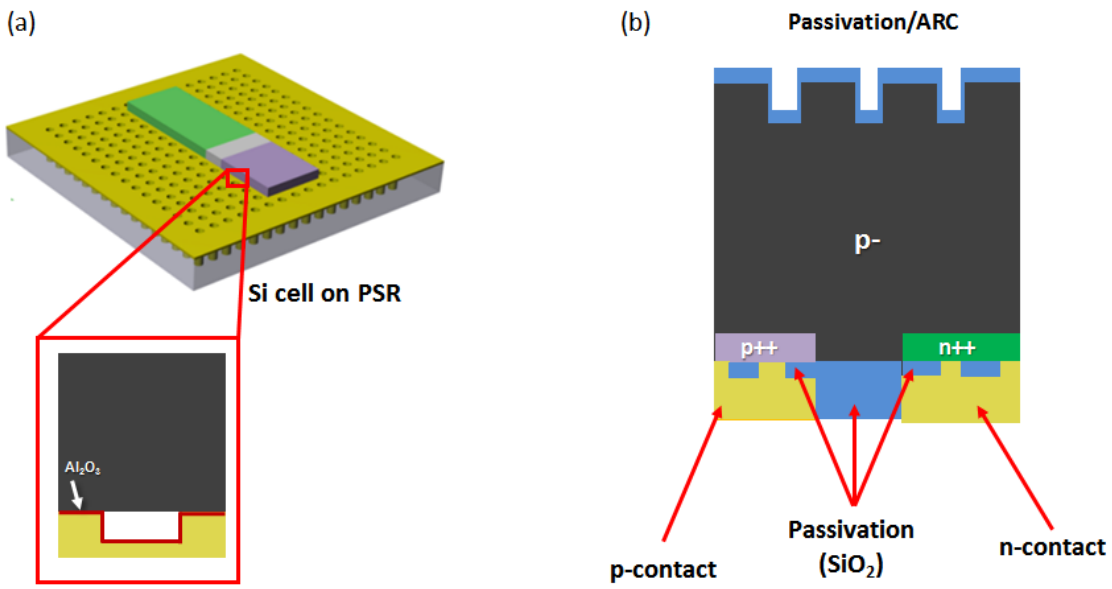

Figure 2.17 Illustrations of a microcell above a periodically nanostructured back-side reflector (a) and a proposed cell structure incorporating an integrated periodically nanostructured reflector as a contact as well as having a surface light trapping structure to reduce the amount of Si needed for the solar cell.

2.8 References

1. Ceccaroli, B. and O. Lohne, *Solar Grade Silicon Feedstock*, in *Handbook of Photovoltaic Science and Engineering -- 2nd Ed.*, A. Luque and S. Hegedus, Editors. 2011, John Wiley & Sons: West Sussex. p. 169-217.

2. Green, M.A. and M.J. Keevers, *Optical Properties of Intrinsic Silicon at 300 K.* Progress in Photovoltaics, 1995. **3**(3): p. 189-192.

3. Jacoboni, C., et al., *Review of Some Charge Transport Properties of Silicon.* Solid-State Electronics, 1977. **20**(2): p. 77-89.

4. Bagnall, D.M. and M. Boreland, *Photovoltaic technologies.* Energy Policy, 2008. **36**(12): p. 4390-4396.

5. Atwater, H.A. and A. Polman, *Plasmonics for improved photovoltaic devices.* Nature Materials, 2010. **9**(10): p. 865-865.

6. Yoon, J., et al., *Ultrathin silicon solar microcells for semitransparent, mechanically flexible and microconcentrator module designs.* Nature Materials, 2008. **7**(11): p. 907-915.

7. Saha, S., et al., *Single heterojunction solar cells on exfoliated flexible similar to 25 mu m thick mono-crystalline silicon substrates.* Applied Physics Letters, 2013. **102**(16).

8. Bedell, S.W., et al., *Kerf-Less Removal of Si, Ge, and III-V Layers by Controlled Spalling to Enable Low-Cost PV Technologies.* Ieee Journal of Photovoltaics, 2012. **2**(2): p. 141-147.

9. Dross, F., et al., *STRESS-INDUCED LIFT-OFF METHOD FOR KERF-LOSS-FREE WAFERING OF ULTRA-THIN (similar to 50 mu m) CRYSTALLINE SI WAFERS*, in *Pvsc: 2008 33rd Ieee Photovoltaic Specialists Conference, Vols 1-4*. 2008, Ieee: New York. p. 1584-1588.

10. Henley, F., et al., *Beam-Induced Wafering Technology for Kerf-Free Thin PV Manufacturing*, in *2009 34th Ieee Photovoltaic Specialists Conference, Vols 1-3*. 2009, Ieee: New York. p. 1715-1720.

11. Shir, D., et al., *Performance of Ultrathin Silicon Solar Microcells with Nanostructures of Relief Formed by Soft Imprint Lithography for Broad Band Absorption Enhancement.* Nano Letters, 2010. **10**(8): p. 3041-3046.

12. Guo, X.Y., et al., *Two- and three-dimensional folding of thin film single-crystalline silicon for photovoltaic power applications.* Proceedings of the National Academy of Sciences of the United States of America, 2009. **106**(48): p. 20149-20154.

13. Yoon, J., et al., *Flexible concentrator photovoltaics based on microscale silicon solar cells embedded in luminescent waveguides.* Nature Communications, 2011. **2**: p. 343.

14. Ferry, V.E., J.N. Munday, and H.A. Atwater, *Design Considerations for Plasmonic Photovoltaics.* Advanced Materials, 2010. **22**(43): p. 4794-4808.

15. Ferry, V.E., et al., *Plasmonic Nanostructure Design for Efficient Light Coupling into Solar Cells.* Nano Letters, 2008. **8**(12): p. 4391-4397.

16. Ferry, V.E., et al., *Optimized Spatial Correlations for Broadband Light Trapping Nanopatterns in High Efficiency Ultrathin Film a-Si:H Solar Cells.* Nano Letters, 2011. **11**(10): p. 4239-4245.

17. Pillai, S., et al., *The effect of dielectric spacer thickness on surface plasmon enhanced solar cells for front and rear side depositions.* Journal of Applied Physics, 2011. **109**(7): p. 073105-8.

18. Pillai, S. and M.A. Green, *Plasmonics for photovoltaic applications.* Solar Energy Materials and Solar Cells, 2010. **94**(9): p. 1481-1486.

19. Wang, C.C.D., et al., *Optical and electrical effects of gold nanoparticles in the active layer of polymer solar cells.* Journal of Materials Chemistry, 2012. **22**(3): p. 1206-1211.

20. Grandidier, J., et al., *Thin-film solar cells: light absorption enhancement in thin-film solar cells using whispering gallery modes in dielectric nanospheres.* Advanced Materials, 2011. **23**(10): p. 1272-76.

21. Yao, Y., et al., *Broadband light management using low-Q whispering gallery modes in spherical nanoshells.* Nature Communications, 2012. **3**.

22. Han, S.E. and G. Chen, *Toward the Lambertian Limit of Light Trapping in Thin Nanostructured Silicon Solar Cells.* Nano Letters, 2010. **10**(11): p. 4692-4696.

23. Mavrokefalos, A., et al., *Efficient Light Trapping in Inverted Nanopyramid Thin Crystalline Silicon Membranes for Solar Cell Applications.* Nano Letters, 2012. **12**(6): p. 2792-2796.

24. Jeong, S., S. Wang, and Y. Cui, *Nanoscale photon management in silicon solar cells.* Journal of Vacuum Science & Technology A: Vacuum, Surfaces, and Films, 2012. **30**(6): p. 060801-11.

25. Kelzenberg, M.D., et al., *Enhanced absorption and carrier collection in Si wire arrays for photovoltaic applications.* Nature Materials, 2010. **9**(3): p. 239-244.

26. Garnett, E. and P. Yang, *Light Trapping in Silicon Nanowire Solar Cells.* Nano Letters, 2010. **10**(3): p. 1082-1087.

27. Ferry, V.E., et al., *Light trapping in ultrathin plasmonic solar cells.* Optics Express, 2010. **18**(13): p. A237-A245.

28. Maria, J., et al., *Optimization of 3D Plasmonic Crystal Structures for Refractive Index Sensing.* Journal of Physical Chemistry C, 2009. **113**(24): p. 10493-10499.

29. Yao, J.M., et al., *Functional Nanostructured Plasmonic Materials.* Advanced Materials, 2010. **22**(10): p. 1102-1110.

30. Zeng, L., et al., *Efficiency enhancement in Si solar cells by textured photonic crystal back reflector.* Applied Physics Letters, 2006. **89**(11).

31. Sheng, X., et al., *Design and Non-Lithographic Fabrication of Light Trapping Structures for Thin Film Silicon Solar Cells.* Advanced Materials, 2011. **23**(7): p. 843-847.

32. Battaglia, C., et al., *Light Trapping in Solar Cells: Can Periodic Beat Random?* Acs Nano, 2012. **6**(3): p. 2790-2797.

33. Hsu, C.M., et al., *High-Efficiency Amorphous Silicon Solar Cell on a Periodic Nanocone Back Reflector.* Advanced Energy Materials, 2012. **2**(6): p. 628-633.

34. Curtin, B., R. Biswas, and V. Dalal, *Photonic crystal based back reflectors for light management and enhanced absorption in amorphous silicon solar cells.* Applied Physics Letters, 2009. **95**(23).

35. Zeng, L., et al., *Demonstration of enhanced absorption in thin film Si solar cells with textured photonic crystal back reflector.* Applied Physics Letters, 2008. **93**(22).

36. Hecht, E., *Optics -- 4th Ed.* 4 ed. 2002, San Francisco: Addison Wesley.

37. Fung, D.D.S., et al., *Optical and electrical properties of efficiency enhanced polymer solar cells with Au nanoparticles in a PEDOT-PSS layer.* Journal of Materials Chemistry, 2011. **21**(41): p. 16349-16356.

38. Feng, X., et al., *Competing Fracture in Kinetically Controlled Transfer Printing.* Langmuir, 2007. **23**(25): p. 12555-12560.

39. Kim, S., et al., *Microstructured elastomeric surfaces with reversible adhesion and examples of their use in deterministic assembly by transfer printing.* Proceedings of the National Academy of Sciences of the United States of America, 2010. **107**(40): p. 17095-17100.

40. Meitl, M.A., et al., *Transfer printing by kinetic control of adhesion to an elastomeric stamp.* Nature Materials, 2006. **5**(1): p. 33-38.

41. Baca, A.J., et al., *Semiconductor wires and ribbons for high-performance flexible electronics.* Angewandte Chemie-International Edition, 2008. **47**(30): p. 5524-5542.

42. Baca, A.J., et al., *Printable single-crystal silicon micro/nanoscale ribbons, platelets and bars generated from bulk wafers.* Advanced Functional Materials, 2007. **17**(16): p. 3051-3062.

43. Meitl, M.A., et al., *Stress focusing for controlled fracture in microelectromechanical systems.* Applied Physics Letters, 2007. **90**(8).

44. Korotcenkov, G. and B.K. Cho, *Silicon Porosification: State of the Art.* Critical Reviews in Solid State and Materials Sciences, 2010. **35**(3): p. 153-260.

45. Yao, J.M., et al., *Seeing molecules by eye: Surface plasmon resonance imaging at visible wavelengths with high spatial resolution and submonolayer sensitivity.* Angewandte Chemie-International Edition, 2008. **47**(27): p. 5013-5017.

46. Rockett, A., *The Materials Science of Semiconductors*. 2008, New York: Springer.

47. Gary, S.K. and T. Kupka, *Propogation of Light in Metallic Nanowire Arrays: Finite-Difference Time-Domain Studies of Silver Cylinders.* Physical Review B, 2003. **68**: p. 045415.

48. Emery, K., *Measurement and Characterization of Solar Cells and Modules*, in *Handbook of Photovoltaic Science and Engineering -- 2nd Ed.*, A. Luque and S. Hegedus, Editors. 2011, John Wiley & Sons: West Sussex. p. 797-834.

49. Nelson, J., *Physics of Solar Cells*. 2003, London: Imperial College Press. 10-11.

50. Green, M.A., *Silicon Solar-Cells - Evolution, High-Efficiency Design and Efficiency Enahancements.* Semiconductor Science and Technology, 1993. **8**(1): p. 1-12.

51. Wenham, S.R. and M.A. Green, *Silicon solar cells.* Progress in Photovoltaics, 1996. **4**(1): p. 3-33.

52. Yao, Y., et al., *Fabrication and assembly of ultrathin high-efficiency silicon solar microcells integrating electrical passivation and anti-reflection coatings.* Energy & Environmental Science, 2013. **6**(10): p. 3071-3079.

53. Mulvaney, P., *Surface Plasmon Spectroscopy of Nanosized Metal Particles.* Langmuir, 1996. **12**(3): p. 788-800.

54. Link, S. and M.A. El-Sayed, *Spectral Properties and Relaxation Dynamics of Surface Plasmon Electronic Oscillations in Gold and Silver Nanodots and Nanorods.* Journal of Physical Chemistry B, 1999. **103**(40): p. 8410-8426.

55. Gao, H.W., et al., *Screening plasmonic materials using pyramidal gratings.* Proceedings of the National Academy of Sciences of the United States of America, 2008. **105**(51): p. 20146-20151.

56. Green, M.A., *SILICON SOLAR-CELLS - EVOLUTION, HIGH-EFFICIENCY DESIGN AND EFFICIENCY ENHANCEMENTS.* Semiconductor Science and Technology, 1993. **8**(1): p. 1-12.

57. Green, M.A., *Silicon solar cells: state of the art.* Philosophical Transactions of the Royal Society a-Mathematical Physical and Engineering Sciences, 2013. **371**(1996).

58. Suwito, D., et al., *Industrially Feasible Rear Passivation and Contacting Scheme for High-Efficiency n-Type Solar Cells Yielding a V(oc) of 700 mV.* Ieee Transactions on Electron Devices, 2010. **57**(8): p. 2032-2036.

59. Ok, Y.W., et al., *Understanding of a-Si:H(p)/c-Si(n) heterojunction solar cell through analysis of cells with point-contacted p/n junction.* Current Applied Physics, 2009. **9**(6): p. 1186-1190.

60. Swanson, R.M., et al., *POINT-CONTACT SILICON SOLAR-CELLS.* Ieee Transactions on Electron Devices, 1984. **31**(5): p. 661-664.

61. Taguchi, M., et al., *HIT (TM) cells - High-efficiency crystalline Si cells with novel structure.* Progress in Photovoltaics, 2000. **8**(5): p. 503-513.

62. Mishima, T., et al., *Development status of high-efficiency HIT solar cells.* Solar Energy Materials and Solar Cells, 2011. **95**(1): p. 18-21.

63. Taguchi, M., et al., *Obtaining a higher V-oc in HIT cells.* Progress in Photovoltaics, 2005. **13**(6): p. 481-488.

Chapter 3

Fabrication and Characterization of InGaP and GaAs Solar Microcells under One Sun and Concentrated Light

3.1 Abstract

This chapter focuses on the design principles, fabrication, and characterization of III-V solar microcells – specifically, InGaP and GaAs solar microcells. Here the term "microcells" is used to define solar cells that are approximately 600 x 600 µm^2 in size. The chapter will begin with an overview of each epilayer and the rationale behind its design. Fabrication of these devices will then be discussed in great detail accompanied by examination of cell performance – with key solar cell parameters surveyed – under one sun and concentrated sunlight.

3.2 Introduction

III-V semiconductors such as InGaP and GaAs have advantages over Si devices such as direct band gaps and their potential for large external radiative efficiency values [1, 2]. As such, they have the potential for extremely high energy conversion efficiencies. A thin-flim GaAs cell holds the record single junction efficiency at 28.8% under standard test conditions [3] and InGaP cells have been tailored to reach efficiency values past 20% [2].

Figure 3.1 is an outline of the InGaP epi-stack used for the experiments discussed herein. Unlike Si solar cells, III-V solar cells consist of epi-layers that have different band gaps for the various parts of the cell; wider band gap materials are used for the backsurface field and window layers and each epi-layer in the solar cell must be carefully lattice matched to the parent epi-wafer in order to reduce growth defects. This last aspect greatly limits the choice of available materials for compound semiconductor solar cells. If materials were grown without low defects, their efficiency values would be greatly reduced from their optimal values and no real benefit to using III-V materials as solar cells would be gained. The band gaps for the different layers are often created by varying the composition in ternary and quaternary alloys. These multilayer structures may be produced either from Metal-Organic Chemical Vapor Deposition (MOCVD), Liquid Phase Epitaxy (LPE), as well as Molecular Beam Epitaxy (MBE). MOCVD growths have improved in quality over the years and have proven to achieve the best economics of growth that are also combined with high crystal perfection, homogeneity, and interface control [4].

3.2.1 Compound Semiconductor Microcells

The sizes of the III-V solar cells in this thesis are on the order of 600 x 600 μm^2. Miniaturization of these devices presents opportunities for having small, compact form factors that can achieve high energy conversion efficiencies along with more efficient utilization of semi-precious and expensive materials which compose the solar cell. When the thickness of a solar cell is reduced, collection of the free carriers is improved. This aspect of a thinner cell can lead to better short-circuit current and open-circuit voltage parameters – improving the overall light conversion efficiency of the cell. This, of course, assumes the cell is thick enough to collect a majority of the photons. There are drawbacks, however, to having micro-scale (length and width) devices. The increased cell surface area will result in more recombination along the edges of the device. As such, it is impractical to work cells that have unpassivated sidewalls operating at one sun. To better exploit thin-film microcells, it is better to work with these devices under concentrated sunlight. In concentrator systems where the cells can be working in the high-carrier injection limit; that is, with increasing light irradiance, at some point it is possible for the free carrier density to exceed the dopant density – the number of free electrons is equal to the number of free holes ($\Delta n = \Delta p >> n_0$ or p_0). When the amount of generated carriers is greater than the background dopant density of the material, the primary method of recombination becomes Auger recombination and sidewall recombination becomes negligible. It is possible to work with devices ~ 600 x 600 μm^2 in a concentration regime of ~1100 suns [5, 6]. This avenue presents opportunities more effective utilization of photovoltaic materials that can reduce the overall cost of the concentrator system. As an additional benefit, concentration also improves solar cell energy conversion efficiency.

3.2.2 Epitaxial Lift-Off Technique

The method in which the microcells are removed from the host wafer is a method that has been around for many years known as the epitaxial lift-off technique. The method has been used for a while with GaAs cells [7-10], but has also been tried with other materials [11-14]. The sacrificial material is AlAs. A small amount of gallium is present (usually it is $Al_{0.96}Ga_{0.04}As$) to have the sacrificial layer lattice matched to the GaAs substrate. Immersion of the sample in HF acid is known to etch the AlAs layer at a very high etch rate; etch rates can be greater than ~1 mm an hour at room temperature. Occasionally some of the epi-layers in the stack can be attacked by HF [15]. In these cases, photoresist can serve as an etch barrier – or coating the device with another substance that is resistant to HF – to help passivate the device during etching. Here, $Al_{0.96}Ga_{0.04}As$ (henceforth known as AlAs) is the sacrificial material employed to selectively remove InGaP and GaAs solar cells from GaAs host wafers. The AlAs layer is 500 nm as thicker layers are known to have higher etch rates [15, 16].

3.3 Materials and Methods

3.3.1 InGaP Solar Cell Epi-Stack

Figure 3.1 is an outline of the InGaP epi-stack. The epi-layers are formed by growth on a gallium arsenide (GaAs) wafer (GaAs (100) 10° off (111) plane) grown by metal-organic chemical vapor deposition. Massimo Semicondutor was the company that provided the growth using preset conditions from their solar cell epi-layers. For a deeper discussion such as the reason for the specific p- and n-type dopants and for a history of InGaP-based solar cells, readers are encouraged to look at reference [17]. The structure (from bottom to top) consists of 500 nm AlAs layer for sacrificial etching; an intrinsic InGaP layer that is 1 µm thick to help facilitate transfer printing; a 100 nm thick GaAs layer acting as the p-contact (Zn doped, $p > 1 \times 10^{19} cm^{-3}$); this dopant density assists in forming ohmic contacts with high workfuction metals such as Au. The p-layer is only 100 nm thick which offers the potential for fabricating bifacial devices, as well. An $Al_{0.25}In_{0.50}Ga_{0.25}P$ (henceforth known as AlInGaP) layer acts as the back-surface field (Zn doped, $p \sim 8 \times 10^{17} cm^{-3}$). This layer consists of a wider band gap material and greater dopant density than the InGaP base layer to help repel minority carriers – in this case electrons – from the high recombination rear contact. The 1.3 µm $In_{0.50}Ga_{0.50}P$ (InGaP) base layer serves as the absorbing layer (Zn, $p \sim 3 \times 10^{16} cm^{-3}$). This doping concentration serves as a balance to allow for effective absorption of light and also diffusion of the free-carriers to their respective contacts. A 100 nm thick $In_{0.50}Ga_{0.50}P$ emitter (Si, $n \sim 2 \times 10^{18}$ cm^{-3}) to form the p-n junction and a 40 nm thick $Al_{0.25}In_{0.50}Ga_{0.25}P$ window (Si, $n \sim 4 \times 10^{18}$ cm^{-3}). The cap layer consists of a 100 nm thick GaAs contacting layer (Si, $n \sim 4.5 \times 10^{18}$ cm^{-3}); and a highly doped layer of GaAs (Te, $n > 1 \times 10^{19}$ cm^{-3}) to allow for formation of ohmic contacts using lower workfunction materials such as Ti or Ge. These doping conditions are optimal for minimizing electrical resistance yet the doping levels are set up to minimize carrier recombination. Traditionally InGaP cells are used in multijunction solar cells where the window layer is $Al_{0.50}In_{0.50}P$ [17-19]. In this case AlInGaP was chosen as the window layer for two reasons; it was chosen because (1) it has a greater resistance to etching in HF [15] than $Al_{0.50}In_{0.50}P$ and has been used in (2) previous record-efficiency multijunction devices [20]. The InGaP emitter/base layers grown here have a band gap of ~ 1.9 eV suggesting a disordered InGaP layer [21, 22]. This does not affect the performance of the devices, but rather makes the band gap wider; traditionally InGaP MOCVD growths can range from 1.8 eV to 1.91 eV depending on the growth conditions [17]. The bottom InGaP layer above the AlAs layer serves as a supporting layer to help facilitate transfer printing. Because InGaP solar cell fabrication involves both contacts facing the top surface, and since the bottom p-contact layer is only 100 nm, the 1 µm of InGaP serves as a support layer when transfer printing InGaP cells to foreign substrates. Otherwise, the 100 nm p-layer could easily tear during transfer printing.

3.3.2 GaAs Solar Cell Epi-Stack

Figure 3.2 is an outline of the GaAs epi-stack. The various epi-layers are grown on top of GaAs wafer [n-type GaAs, (100 10° of towards the (110)] by metal-organic chemical vapor deposition in a similar manner to the InGaP cell. For a more thorough discussion of the GaAs cell overview, please see reference [17]. Massimo Semicondutor was the company that provided the growth using preset conditions from their solar cell epi-layers. The structure (from bottom to top) consists of 500 nm AlAs layer for sacrificial etching; an intrinsic InGaP layer that is 700 nm thick to help facilitate transfer printing; a 300 nm thick GaAs layer acting as the p-contact (Zn doped, $p \sim 3.8 \times 10^{19} cm^{-3}$); an $Al_{0.30}Ga_{0.70}As$ layer acting as the back-surface field (Zn doped, $p \sim 8 \times 10^{18} cm^{-3}$); a 2.5 µm GaAs base layer serving as the absorbing layer (Zn, $p \sim 1 \times 10^{17} cm^{-3}$); a

100 nm thick GaAs emitter (Si, n ~ 2 x 10^{18} cm^{-3}); a 25 nm thick $In_{0.50}Ga_{0.50}P$ window (Si, n ~ 2 x 10^{18} cm^{-3}); a 100 nm thick GaAs contacting layer (Si, n ~ 2 x 10^{18} cm^{-3}); and a highly doped cap layer of 100 nm GaAs (Te, n > 1 x $10^{19}$$cm^{-3}$). These doping conditions are optimal for minimizing electrical resistance yet the doping is set up to reduce carrier recombination by allowing long enough path lengths. The InGaP window layer was chosen because the InGaP/GaAs interface has one of the lowest recombination velocities, and thus provides for excellent surface passivation [23]. The AlGaAs backsurface field was chosen since for three reasons: (1) it has a wider band gap (E_g ~2 eV) than InGaP, (2) can be selectivity etch with different ratios of citric acid:hydrogen peroxide, and (3) can still maintain a highly structured morphology at higher p-doping concentrations than InGaP [24].

3.3.3 Wet Etchants

Many selective and non-selective etchants exist for processing III-V devices. For InGaP- and GaAs-based solar cells, there are multiple etchants that may be used to tune selectivity for device processing [25]:

- Mixtures of ammonia, hydrogen peroxide, and water etch GaAs but do not etch InGaP (or AlInGaP). A (2:1:10) of $NH_4OH:H_2O_2:H_2O$ that etches GaAs is one common formulation [26].
- Concentrated HCl acid rapidly etches AlInGaP and InGaP but does not etch GaAs [27]. HCl acid may be diluted with water to slow down the etch rate of InGaP-based materials. Dilluting the solution too much, however, will make it unable to etch InGaP. In general, HCl is known to etch phosphide-based materials and H_3PO_4 is known to etch arsenide-based materials [28, 29].

- A mixture of phosphoric acid, hydrogen peroxide, and water etches GaAs, but does not etch InGaP-based materials. Various formulations are present; two common recipes are (1:13:12) etch rate of ~40 nm/s and (3:1:25) etch rate of 140 nm/min [30].
- A mixture of sulfuric acid, hydrogen peroxide, and water – basically piranha [31] – in a ratio of (1:8:80) has an etch rate of 8 nm/s [32].
- Citric acid and hydrogen peroxide in various combinations will etch GaAs, but not etch AlGaAs layers [33]. This is a common etch-stop routine. This process also does not etch InGaP.

There are many formulations which can be found in the literature [25]. Table 3.1 gives the various etchant ratios for citric acid and hydrogen peroxide and their etch rates. Wet etching formulations are suitable for processing microcells of our size regime making dry etching techniques unnecessary. All of these etching solutions were thoroughly mixed and set aside for 15 minutes after mixing to allow the solutions to equilibriate to room temperature. Etching solutions were kept fresh to avoid any reproducibility issues. Specific formulations for etching each epi-stack will be discussed in more detail in the device fabrication sections that follow.

3.3.4 InGaP Cell Fabrication

The InGaP cell is designed for removal from the wafer because of a thin layer of AlAs can be sacrificially etched away. The cells can be integrated onto foreign substrates using techniques of epitaxial lift-off and transfer printing. Figure 3.3 details the fabrication of the InGaP cells in detail. The cells are lithographically fabricated and etched with wet etchants by the following process: (1) the InGaP substrate is photolithographically patterned with photoreisist (AZ 5214, Clariant) and selective wet etchants etch down to the p-type GaAs layer;

to etch the GaAs cap layer, H_3PO_4 (85 wt% in water):H_2O_2 (30 wt% in water):H_2O (1:13:12) was used and etches down to the AlInGaP window layer; once at the AlInGaP window layer, (2) concentrated HCl acid (36 wt% in water) etches the AlInGaP window/back-surface field and InGaP layers to stop at the GaAs p-contact; another photolithographic pattern (AZ 5214, Clariant) is applied to the wafer and (3) the phosphoric acid etchant is again used followed by HCl to etch the InGaP layer and reveal the AlAs layer. (The lower InGaP layer takes ~15 s to etch in HCl.) At this point metal contacts are deposited (4) with Ti/Au (or Cr/Au;10nm/~200 nm) for the n-contact and Au (~200 nm) for the p-contact by two lift-off steps (AZ 2020, Clariant). The cells are then encapsulated in SPR 220 v4.5 (5) and the cells are undercut in an ethanol-rich hydrofluoric acid solution (49% HF, Transene; HF:ethanol = 1:1.5 by volume) to undercut the cells. The ethanol in the HF solution serves to reduce bubble formation so that greater HF concentrations could be used to enhance the AlAs etch rate. Indivdual InGaP cells can be lifted off the surface by a polydimethylsiloxane (PDMS) stamp and transfer printed to glassed slides (6) with a thin layer of SU-8 2002 (Microchem) acting as the adhesive. The cap layer is then removed by the phosphoric acid etchant solution with another photoresist layer protecting the p-type GaAs. The cap layer is kept on the surface during the HF undercut step because fluoride ions in HF are known to be able to penetrate photoresist [34] and, in this case, attack the AlInGaP window layer [15]. (During studies when the fabrication had the AlInGaP window layer covered by photoresist, excessive delamination was observed. This delamination did not occur when the GaAs cap layer was covered by photoresist. This suggests that the AlInGaP window layer is partially [or completely] etched by HF during the undercutting step.) HF penetrating and etching the window layer can be remedied by using small, thin-flm coatings – such as anti-reflective coatings – which are impervious to HF attack. Another method would be to use a different etchant material such as AlInP, which has been shown to have a high etch rate in HCl [35].

3.3.5 InGaP Etching Issues

There is a major issue with etching InGaP cells that can cause problems with device integrity. The problem deals with the wet etching behavior of InGaP and AlInGaP layers. HCl-based solutions are used for wet etching of these layers [36, 37]. Figures 3.4 a and b show the severe under-etching of InGaP/AlInGaP etched by HCl and being protected by a photoresist mask. From reference [38], InGaP wet etching in concentrated HCl, the etch rate at 20°C has a two-fold rotational symmetry about [100] and etch rates can vary between planes. This issue is not too serious for structures hundreds of microns in size (length and width) and only microns in thickness, but it can present problems. Solutions to this issue include that, when depositing the photoresist mask for mesa etching, the mesa orientation is positioned 45° off axis. In this case, the under etching becomes less apparent. Another solution, the solution I have implemented for device fabrication, is to keep the GaAs cap layer on the surface during mesa etching. This remedies the problem and only the corners of the cell are etched – as shown in Figure 3.4 c.

3.3.6 Photolithography Processes

Photolithography using AZ 5214

a. Spin-coat at 3000 rpm for 30 seconds to form a film ~ 1.5 µm thick.

b. Pre-bake at 110°C for 60 seconds to drive off volatile organic solvents

c. Exposure dose of 135 mJ/cm^2 at 365nm.

d. Develop in 917 developer.

e. Hard bake at 110°C for ~ 1 min.

Photolithography using AZ 2020

a. Spin-coat at 3000 rpm for 30 seconds to form a film ~2 µm thick layer of photoresist.

b. Pre-bake at 110°C for 60 seconds to drive off volatile organic solvents

c. Exposure dose of 135 mJ/cm^2 at 365nm.

d. Develop in 917 developer.

e. Hard bake at 110°C for ~ 1 min.

Photolithography using SPR 220 v 4.5

a. Spin-coat at 3000 rpm for 30 seconds to form a film ~ >4.5 µm thick.

b. Pre-bake at 110°C for 60 seconds to drive off volatile organic solvents

c. Exposure dose of 135 mJ/cm^2 at 365nm.

d. Develop in 400K developer developer diluted in water (5:1 = water:developer).

e. Hard bake at 125°C for ~ 10 min to allow the photoresist to reflow; **THIS REFLOW STEP IS CRUCIAL FOR UNDERCUTTING THE CHIPLETS.**

3.3.7 GaAs Cell Fabrication

Fabrication for both p- and n-contacts on the top of the cell followed a similar fabrication strategy as the aforementioned InGaP cells. The only difference was the etchants used. The cells are lithographically fabricated and etched with wet etchants in the following process: the

GaAs substrate is photolithographically patterned with photoreisist (AZ 5214, Clariant) and selective wet etchants etch down to the p-type GaAs layer (Figure 3.2); to etch the GaAs cap layer, H_3PO_4 (85 wt% in water):H_2O_2 (30 wt% in water):H_2O (1:13:12) is used and etches down to the InGaP window layer; once at the InGaP window layer, concentrated HCl acid (36 wt% in water) etches the InGaP window layer to the GaAs emitter; at this point a 3:1 ratio (citric acid:hydrogen peroxide) is used to etch down to the $Al_{0.3}Ga_{0.7}As$ backsurface field (roughly 11 to 12 min. at room temperature); at this stage a 10:1 (citric acid:hydrogen peroxide) solution is used to etch through the $Al_{0.3}Ga_{0.7}As$ layer and to etch a bit of the GaAs p-contact (~ 1 min); another photolithographic pattern (AZ 5214, Clariant) is applied to the wafer and the phosphoric acid etchant is again used followed by HCl to etch the InGaP layer and reveal the AlAs layer. At this point the metal contacts are deposited with Ti/Au (or Cr/Au; 10nm/~200 nm) for the n-contact and Au (~200 nm) for the p-contact by two lift-off steps (AZ 2020, Clariant). The cells are then encapsulated in SPR 220 v4.5 and the cells are undercut in an ethanol-rich hydrofluoric (HF) acid solution (HF:ethanol = 1:1.5 by volume). The ethanol in the HF solution served to reduce bubble formation so that greater HF concentrations could be used to enhance the AlAs etch rate; typical undercutting times for a 650 µm wide device is roughly one hour. While there has been no investigation into this phenomenon in the literature, it is believed that the ethanol helps reduce bubble formation and, therefore, preserves the integrity of the fragile III-V materials during the etching process. Individual GaAs cells can be lifted off the surface by a polydimethylsiloxane (PDMS) stamp and transfer printed to glassed slides with a thin layer of SU-8 2002 (Microchem) acting as the adhesive. The cap layer is then removed by the phosphoric acid etchant solution with another photoresist layer protecting the p-type GaAs. The process yielded cells with inconsistent results. The current-voltage curves would have a significant amount of series resistance. The most probable reason for this inconsistent performance (and extremely high series resistance) is the potential for non-uniform etching to the AlGaAs layer. This can be overcome by placing the p-contact on the bottom of the cell, or working with different etchants. For example, a 3:1:25 of H_3PO_4:H_2O_2:H_2O can be used to time the etch until it etches past the AlGaAs layer and ~50 nm into the p-contact. The strategy I have chosen to take is to place the p-contact on the back-surface of the solar cell.

3.3.8 GaAs with P-Contact on the Back Surface

Cell fabrication with a p-contact on the backside of the cell is shown in Figure 3.5. The cells are lithographically fabricated and etched with wet etchants in the following process: (1) the GaAs substrate is photolithographically patterned with photoreisist (AZ 5214, Clariant) and a wet etch with H_3PO_4 (85 wt% in water):H_2O_2 (30 wt% in water):H_2O (1:13:12) is then used to etch down to the InGaP window layer; once at the InGaP window layer, concentrated HCl acid (36 wt% in water) etches the InGaP and the phosphoric acid solution is then used to etch all the GaAs down to the lower InGaP layer; HCl then etches the last InGaP layer to expose the AlAs (1). At this point the top metal contact is deposited (2) with Ti/Au or Cr/Au (10nm/~200 nm) for the n-contact by a lift-off step (AZ 2020, Clariant). The cells are then encapsulated in SPR 220 v4.5 (3) and the cells are undercut in an ethanol-rich hydrofluoric (HF) acid solution (HF:ethanol = 1:1.5 by volume) to undercut the cells. Individual GaAs cells are then transferred to a PDMS stamp to have the InGaP layer removed with HCl (etching takes ~25 s) and the bottom contact is deposited with Au (~ 200 nm; 4). After contact deposition, the cell is transfer printed to a glass slide with a thin layer of SU-8 2002 (Microchem) acting as the adhesive. The bottom p-contact as well as the cap layer are then removed by the phosphoric acid etchant solution (5).

3.3.9 Cell Encapsulation for Large-Area Contacts

In order to measure the solar cells with alligator clips and to minimize problems probing the solar cells on soft surfaces, devices were encapsulated and had large-area contacts deposited (unless otherwise noted). A 2 mm thick layer of photocurable epoxy (SU-8 2002, MicroChem) acts as an adhesive to facilitate transfer printing of the microcell to the glass substrate. The sidewalls of the cell are then coated another ~2 μm thick layer of a photocurable epoxy (SU-8 2002, MicroChem). (Note: sometimes residual SU-8 remains on the surface of the device. Samples with residual SU-8 were etched in oxygen plasma.) Following this sidewall coverage, the portions of the cell are then covered with another photocurable epoxy ~500 nm thick (SU-8 2000.5, MicroChem). Large-area metal contacts of Cr/Cu/Au (10 nm/500 nm – 1 μm/10 nm) are used for electrical interconnection that are created through lift-off using AZ 2070. SU-8 is a negative-tone photoresist that is extremely versatile and is capable of forming tapered sidewalls. The sidewalls of the final encapsulated device were sloped as to allow for deposited contacts to have very low series resistance. Sputtering contacts in this manner is the technique for minimizing resistance issues as sidewall definition has a huge impact on the uniformity of the deposition. A device as well as an illustration of an encapsulated device is presented in Figure 3.6a and b. The process flow was the following:

a. Spin coat SU-8 2002 on a glass slide a 3000 RPM for ~15 s
b. Partially sure the SU-2002 under UV light (365 nm @ ~ 18mW/cm^2) for ~ 5 s (note: This partial curing stage can be shorter or longer. The point is to have the SU-8 “soft” enough to enable transfer printing to the glass slide.
c. Transfer printing the microcell to the glass slide.
d. Cure the transfer-printed sample longer in the UV light ~20 s

e. Heat for ~ 5 min at 110°C to cure cross-link the epoxy and use acetone to remove any positive-tone photoresist that remains on the microcell from undercutting.
f. Spin-coat SU-8 2002 at 3000 rpm for 30 seconds to form a film ~ 2 µm thick film (this is the planarization layer).
g. Soft bake at 95°C for 1 min to drive off volatile organic solvents.
h. Upside-down exposure of the sample to 90 mJ/cm^2 at 365nm.
i. Post-exposure bake for 2 min at 95°C.
j. Develop in SU-8 developer until fully developed.
k. Remove any residual SU-8 resist on the surface of the cell with oxygen plasma.
l. Spin-coat SU-8 2000.5 at 800 RPM (or less); Ensure that the PR does not de-wet. (If the PR de-wets, treat the sample briefly with oxygen plasma and re-spincoat the sample.)
m. soft bake for 1 min at 95 C
n. spin-coast AZ 2070 photoresist at 3000 rpm for ~30s
o. soft bake: ~1 min @ 110C
p. expose 45 mJ (~5 s when @ 9 mW; 365 nm light)
q. PEB ~ 1 min 15 sec @ 110C
r. Develop in 917 developer
s. Deposit Cr/Cu/Au (10 nm/0.5 µm – 1 µm/10 nm); the Cu thickness can be varied to deposit thicker layers of metal to minimize resistive losses.

3.4 Results and Discussion

3.4.1 Microcell Performance under One Sun and Concentrated Light

Figure 3.7 is an image of a fabricated InGaP solar microcell and the I-V characteristics under one sun. The microcell has Ti/Au contacts for both n- and p-contacts that are ~ 120 nm thick. The conversion efficiency for this cell under one sun was ~ 9.28% under standard test conditions with a FF of ~ 84%. Upon exposure to concentrated sunlight, however, the FF drops substantially suggesting a large amount of series resistance is present inside of the microcell. In order for this cell to work effectively under higher illumination conditions, an optimized contact scheme is required. COMSOL modeling was used to determine the places for high series resistance inside of the microcell.

3.4.2 COMSOL Modeling for an Improved Contact Design

In order to assess the performance of III-V cells under concentrated sunlight, COMSOL Multiphysics® software was used in order to assess possible places for series resistance inside of a solar cell. Figure 3.8 shows the different places series resistance can occur inside of a solar cell [39]. From sheet resistance values and other key parameters, COMSOL can calculate the energy lost due to resistive heating. From this, it is possible to back-calculate the actual resistance for certain layers of the solar cell. Two of the main places that series resistance may occur are from the p- and n-contacts on the cell. Because the doping profiles are known for each layer in the two epi-stacks, it is possible to calculate the various sheet resistances.

To understand the series resistance associated with these layers, modeling of the p-type contact layer as well as the n-type emitter and window layers was performed. This modeling will dictate the geometrical construction of the contacts with the goal of minimizing series resistance losses in order to maintain proper power output. With the resistances calculated for the various layers, Equation 3.1 can be applied to see the effect of resistance on the photocurrent.

$$I = I_L - I_0 \, exp\left\{\frac{q(V+IR_S)}{ak_bT}\right\} - \frac{V+IR_S}{R_{SH}} \qquad (3.1)$$

From the modeling, the best result for the contacting scheme is shown in Figure 3.9. Seven grid fingers are employed although 5 fingers for the top contact are most likely adequate for this case. The bottom contact contains the most resistance – about an order of magnitude more than the top contact. For the case of the InGaP epistack, the top contacts generally have only a few ohms of resistance while the bottom p++ contact contains approximately 15 to 25 ohms, as calculated through COMSOL. For the GaAs epistack the window/emitter layer resistance was on the order of a few ohms but the p++ contact layer was on the order of 10 ohms. For both of these epi-layers, the alternate bottom contact has a series resistance that is ~ 15% lower than the u-shaped contact. Either contact is suitable for these cells. The main constraint on the contact geometry is which spectrum splitting method will be employed. For example, if the light is to be split vertically, then minimizing the area of the lower p-contact is necessary. If, however, the light is to be split horizontally, then a contact on the backsurface of the cell – as is the case for the GaAs device – can be implemented. (It should be noted that having the entire contact on the backsurface of the device gives a series resistance lower than the top contacting scheme.) Given these resistance values, they are still quite low given our cell dimensions. The results that follow in the next sections show cell performance under concentrated sunlight.

3.4.3 Transmission-Line Measurements

Forming ohmic contacts on the p- and n-type portions of the device is necessary to minimize resistive losses and ensure overall device integrity. There has been much discussion as to the choice of metals used for contacting to n- and p-type GaAs [30]. Here Ti/Au or Cr/Au was used for the n-type contact and Au for the p-type contact. Ti and Cr have lower work functions than Au, so they are more suitable metals for contacting to n-type GaAs. Au has a high work function so it is suitable for contacting to p-type GaAs. Au has excellent adhesion to GaAs and other semiconductor materials so long as an oxide layer is removed before metal deposition. From transmission line measurements, typical contact resistances are ~ 8 x 10^{-5} ohm-cm^2 for Ti/Au on n-GaAs and 1 x 10^{-3} – 7 x 10^{-4} ohm-cm^2 for Au on p-GaAs. These contact resistances are quite low and suitable for the needs for concentration in the hundreds of sun range.

3.4.4 Cells under Concentrated Light

Figure 3.10 details the performance of GaAs and InGaP cells under concentrated sunlight. The data was acquired from the solar simulator setup outlined in Chapter 1. A lens was placed above the cell and its distance from the cell was modified to vary the concentration ratio. It was possible to achieve concentration ratios of ~200 sun. For these experiments the cells were probed directly with tungsten probe tips as opposed to using large-area contacts. The concentration ratio was first determined by measuring the cell under one sun and recording its photocurrent and then placing the cell under a lens and re-recording its respective photocurrent. Because the photocurrent of a solar cell is linearly proportional to the illumination intensity (see Equation 1.2), this technique is an excellent gauge at measuring cells under concentrated sunlight [17]. In Figure 3.9a, the InGaP cell with a U-shape contact has an efficiency ~10.6 % at 2 suns with a FF of 86%. The FF of the cell gradually fell when brining the concentration up to nearly 200 suns – 192 suns – with the FF falling to 79%. The efficiency at this level of concentration was estimated to be 10.2%. Better results were obtained for the InGaP cell having the square-shaped p-contact. Under two suns, the efficiency was 10.4% with a FF of 85%. At 225 suns of concentration the FF was 81% with a conversion efficiency of 10.4%. For the case of the GaAs cell, at two suns the cell has an efficiency of 13.8% with a FF of 82%. Taking the cell all the way up to 235.3 suns, the FF fell to 74% with a conversion efficiency of 13.2%.

3.4.5 Cell Performance Values and Room for Further Improvements

First and foremost, for these measurements, the efficiency for each cell is taken to be the area of the p-n junction. The lower, p-contact region is not considered in this area estimation. The size of the top contact is, however, included in the efficiency calculation. This method for determining conversion efficiency is an accurate method since it accounts for the entire p-n junction area – including the shading from the top contact – and the light will not necessarily be falling on the lower contact. The lower contact is an inactive area that does not generate a photocurrent. Concentrating systems can be designed where the light falls mostly on the top cell with minimal light leakage onto the lower contact. The reason for the lower performance for some of the cells under concentrated light comes from the fact that the FF under concentrated light is lower. In order to have better-performing samples under concentration, the FF must remain as close to the original value under one sun as possible. Therefore, as mentioned in the COMSOL modeling section, series resistance must be kept to a minimum. Several places for series resistance occur in these devices. For starters, there is inherent series resistance present in each of the epi-layers. The epi-layers for both InGaP and GaAs cells, however, are at doping concentrations and layer thicknesses such that series resistance should not be a significant factor.

These cells, in fact, should be able to work at over 1000 suns or more given an appropriate contacting scheme. Another potential source for series resistance comes from the semiconductor-metal interface as a result of having non-ohmic contacts. This problem can be remedied with the materials used to form contacts. The epilayers for both of these contacts are at a high enough dopant density such that each should be able to form an ohmic contact – Ti/Au for the n-contact and Au for the p-contact. The contact resistance for both of these schemes is quite low; as verified by transmission-line measurements. The series resistance from these sources is low enough such that these contacts are not a contributing factor to the series resistance. Another possibility for series resistance comes from the technique used to measure these devices: these cells were measured directly with tungsten tips on a soft surface. The cells are above a ~ 2.5 μm layer of SU-8. If these samples are probed with the tips too forcefully, they will break. It has been observed that probing on soft surface increase the series resistance [40]. As such, this is the most likely cause for the drop in FF with increase concentration. Preliminary data has been acquired with a GaAs cell having large-area contacts. At 100 suns, the FF was able to be 81% and the concentration factor was increased to 334 suns with the FF falling to 75%. Improving upon these results will require thicker metal for the cell’s contacts as well as potentially thicker metal layers for the large-area cell encapsulation. Encapsulating the cell in a polymer produces non-uniform side and sloped sidewalls around a cell. Therefore, sputter-coating or electrodepositing large-area contacts are two potential techniques that could generate a uniformly thick enough layer of metal across the surface in order to minimize resistive losses. Another area for improvement comes from how these devices are probed. They are measured using two probes rather than four. A four probe measurement is necessary for accurate measurements as it takes into account the series resistance from the probes wires. All of the measured FFs from our measurements, therefore, are probably a percentage point or two higher than recorded.

Cell efficiencies can be improved upon by employing anti-reflective coatings and surface passivation schemes. A good anti-reflective coating should boost the performance for each device by 30% and passivating the sidewalls will add further improvement. Depositing thicker contacts should allow for performance under greater concentrated sunlight. The overall goal, however, for these cells employ ~ 200 suns, so the current scheme is sufficient for academic investigations. Improving the FF for these devices under concentration will also improve efficiency. For example, the InGaP cell with the square-shaped p-contact currently has an efficiency of 10.4% under 225 sun with a fill factor of 81%. If the fill factor can be maintained at 85%, the efficiency would improve to just over 11 %. For the GaAs cell at 235.3 suns, the efficiency is 13.2 % with a fill factor of 74%. Improving the fill factor to around 83% – the value under one sun – the efficiency improves to 14.8 %. These are conservative estimates for cell performance with improvements in fill factor. Taking into account the slight improvements in open-circuit voltage will add further improvements to efficiency, but these will be smaller improvements than what can be gained by keeping the fill factor constant.

One additional avenue for improving cell performance is changing the window layers of each cell to allow for a greater photocurrent. As discussed in sections 3.3.1 and 3.3.2, the InGaP cell has a 40 nm thick AlInGaP window layer and the GaAs cell has a 25 nm thick InGaP window layer. Switching both of these window layers to a 20 to 25 nm window layer of AlInP would produce the optimal photocurrent as the band gaps for AlInGaP, InGaP, and AlInP are 2.05 eV, 1.9 eV, and 2.3 eV, respectively. A four percent increase in the photocurrent for an

InGaP cell was observed when thinning the AlInGaP window layer with an extremely dilute solution of HCl (1:5 of $HCl:H_2O$ by volume).

Another method for improving the overall performance is to also design the cells in such a way as to promote better collection of light generated from radiative emission. A paper from NREL has discussed how to create more radiative emission from an InGaP cell by redesigning the cell’s epitaxial layers as well as using specially tailored backside reflectors to collect more of this radiated light [2]. Similar techniques have been exploited for GaAs-based devices [1, 41].

3.5 Availability of Photovoltaic Materials

Unlike silicon, III-V materials are rare-earth substances. As such, when using these materials for grid-level power generation, a question of availability of each material is of question. Predicting the long term availability of gallium, indium, and even germanium is difficult, but has been addressed by Andersson et. al [42]. Gallium has an earth abundance of around 15 ppm, making gallium almost as abundant as copper [42]. Gallium, however, does not form in any ores at a very high concentration [43]. This is also true for materials like germanium, selenium, as well as indium – making people refer to them as the “scattered metals” [44]. From this study, it appears that germanium might be the material with availability constraints such that production of devices might become more difficult. Working with germanium-free materials is one avenue for large-scale production [45]. Another avenue involves using some sort of lift-off technique which has been demonstrated with mechanical spalling to exfoliate III-V devices off the surface of a germanium wafer. The wafer can be reused multiple times to minimize materials usage [46, 47].

3.6 Conclusions

This chapter has discussed the rationale behind the epitaxial layers for InGaP- and GaAs-based solar microcells. Fabrication strategies and cell performance under one sun and concentrated light have also been examined. From the discussion above, InGaP cells can be fabricated with an efficiency of ~10% and GaAs cells can be fabricated with an efficiency of ~ 13%. There are improvements that can be possible to achieve greater conversions efficiencies, as discussed in great detail above, but for the scope of this project, these efficiencies are adequate. The overall goal – as will be discussed in the next chapter – is to employ these cells in a spectrum splitting set-up that partitions different portions of the solar spectrum above each cell.

3.7 Figures and Tables

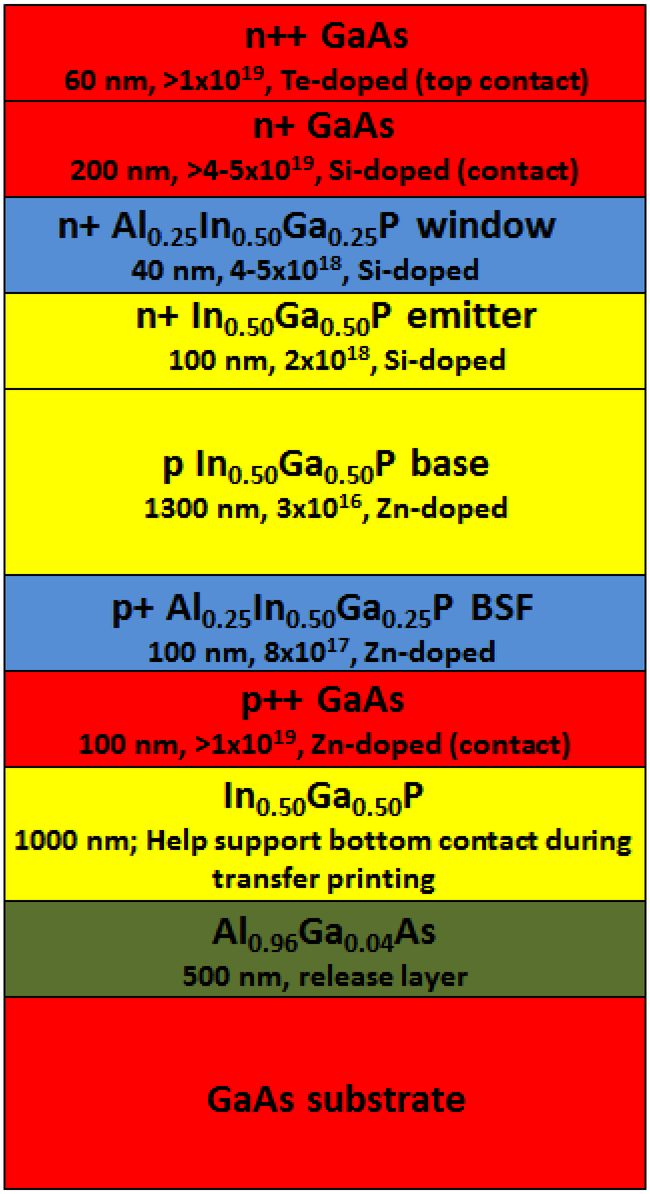

Figure 3.1 InGaP solar cell epi-stack. The layers (from top to bottom) consists of a GaAs cap, an AlInGaP window layer, InGaP emitter and base layers, an AlInGaP backsurface field, a GaAs p-type bottom contact, an InGaP layer below that, a sacrificial AlAs layer, and the GaAs substrate.

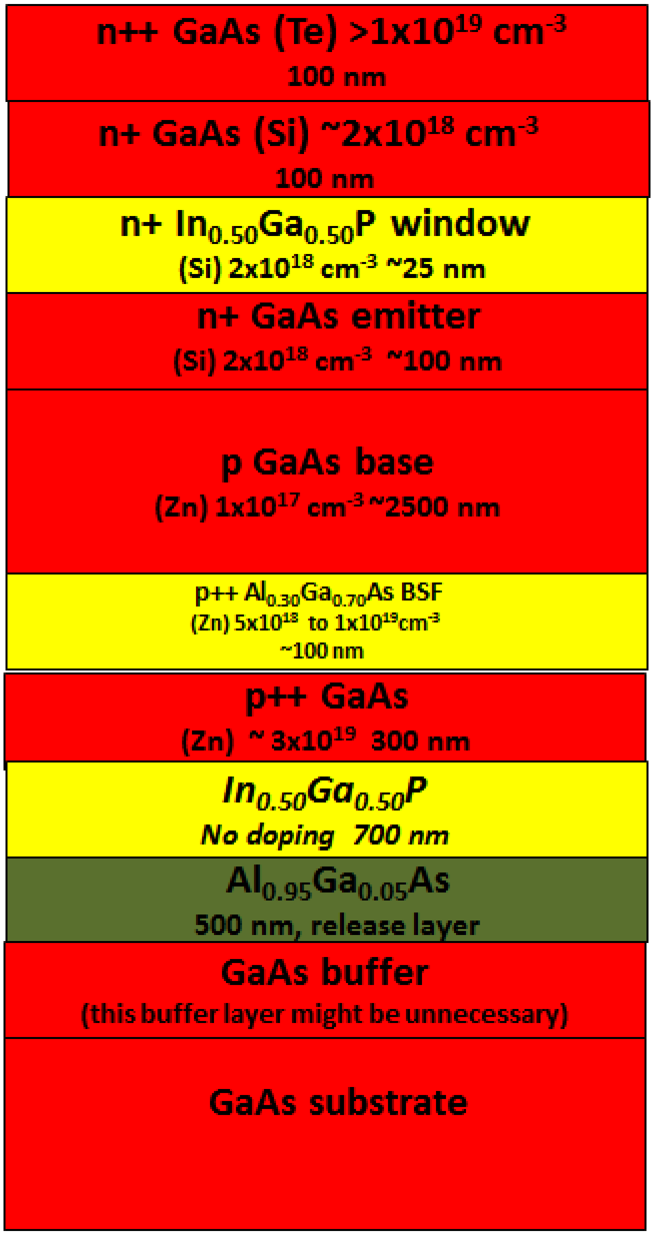

Figure 3.2 GaAs solar cell epi-stack. The layers (from top to bottom) consists of a GaAs cap, an InGaP window layer, GaAs emitter and base layers, an AlGaAs backsurface field, a GaAs p-type bottom contact, an InGaP layer below that, a sacrificial AlAs layer, and the GaAs substrate.

citric acid:H_2O_2	GaAs	$Al_{0.3}Ga_{0.7}As$
1:2	6	2.7
1:1	6.9	2.7
2:1	9.5	2.4
3:1	216.9	2.4
4:1	223.5	2.3
5:1	314	2.7
7:1	288.2	8.9
10:1	251.3	194.5
15:1	155.1	108.2
20:1	76.2	91.8
50:1	39.7	51.2

Table 3.1 Etch rates (in nm/min) for GaAs and AlGaAs in citric acid. Table is adapted from reference [37]. The etch rates are from 20 to 25°C.

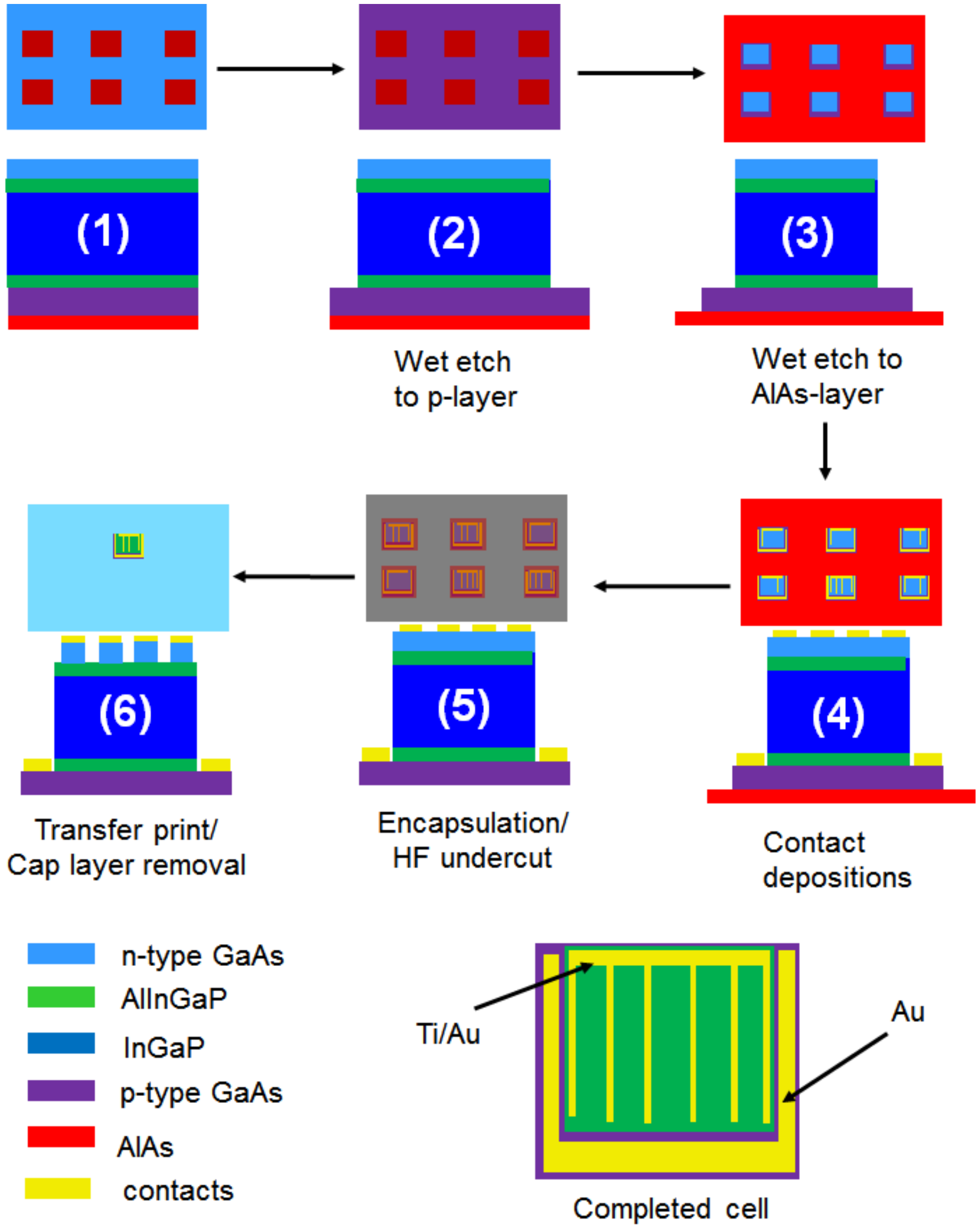

Figure 3.3 InGaP cell fabrication from the epi-wafer. The process begins with (1) patterning the wafer for the cell scheme followed by mesa etching (2 and 3). Afterward, contact deposition is performed with Ti/Au and Au (4) then encapsulation and cell undercutting in HF (5). Cells can then be selectively removed and transferred to a foreign substrate where the cap layer is removed (6).

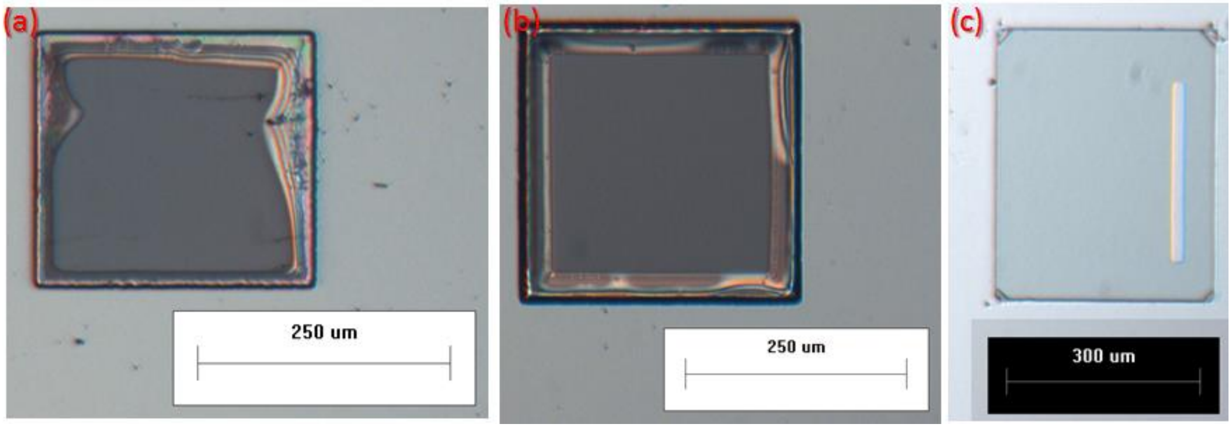

Figure 3.4 (a) and (b) are the over-etching of the AlInGaP window and InGaP emitter/base layers with concentrated HCl. The square-shaped photoresist mask covering each microcell is inadequate for protecting from overetching of AlInGaP and InGaP. AlInGaP and InGaP have a high etch rate in concentrated HCl. To remedy this problem, the GaAs cap layer acts as an etch mask as shown is (c). In (c) the cap layer is removed except for the grey bar at the top. Etching of each corner is present.

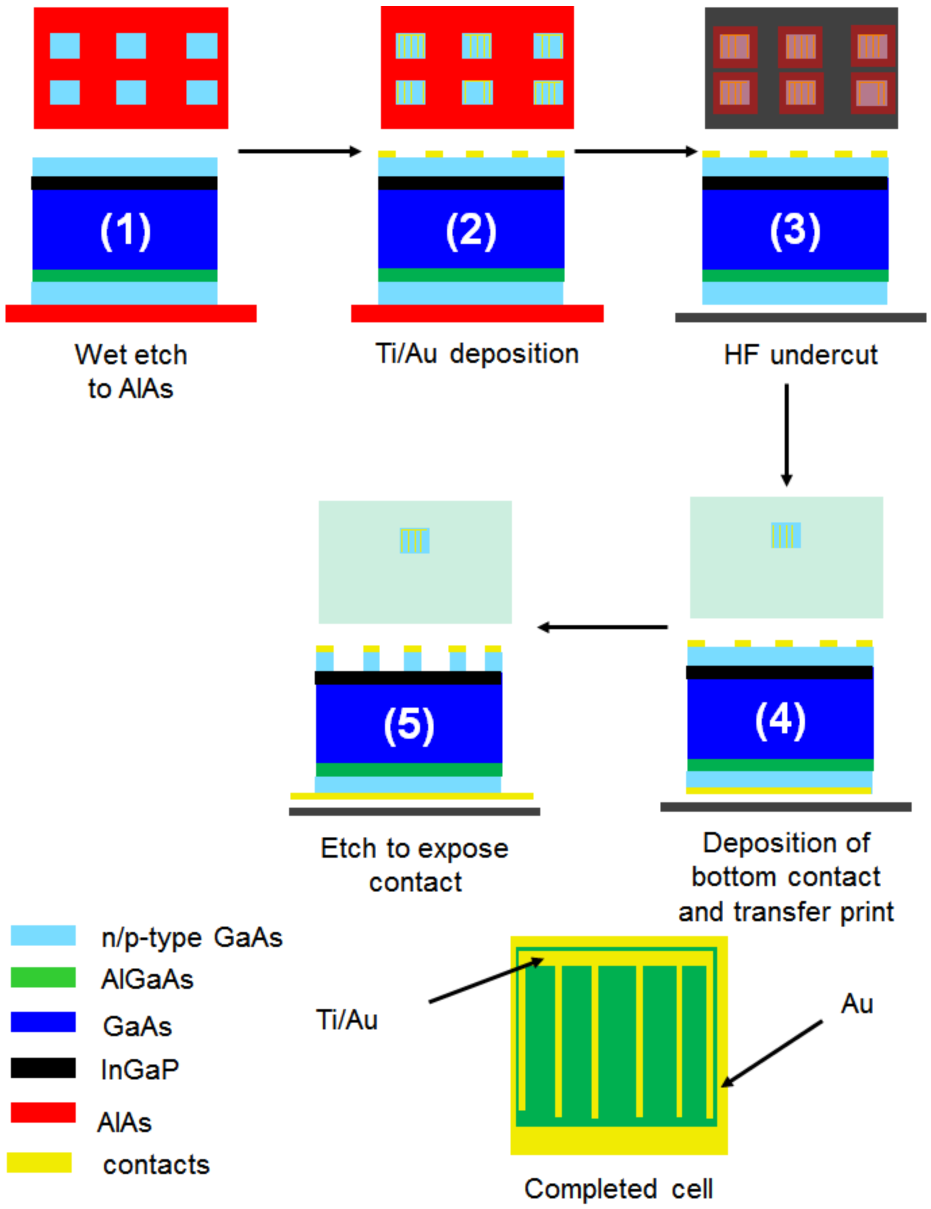

Figure 3.5 GaAs cell fabrication protocol. The process begins with photolithography and mesa etching down to the AlAs layer (1). Afterward, the front contact is deposited Ti/Au (n-contact; 2) and the cells are encapsulated and undercut in HF (3). The cells are then lifted off of the surface and the bottom InGaP layer is etched in HCl and the p-contact (Au) is deposited (4). Cells are then transfer printed and the cap layer is removed and the back contact is exposed (5).

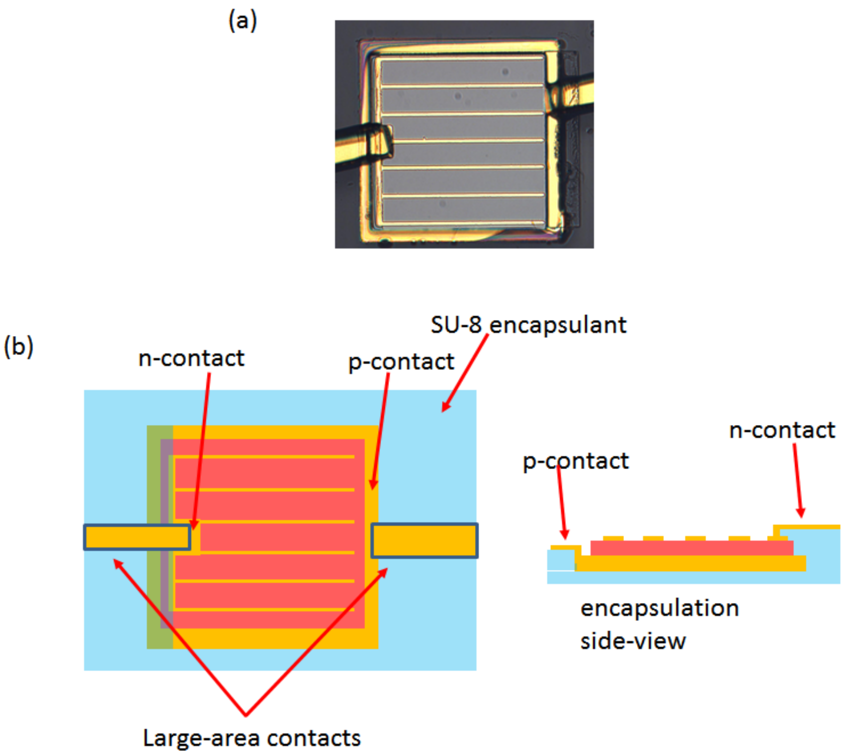

Figure 3.6 Image of an encapsulated GaAs cell (a) along with an illustration showing the encapsulant and the various layers (b). The microcell is approx. 550 x 550 µm^2 in size (active cell) and approx. 650 x 650 µm^2 when including the bottom contact.

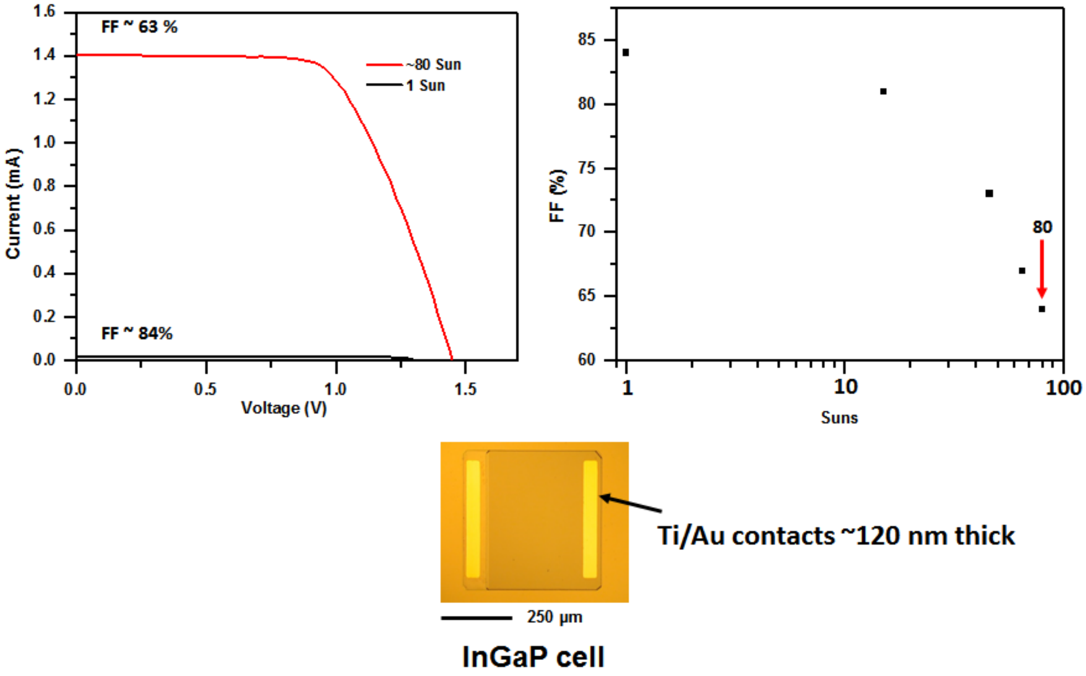

Figure 3.7 InGaP microcell under one sun and 80 sun concentration. The test conditions were standard AM 1.5G. The FF for the cell under on sun is ~84% – a good FF for an InGaP-based device, but under concentrated sunlight (up to ~80 suns) the FF drops. The reason for this decrease in FF is an unoptimized contacting scheme which produces a large amount of series resistance.

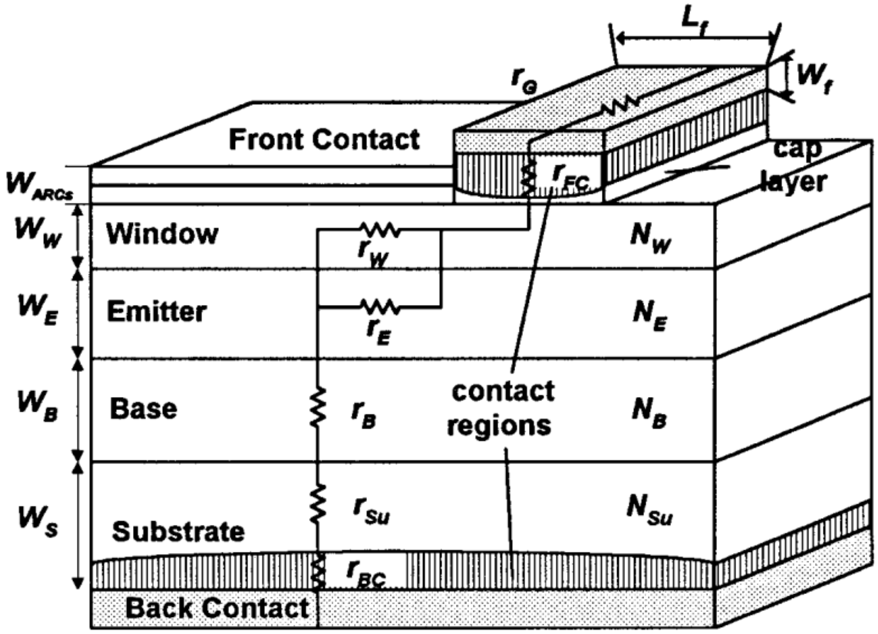

Figure 3.8 Cross-section of a solar cell depicting all of the places for series resistance inside of the device. Figure is adapted from reference [39].

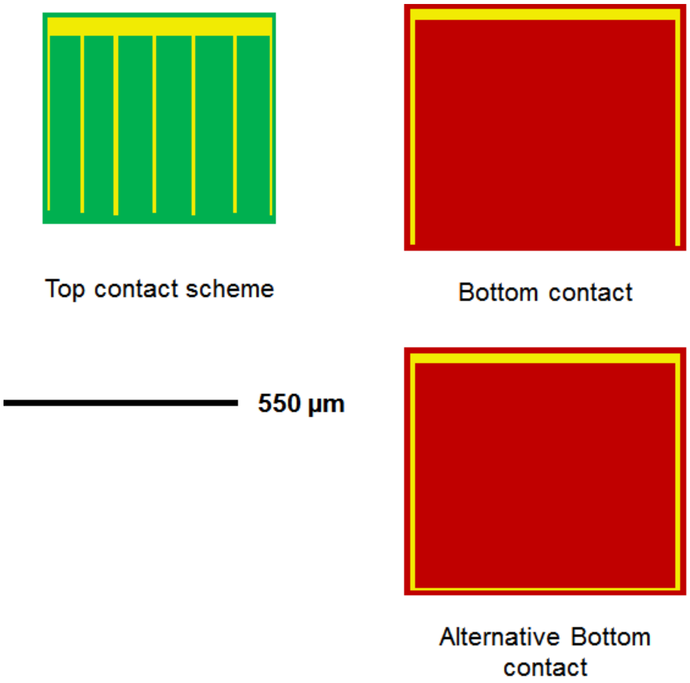

Figure 3.9 Optimized contacting schemes for the n-type (green, left-hand figure) and p-type (red, right-hand figure) layers of the solar cell.

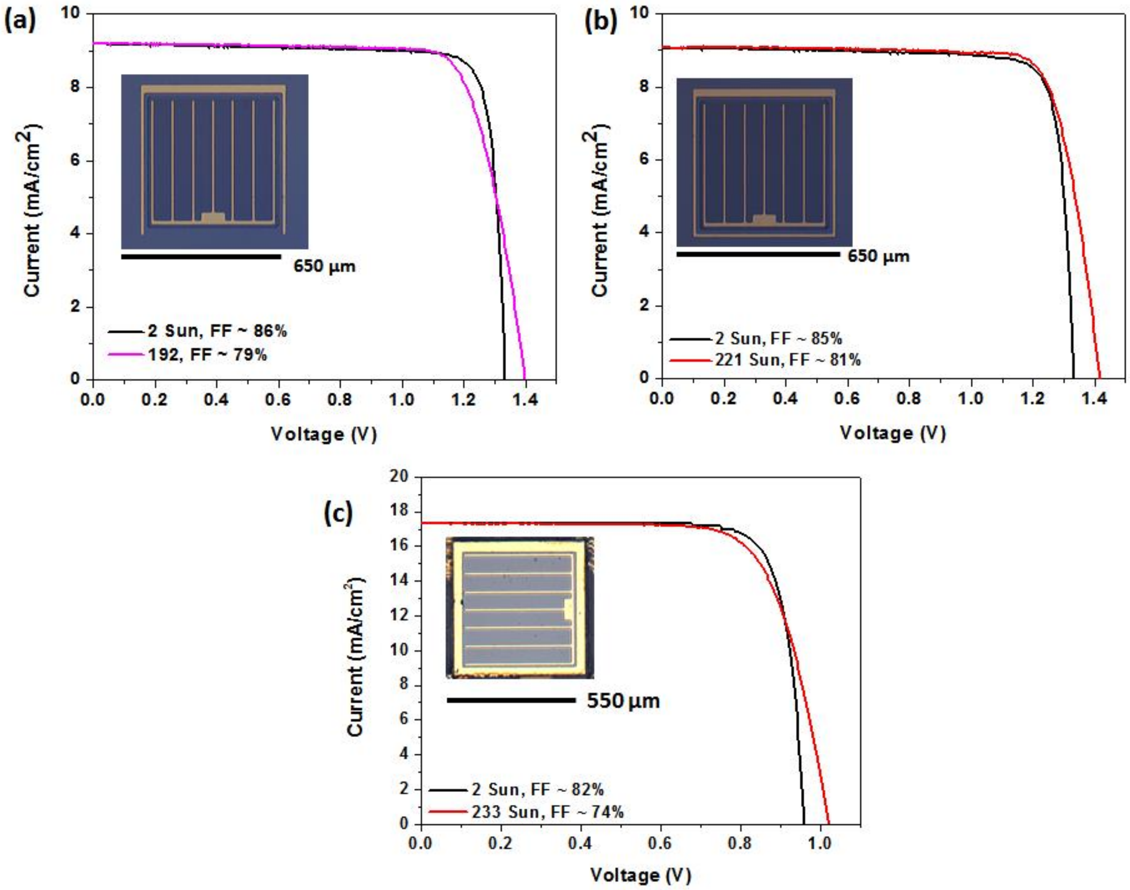

Figure 3.10 InGaP and GaAs cell results under concentrated sunlight. InGaP cells with (a) U-shape and (b) square shape contacts and (c) GaAs cell with a back-side contact. The current densities are plotted along with the amount of concentrated sun light and fill factor (FF) values.

3.8 References

1. Miller, O.D., E. Yablonovitch, and S.R. Kurtz, *Strong Internal and External Luminescence as Solar Cells Approach the Shockley-Queisser Limit.* Ieee Journal of Photovoltaics, 2012. **2**(3): p. 303-311.

2. Geisz, J.F., et al., *Enhanced external radiative efficiency for 20.8% efficient single-junction GaInP solar cells.* Applied Physics Letters, 2013. **103**(4).

3. Green, M.A., et al., *Solar cell efficiency tables (version 43).* Progress in Photovoltaics, 2014. **22**(1): p. 1-9.

4. Luque, A. and V.M. Andreev, eds. *Concentrator Photovoltaics*. Spriner Series in optical sciences. 2007, Springer.

5. Burroughs, S., et al., *A New Approach For A Low Cost CPV Module Design Utilizing Micro-Transfer Printing Technology.* AIP Conference Proceedings, 2010. **1277**(1): p. 163-166.

6. Furman, B., et al. *A high concentration photovoltaic module utilizing micro-transfer printing and surface mount technology*. in *Photovoltaic Specialists Conference (PVSC), 2010 35th IEEE*. 2010.

7. Yoon, J., et al., *GaAs photovoltaics and optoelectronics using releasable multilayer epitaxial assemblies.* Nature, 2010. **465**(7296): p. 329-U80.

8. Konagai, M., M. Sugimoto, and K. Takahashi, *HIGH-EFFICIENCY GAAS THIN-FILM SOLAR-CELLS BY PEELED FILM TECHNOLOGY.* Journal of Crystal Growth, 1978. **45**(1): p. 277-280.

9. vanGeelen, A., et al., *Epitaxial lift-off GaAs solar cell from a reusable GaAs substrate.* Materials Science and Engineering B-Solid State Materials for Advanced Technology, 1997. **45**(1-3): p. 162-171.

10. Schermer, J.J., et al., *Thin-film GaAs epitaxial life-off solar cells for space applications.* Progress in Photovoltaics, 2005. **13**(7): p. 587-596.

11. van Deelen, J., et al., *On the development of high-efficiency thin-film GaAs and GaInp(2) cells.* Journal of Crystal Growth, 2007. **298**: p. 772-776.

12. Schermer, J.J., et al., *High rate epitaxial lift-off of InGaP films from GaAs substrates.* Applied Physics Letters, 2000. **76**(15): p. 2131-2133.

13. Tatavarti, R., et al., *InGaP/GaAs / InGaAs INVERTED METAMORPHIC (IMM) SOLAR CELLS ON 4 " EPITAXIAL LIFTED OFF (ELO) WAFERS.* 35th Ieee Photovoltaic Specialists Conference, 2010: p. 2125-2128.

14. Yazawa, Y., et al., *GaInP single junction and GaInP/GaAs two junction thin-film solar cell structures by epitaxial lift-off.* Solar Energy Materials and Solar Cells, 1998. **50**(1–4): p. 229-235.

15. Kim, R.H., et al., *Flexible Vertical Light Emitting Diodes.* Small, 2012. **8**(20): p. 3123-3128.

16. Kim, R.H., *Printed Microscale Inorganic Light Emitting Diodes on Flexible Substrates for Display, Biomedical, and Robotic Applications*, in *Materials Science and Engineering*. 2012, University of Illinois at Urbana-Champaign: Urbana, IL. p. 164.

17. Luque, A. and S. Hegedus, eds. *Handbook of Photovoltaic Science and Engineering -- 2nd Ed.* 2011, John Wiley & Sons: West Sussex.

18. Bertness, K.A., et al., *29.5-PERCENT-EFFICIENT GALNP/GAAS TANDEM SOLAR-CELLS.* Applied Physics Letters, 1994. **65**(8): p. 989-991.

19. Karam, N.H., et al., *Recent developments in high-efficiency Ga0.5In0.5P/GaAs/Ge dual- and triple-junction solar cells: steps to next-generation PV cells.* Solar Energy Materials and Solar Cells, 2001. **66**(1-4): p. 453-466.

20. Garcia, I., et al., *A 32.6% efficient lattice-matched dual-junction solar cell working at 1000 suns.* Applied Physics Letters, 2009. **94**(5).

21. Su, L.C., I.H. Ho, and G.B. Stringfellow, *KINETICALLY CONTROLLED ORDER-DISORDER STRUCTURE IN GALNP.* Applied Physics Letters, 1994. **65**(6): p. 749-751.

22. Delong, M.C., et al., *BAND-GAP OF COMPLETELY DISORDERED GA0.52IN0.48P.* Applied Physics Letters, 1995. **66**(23): p. 3185-3187.

23. Kim, C.C., J.W. Garland, and P.M. Raccah, *MODELING THE OPTICAL DIELECTRIC FUNCTION OF THE ALLOY SYSTEM ALXGA1-XAS.* Physical Review B, 1993. **47**(4): p. 1876-1888.

24. Gomyo, A., et al., *NONEXISTENCE OF LONG-RANGE ORDER IN GA0.5IN0.5P EPITAXIAL LAYERS GROWN ON (111)B AND (110) GAAS SUBSTRATES.* Japanese Journal of Applied Physics Part 2-Letters, 1988. **27**(12): p. L2370-L2372.

25. Clawson, A.R., *Guide to references on III-V semiconductor chemical etching.* Materials Science & Engineering R-Reports, 2001. **31**(1-6): p. 1-438.

26. Olson, J.M., et al., *ULTRALOW RECOMBINATION VELOCITY AT GA0.5IN0.5P/GAAS HETEROINTERFACES.* Applied Physics Letters, 1989. **55**(12): p. 1208-1210.

27. Hjort, K., *Sacrificial etching of III-V compounds for micromechanical devices.* Journal of Micromechanics and Microengineering, 1996. **6**(4): p. 370-375.

28. Pearton, S.J., *Critical issues of III-V compound semiconductor processing.* Materials Science and Engineering B-Solid State Materials for Advanced Technology, 1997. **44**(1-3): p. 1-7.

29. Pearton, S.J., *Chapter 1 Introduction*, in *Semiconductors and Semimetals*, R. Willardson and H.S. Nalwa, Editors. 2001, Elsevier. p. 1-13.

30. Baca, A.G. and C.I.H. Ashby, *Fabrication of GaAs Devices*. 2005, London, United Kingdom: Institution of Engineering and Technology.

31. *Piranha Solutions*. 2011 [cited 2014 2-18]; Available from: http://web.princeton.edu/sites/ehs/labsafetymanual/cheminfo/piranha.htm.

32. Shaw, D.W., *LOCALIZED GAAS ETCHING WITH ACIDIC HYDROGEN-PEROXIDE SOLUTIONS.* Journal of the Electrochemical Society, 1981. **128**(4): p. 874-880.

33. Lee, H.J., et al., *Selective wet etching of a GaAs/AlxGa1-xAs heterostructure with citric acid-hydrogen peroxide solutions for pseudomorphic GaAs/AlxGa1-xAs/InyGa1-y heterojunction field effect transistor fabrication.* Materials Science and Engineering B-Solid State Materials for Advanced Technology, 1995. **35**(1-3): p. 230-233.

34. MicroChemicals. *Etching with Hydrofluoric Acid*. 2013; Available from: http://www.microchemicals.eu/technical_information/hf_etching.pdf.

35. Cheng, C.W., et al., *Epitaxial lift-off process for gallium arsenide substrate reuse and flexible electronics.* Nature Communications, 2013. **4**.

36. Lothian, J.R., et al., *PLASMA AND WET CHEMICAL ETCHING OF IN0.5GA0.5P.* Journal of Electronic Materials, 1992. **21**(4): p. 441-445.

37. Wanlass, M.W., et al., *Lattice-mismatched approaches for high-performance, III-V photovoltaic energy converters*, in *Conference Record of the Thirty-First IEEE Photovoltaic Specialists Conference - 2005*. 2005, Ieee: New York. p. 530-535.

38. Cich, M.J., et al., *Crystallographic dependence of the lateral undercut wet etching rate of InGaP in HCl.* Applied Physics Letters, 2003. **82**(4): p. 651-653.

39. Algora, C. and V. Diaz, *Influence of series resistance on guidelines for manufacture of concentrator p-on-n GaAs solar cells.* Progress in Photovoltaics, 2000. **8**(2): p. 211-225.

40. Zhao, L., *High Efficiency Mechanically Stacked Multi-junction Solar Cells for Concentrator Photovoltaics*. 2010, KATHOLIEKE UNIVERSITEIT LEUVEN: Heverlee, Belgium. p. 200.

41. Steiner, M.A., et al., *Optical enhancement of the open-circuit voltage in high quality GaAs solar cells.* Journal of Applied Physics, 2013. **113**(12).

42. Andersson, B.A., *Materials availability for large-scale thin-film photovoltaics.* Progress in Photovoltaics: Research and Applications, 2000. **8**(1): p. 61-76.

43. Petkof, B., *Gallium in Mineral Facts and Problems*, B.o.M. US Dept. of the Interior, Editor. 1985: Washington, DC.

44. Habashi, F., ed. *The economic classification of metals*. Handbook of Extractive Metallurgy. 1997, Wiley-VCH: Weinheim. 1-13.

45. Chiu, P., et al., *InGaP/GaAs/InGaAs Triple Junction Concentrators Using Bi-Facial Epigrowth*, in *High and Low Concentrator Systems for Solar Electric Applications V,* L.E. Greene and R.A. Sherif, Editors. 2010, Spie-Int Soc Optical Engineering: Bellingham.

46. Shahrjerdi, D., et al., *High-Efficiency Thin-Film InGaP/(In)GaAs/Ge Multijunction Solar Cells Enabled by Controlled Spalling Technology*. 2012 38th Ieee Photovoltaic Specialists Conference. 2012, New York: Ieee. 974-977.

47. Shahrjerdi, D., et al., *Ultralight High-Efficiency Flexible InGaP/(In)GaAs Tandem Solar Cells on Plastic.* Advanced Energy Materials, 2013. **3**(5): p. 566-571.

Chapter 4

Enhanced Ultraviolet Responses in Thin-film InGaP Solar Microcells by Down-Shifting

Significant portions of the text, as well as the figures, included herein are reproduced with permission from the following paper: X. Sheng, C.J. Corcoran, J. He, L. Shen, S. Kim, J. Park, R.G. Nuzzo and J.A. Rogers, "Enhanced Ultraviolet Responses in Thin-Film InGaP Solar Cells by Down-Shifting," Physical Chemistry Chemical Physics 15, 20434-20437 (2013). DOI: 10.1039/c3cp54096k.

4.1 Abstract

This chapter focuses on layers of poly(methyl methacrylate) doped with the Eu complex Eu(DPEPO)(hfac)(3) (EuDH) to provide a means for down-shifting incident ultraviolet (UV) light into the visible range. It is observed that this Eu complex has beneficial effects on the overall performance of solar cells, as will be demonstrated with thin-film InGaP microcells.

4.2 Introduction

Light management in solar cells represents an effective avenue for improving performance and reducing the overall cost of photovoltaic (PV) systems [1]. To approach efficiencies close to those defined by detailed balance limits [2], a solar cell must have both a great electronic efficiency and a great optical efficiency as well as a good degree of radiative efficiency [3]. Every photon that is incident upon a solar cell, with an energy above the cell's band gap, should be absorbed and each absorption event should yield at least one electron–hole pair capable of extraction as electrical power. Traditional routes for improving cell performance have focused significant efforts towards light trapping and other schemes to enhance the absorption near the solar cell’s band edge, particularly in the long wavelength side of the solar spectrum [4-7]. By contrast, less attention has been paid to the short-wavelength limit. In the ultraviolet (UV) range (300–400 nm), most PV materials naturally have high absorption coefficients, thereby eliminating the need for light trapping. Low quantum efficiencies, however, are usually obtained in this region of the spectrum, even for cells with record efficiencies [8]. Figure 4.1 represents the quantum efficiency of a typical thin-film GaAs solar cell created with the epitaxial lift-off technique from Alta Devices. These devices hold the single junction efficiency record at 28.8% efficiency based on standard test conditions under the AM 1.5G solar spectrum [8]. This is remarkeable for several reason such as the fact that (1) the absorber layer is ~ 1 µm thick and (2) the maximum efficiency under standard test conditions is around 33%. As is apparent from Figure 4.1, there is a low response in the UV region. Such a low response to the UV arises from both intrinsic and more practical considerations. First, in order to decrease series resistance and maximize carrier collection, traditional cell designs incorporate highly doped window and/or emitter layers [9-11], which can act as a deadzone for UV light conversion because of the extremely short diffusion lengths for the minority carriers in these regions. Second, anti-reflective coatings are typically optimized to minimize light reflections around the peak of the solar spectrum (500–700 nm) [12], and can often have high reflection losses in the UV range [13]. Finally, in most modules, solar cells are encapsulated with glass and/or plastic covers [14] that absorb UV light; this problem can be minimized with silicone-based encapsulants as opposed to organic-based encapsulants such as ethylene-vinyl acetate [15]. From the flux of UV photons from 300–400 nm in the standard AM1.5G solar spectrum [12], there is a potential for these UV photons to contribute 1.3 mA cm^{-2} of current to the overall power out-put of the device. Exploiting these UV photons efficiently can therefore improve the efficiency by a meaningful amount. Various down-shifting materials, including organo-lanthanide complexes, organic dyes and quantum dots, have been proposed to convert UV photons into visible ones [16, 17]. Polymer coatings that serve as a solar cell encapsulant have been doped with down-shifting materials to demonstrate increase UV responses and efficiencies for conventional PV cells and modules based on semiconductor materials such Si and CdTe [18-22]. For another approach, by applying the UV down-shifting layers on top of organic solar cells, UV degradation can be mitigated and longer device lifetimes can be achieved [17]. Such concepts, however, also have particular potential in high efficiency III–V (GaAs, InGaP, etc.) solar cells, where detailed balance limits can be approached as a result of high radiation efficiencies [9, 22]. This chapter demonstrates the use of a specific europium complex, Eu(DPEPO)(hfac)3 [DPEPO = bis(2-(diphenyl-phosphino)phenyl)ether oxide, hfac = hexafluoroacetylacetonate], doped into thin films of poly(methyl methacrylate) (PMMA), as a means for down-shifting UV photons (300–360 nm) into visible photons at 610 nm of light. Experiments with thin-film indium gallium phosphide (InGaP) cells formed by the epitaxial lift-off demonstrate improvements that result from application of such films as front side coatings. The UV gain and loss mechanisms for down-shifting are analyzed in detail by numerical simulations.

4.3 Materials and Methods

4.3.1 InGaP Cell Design and Fabrication

Figure 4.2a presents an optical micrograph of a thin-film InGaP solar cell (500 µm x 500 µm) integrated onto a glass substrate using techniques of epitaxial lift-off and transfer printing.

The cell design and fabrication protocol followed procedures discussed in chapter 3. The materials for the cells are formed by growth on a gallium arsenide (GaAs) substrate via metal–organic chemical vapor deposition (MOCVD). The detailed structure (from bottom to top) includes the GaAs substrate, a 500 nm $Al_{0.96}Ga_{0.04}As$ sacrificial layer, a 1000 nm In0.5Ga0.5P supporting layer, a 100 nm p-GaAs bottom contact ($p > 1 \times 10^{19}$ cm^{-3}), a 100 nm p-$Al_{0.25}In_{0.5}Ga_{0.25}P$ backsurface field (BSF) layer ($p = 8 \times 10^{17}$ cm^{-3}), a 1300 nm p-$In_{0.5}Ga_{0.5}P$ base ($p = 3 \times 10^{16}$ cm^{-3}), a 100 nm n-$In_{0.5}Ga_{0.5}P$ emitter ($n = 2 \times 10^{18}$ cm^{-3}), a 40 nm n-$Al_{0.25}In_{0.5}Ga_{0.25}P$ window layer ($n = 5 \times 10^{18}$ cm^{-3}) and a 200 nm n-GaAs contact ($n > 5 \times 10^{18}$ cm^{-3}). Zn and Si serve as p-type and n-type dopants, respectively. Bilayers of Cr/Au (10 nm/100 nm) form the contacts. The cells are lithographically fabricated, using H_3PO_4 (85 wt% in water)–H_2O_2 (30 wt% in water)–H2O (1:13:12) and HCl (36 wt% in water) to etch the GaAs and InGaP/AlInGaP layers, respectively. These etching solutions were etch-selective for their respective layers. After removing the $Al_{0.96}Ga_{0.04}As$ sacrificial layer in an ethanol-rich hydrofluoric acid (HF) solution (ethanol :HF = 1.5:1 by volume), individual InGaP cells can be released from the GaAs wafer and then bonded onto glass substrates by transfer printing with a flat poly(dimethylsiloxane) (PDMS) stamp [23]. The ethanol in the HF solution served to reduce bubble formation so that greater HF concentrations could be used to enhance the AlAs etch rate. Devices were typically undercut within 45 min and were allowed to overetch for an additional 10 min.

4.3.2 InGaP Cell Encapsulation in SU-8

In order to encapsulate the cells with the downconversion material, the material must be spin-coated over the surface of the cell. This process covers the contacts, and therefore, large-area interconnects are required. The protocol for the large-area contacts is the same as listed in chapter 3. Briefly, a 2 mm layer of photocurable epoxy (SU-8 2002, MicroChem) acts as an adhesive to facilitate transfer printing to the glass substrate. The sidewalls of the cell are encapsulated with a 500 nm thick layer of a photocurable epoxy (SU-8 2000.5, MicroChem). Large-area metal contacts of Cr/Cu/Au (10 nm/500 nm/10 nm) are used for electrical interconnection. This device with the large-area contacts serves for testing cells before and after deposition of the luminophore. SU-8 is a neagative tone photoresist that is extremely versatile and is capable of forming tapered sidewalls [24]. Figure 4.3a is a representation of the entire encapsulated device. The sidewalls of the final encapsulated device were sloped as to allow for deposited contacts to have very low series resistance. Sputtering contacts in this manner is the technique for minimizing resistance issues as sidewall definition has a huge impact on the uniformity of the deposition [25].

4.3.3 Encapsulation of the Cell with the Luminophore

The Eu(DPEPO)(hfac)3 (EuDH) complex serves as the UV luminophore [26]. Figure 4.3b is the chemical structure of the EuDH complex. Powders of EuDH are mixed into a solution of PMMA (950000 MW in anisole, 11 wt%, by MicroChem), at a concentration of 1 wt% EuDH. PMMA is a desirable choice for the polymer matrix because it is transparent at wavelengths longer than 300 nm and is commonly used for solar module encapsulation [27]. The resulting solution can be spin cast and cured at 150°C, to remove anisole and form EuDH-doped PMMA solid films on substrates of interest. Figure 4.4 shows the absorption and emission properties of a 40 µm thick PMMA + EuDH film coated on a quartz substrate, and a comparison to a 40 µm thick film without EuDH. Shown in Figure 4.4a, the PMMA absorbs UV at wavelengths below~300 nm, while the EuDH complex absorbs light between 300 nm and 360 nm. The photons absorbed by EuDH are down-shifted, with an emission peak at around 610 nm

(Figure 4.4b), which corresponds to a Stokes shift that is much larger than that in common organic dyes [18, 20, 22]. The EuDH doped in a 40 µm thick PMMA film provides nearly 100% UV absorption from 300 nm to 360 nm, eliminating the need for using thick coatings as reported previously [19, 20, 22]. This thin geometry minimizes parasitic optical losses (absorption/scattering by the polymer, edge emission, etc.). The measured intrinsic photoluminescence quantum yield (PLQY) for the EuDH doped in PMMA is ~77%, which is one of the highest values reported in similar Eu-based complexes [21, 26].

4.4 Results and Discussion

4.4.1 Optical Results

Both PMMA and PMMA + EuDH can be coated directly on InGaP cells, as shown in Figure 4.5. The PMMA (Figure 4.4a) allows light ($\lambda > 300$ nm) to pass directly through, for absorption by the cell. Visible light (400–650 nm) can be absorbed by the active InGaP p-n junction, to generate free carriers. Most of the UV light (300–400 nm), however, is blocked by the 40 nm thick AlInGaP window layer, due to the high absorption coefficient of AlInGaP in the UV range [28]. As a result, low UV responses are observed; similar behaviors are also reported in GaAs and InGaP cells with or close to record efficiencies [8-10], for similar reasons. With PMMA + EuDH (Figure 4.4b), UV light from 300 nm to 360 nm is absorbed by the EuDH and down-shifted, without affecting light at longer wavelengths ($\lambda > 360$ nm). The down-shifted light has an isotropic emission profile; it can directly penetrate into the high-index InGaP cell (process 1), or undergo total internal reflection (TIR) at the PMMA/air interface and then couple into the InGaP cell (process 2). Both mechanisms contribute to carrier generation, thereby improving the UV responses. Various loss mechanisms are also present due to non-unity down-shift efficiency (PLQY = 77%) (process 3), out-coupling into the air due to non-TIR at the PMMA/air interface (process 4), and light escaping at the edges of the device (process 5).

To predict and compare the performance of the two device configurations that are listed in Figure 4.5, numerical simulations are employed to determine the external quantum efficiency (EQE) spectra that are plotted in Figure 4.6a. The EQE can be written

$$\mathrm{EQE}(\lambda) = \mathrm{IQE}(\lambda) \text{ x } [1 - R(\lambda)] \qquad (4.1)$$

where the internal quantum efficiency (IQE) spectra can be calculated through electrical modeling [29] of a 1-D InGaP cell structure shown in Figure 4.2b. The reflection spectra R(λ) can be calculated by combining Fresnel reflections and ray tracing [30]. Optical and electrical properties of different layers are found in the literature [28, 31, 32]. The InGaP cell with a PMMA coating shows a low UV response because of high absorption introduced by the AlInGaP window layer, as discussed in Figure 4.5a. In the visible range, the EQE peaks at around 600 nm and decreases to zero at the band-edge of InGaP (E_g ~1.9 eV). If the PMMA layer is doped with EuDH, most of the UV photons from 300 nm to 360 nm are absorbed by the EuDH and down-shifted into photons with wavelengths of ~610 nm, where the InGaP cell has its maximum IQE. In this case, the EQE can be estimated by

$$\mathrm{EQE}(\lambda = 300\text{–}360 \text{ nm}) =$$

$$\mathrm{IQE}(\lambda = 610 \text{ nm})\text{x}[1 - R_{air/PMMA}] \text{ x PLQY x }]1 - \text{escaped light}] =$$

$$90\% \text{ x } (1\text{–}4\%) \text{ x } 77\% \text{ x } (1\text{–}50\%) = 33\% \qquad (4.2)$$

Despite the various loss mechanisms for the luminescent photons, a significant fraction of photons are collected by the InGaP cell, resulting in an improved response from 300 nm to 360 nm. The EQE at longer wavelengths ($\lambda > 360$ nm) is unaffected due to the transparency of the PMMA + EuDH in this range.

4.4.2 Current-Voltage Results

Figure 4.6b presents the measured EQE spectra of InGaP cells with PMMA and PMMA + EuDH coatings. In agreement with simulation results shown in Figure 4.6a, the cell with PMMA + EuDH exhibits an improved EQE from 280 nm to 360 nm compared to the cell with a PMMA coating. The EQE spectra from 360 nm to 700 nm for both cells are identical. The differences between simulation and experimental results (Fig. 4a and b) likely arise from differences between the optical properties of InGaP and AlInGaP used in simulations and the experimental values and from loss mechanisms associated scattering and other parasitic losses. Figure 4.6c shows the measured current–voltage characteristics of the two cells under the standard AM1.5G spectrum. Improved UV responses associated with EuDH down-shifting increases the current density from 8.40 mA cm to 8.68 mA cm^{-2}, with a relative increase of about 3.5%. For the cells with PMMA and with PMMA + EuDH, the efficiencies are 9.28% and 9.48%, respectively. (In these comparisons, we use pairs of cells that exhibited nearly identical performance, as measured before applying the PMMA coatings.)

4.5 Conclusions

In conclusion, that chapter has shown that PMMA coatings doped with a luminescent material, EuDH, can improve the UV responses of thin-film InGaP cells by light down-shifting. As PMMA is a commonly used encapsulation material, this luminescent layer can be readily adopted for current commercial solar modules without altering the active cell structure design. Further performance improvements can be achieved by addressing the various loss mechanisms mentioned in Figure 4.5b. For example, development of luminophores with increased luminescence efficiency (PLQY > 80%) and expanded absorption range (e.g. from 300 nm to 450 nm) with little cross-coupling and a similar Stokes shift could be valuable. In addition, conversion of UV photons into multiple visible or infrared photons via multi-exciton generation offers potential for quantum efficiencies larger than 100% [33, 34]. From the standpoint of optical design, light that escapes from the edges of the device can be collected using luminescent concentrators [30]. To reduce the coupling loss, photonic/plasmonic structures and dyes/quantum dots with controlled anisotropic emission can be considered. Similar designs can be employed directly with world-record Si and GaAs cells 7, although the relative increases in efficiency will be less than those observed with InGaP cells, due to higher overall photocurrents in these systems. Nevertheless, the approaches described here are notable for their ability to be used, in a simple additive fashion, with advanced cell designs and other optical management techniques.

4.6 Acknowledgements

This work is supported by the DOE 'Light-Material Interactions in Energy Conversion' Energy Frontier Research Center under grant DE-SC0001293. L. Shen acknowledges support from China Scholarship Council. S. Kim and J. Park are supported by the National Research Foundation of Korea (NRF) grant funded by the Korea government (MEST) (No. 2012001846). We thank Prof. N. C. Giebink for PLQY measurements.

4.7 Figures

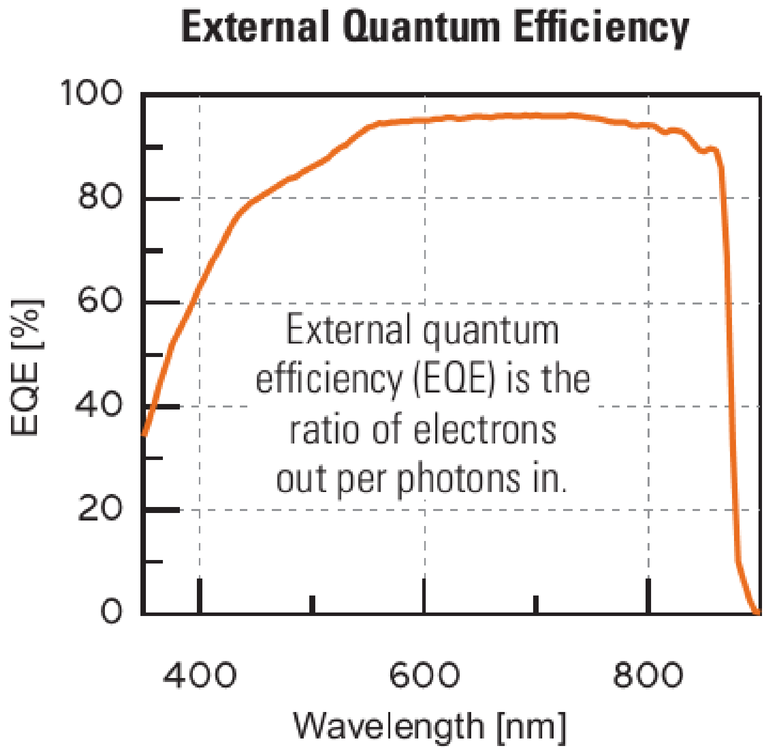

Figure 4.1 External Quantum Efficiency of a typical single junction GaAs solar cell from Alta Devices cell. The figure is taken from reference [35]. The low performance of this cell in the UV is a result of the deadzone in the emitter/window layers as well as the anti-reflective coating not being optimized for UV photons.

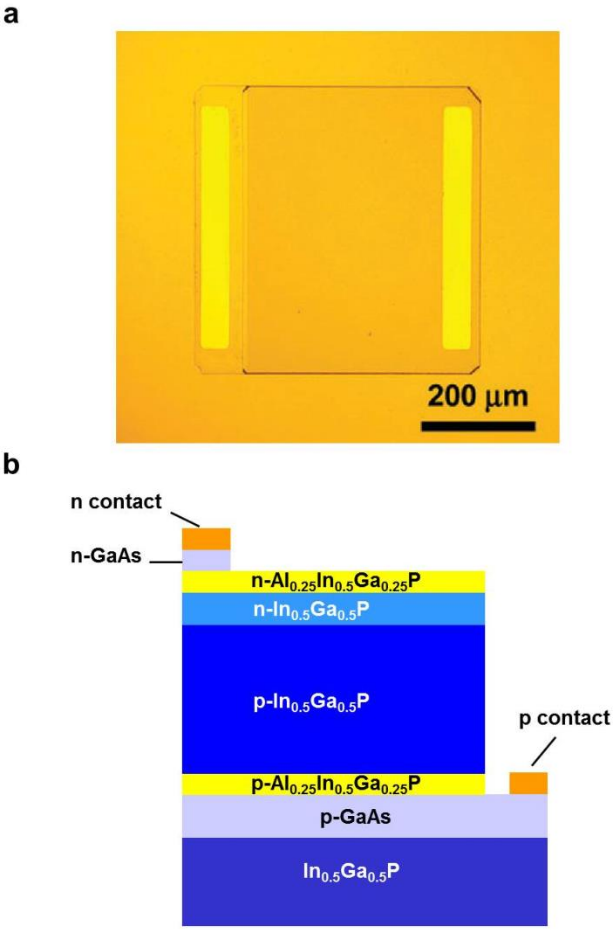

Figure 4.2 (a) Optical microscope image of a thin-film InGaP cell (500 μm × 500 μm) with Ohmic contacts, printed on a glass substrate. (b) Cross sectional schematic illustration of the cell, showing the InGaP homojunction, AlInGaP window layers and contacting layers.

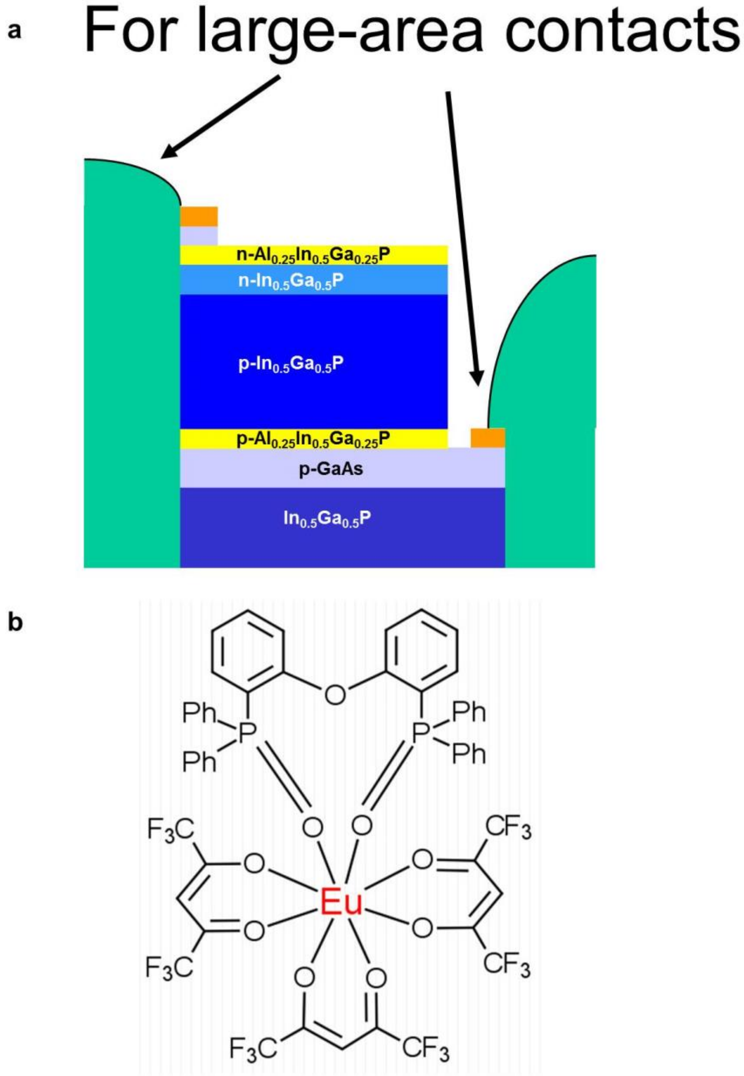

Figure 4.3 (a) Encapsulated InGaP cell with layers of SU-8 green that allow for the deposition of large-area contacts and (b) the EuDH complex that is used to coat the cell.

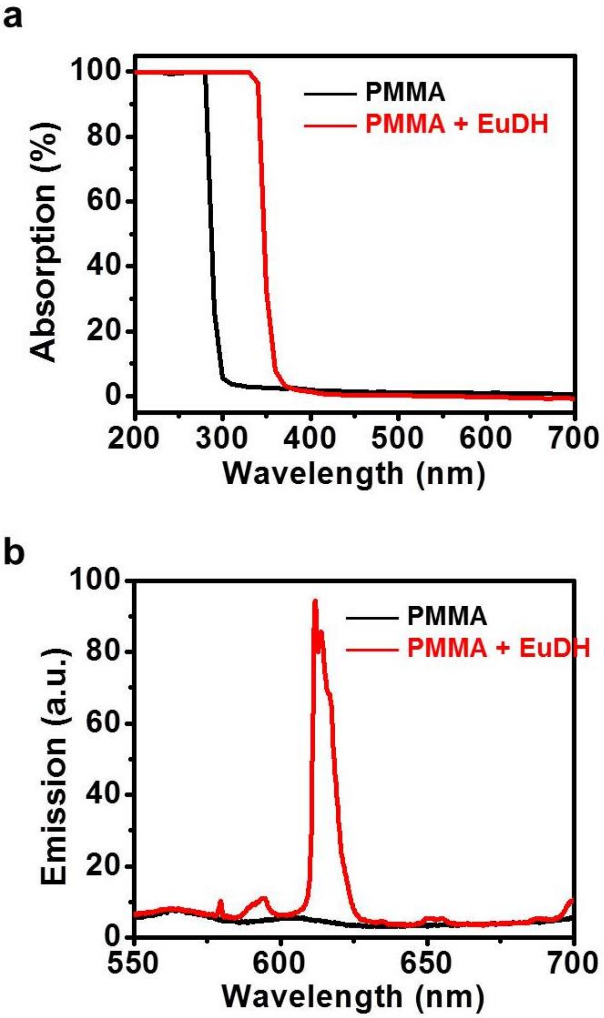

Figure 4.4 Measured optical properties of a layer of PMMA layer (in black) and a layer of PMMA + EuDH (in red) on quartz substrates. The thicknesses in both cases are 40 μm. (a) Absorption spectra. (b) Emission spectra, measured with an excitation source at 365 nm.

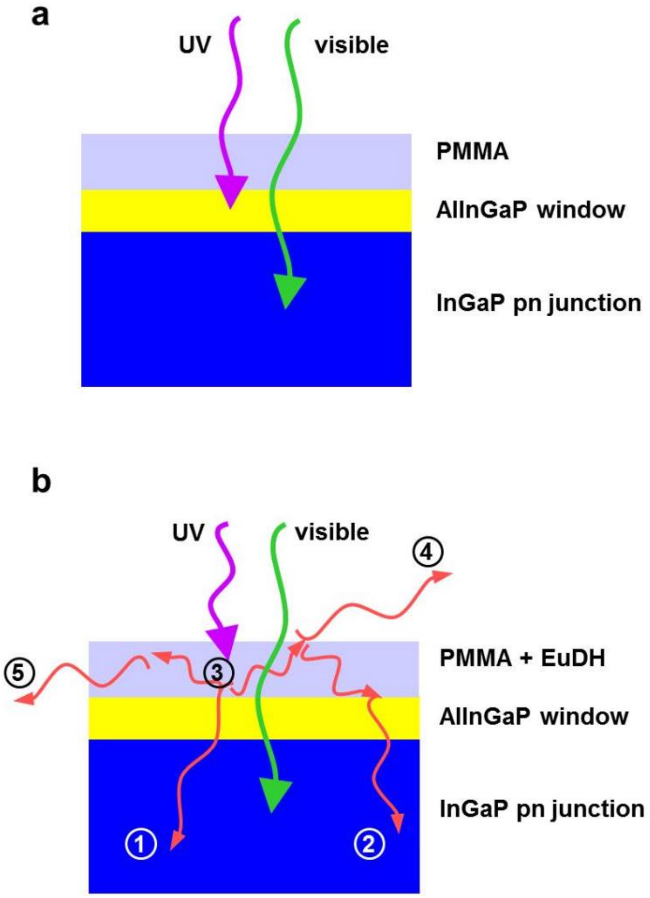

Figure 4.5 Cross sectional schematic illustrations of light responses for InGaP cells with different coatings: (a) a PMMA layer and (b) a PMMA + EuDH layer.

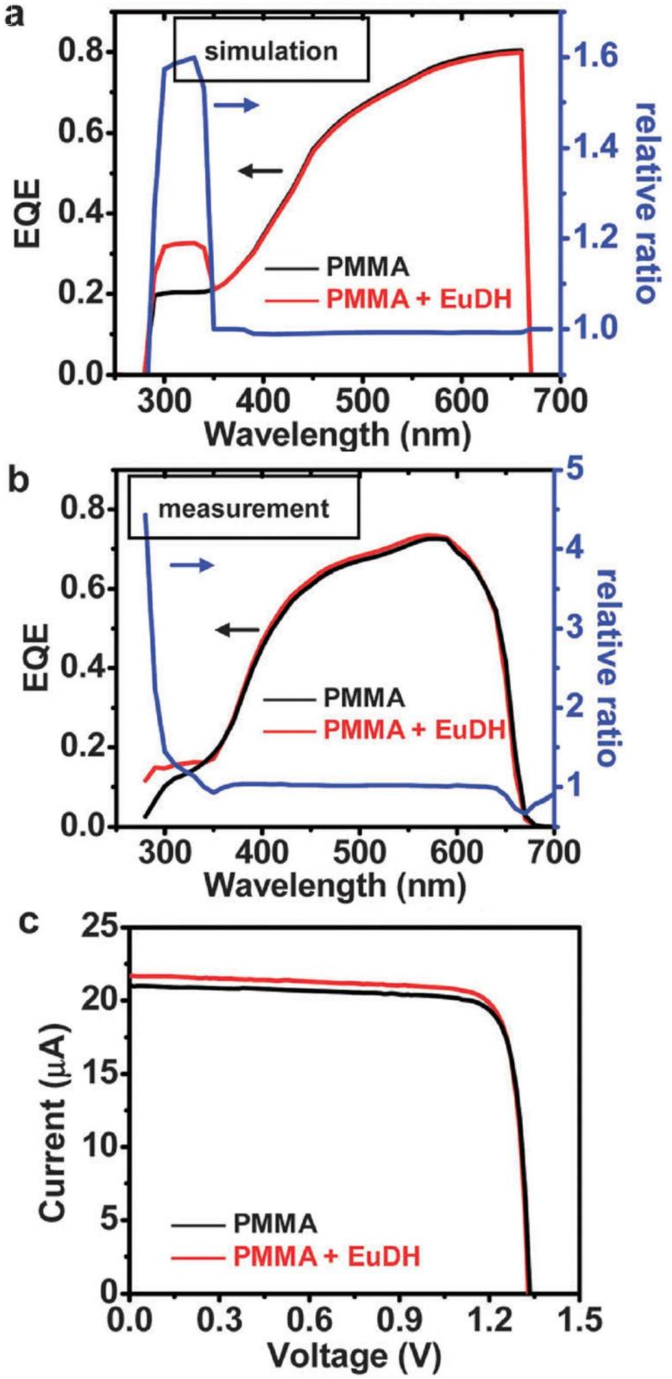

Figure 4.6 Performance of InGaP cells coated with PMMA (in black) and PMMA + EuDH (in red): (a) simulated EQE spectra and the relative ratio; (b) measured EQE spectra and the relative ratio; (c) measured current-voltage characteristics. The relative ratios between black and red curves are also indicated in a and b.

4.8 References

1. Polman, A. and H.A. Atwater, *Photonic design principles for ultrahigh-efficiency photovoltaics.* Nature Materials, 2012. **11**(3): p. 174-177.

2. Shockley, W. and H.J. Queisser, *DETAILED BALANCE LIMIT OF EFFICIENCY OF P-N JUNCTION SOLAR CELLS.* Journal of Applied Physics, 1961. **32**(3): p. 510-&.

3. Miller, O.D., E. Yablonovitch, and S.R. Kurtz, *Strong Internal and External Luminescence as Solar Cells Approach the Shockley-Queisser Limit.* Ieee Journal of Photovoltaics, 2012. **2**(3): p. 303-311.

4. Atwater, H.A. and A. Polman, *Plasmonics for improved photovoltaic devices.* Nature Materials, 2010. **9**(3): p. 205-213.

5. Sheng, X., L.Z. Broderick, and L.C. Kimerling, *Photonic crystal structures for light trapping in thin-film Si solar cells: Modeling, process and optimizations.* Optics Communications, 2014. **314**: p. 41-47.

6. Yablonovitch, E., *THERMODYNAMICS OF THE FLUORESCENT PLANAR CONCENTRATOR.* Journal of the Optical Society of America, 1980. **70**(11): p. 1362-1363.

7. Yu, Z.F., A. Raman, and S.H. Fan, *Fundamental limit of nanophotonic light trapping in solar cells.* Proceedings of the National Academy of Sciences of the United States of America, 2010. **107**(41): p. 17491-17496.

8. Green, M.A., et al., *Solar cell efficiency tables (version 42).* Progress in Photovoltaics, 2013. **21**(5): p. 827-837.

9. Geisz, J.F., et al., *Enhanced external radiative efficiency for 20.8% efficient single-junction GaInP solar cells.* Applied Physics Letters, 2013. **103**(4).

10. Steiner, M.A., et al., *Optical enhancement of the open-circuit voltage in high quality GaAs solar cells.* Journal of Applied Physics, 2013. **113**(12).

11. Zhao, J.H., A.H. Wang, and M.A. Green, *24 center dot 5% efficiency silicon PERT cells on MCZ substrates and 24 center dot 7% efficiency PERL cells on FZ substrates.* Progress in Photovoltaics, 1999. **7**(6): p. 471-474.

12. *Standard Tables for Reference Solar Spectral Irradiances: Direct Normal and Hemispherical on 37 degree Tilted Surface*, ASTMG173-03, Editor. 2005, ASTM International: West Conshohocken, Pennsylvania.

13. Zhao, J. and M.A. Green, *OPTIMIZED ANTIREFLECTION COATINGS FOR HIGH-EFFICIENCY SILICON SOLAR-CELLS.* Ieee Transactions on Electron Devices, 1991. **38**(8): p. 1925-1934.

14. Pern, F.J. and A.W. Czanderna, *CHARACTERIZATION OF ETHYLENE VINYL-ACETATE (EVA) ENCAPSULANT - EFFECTS OF THERMAL-PROCESSING AND WEATHERING DEGRADATION ON ITS DISCOLORATION.* Solar Energy Materials and Solar Cells, 1992. **25**(1-2): p. 3-23.

15. Ketola, B., et al. *Silicones for Photovoltaic Encapsulation*. in *23rd European Photovoltaic Solar Energy Conference*. 2008.

16. Huang, X.Y., et al., *Enhancing solar cell efficiency: the search for luminescent materials as spectral converters.* Chemical Society Reviews, 2013. **42**(1): p. 173-201.

17. Klampaftis, E., et al., *Enhancing the performance of solar cells via luminescent down-shifting of the incident spectrum: A review.* Solar Energy Materials and Solar Cells, 2009. **93**(8): p. 1182-1194.

18. Danos, L., et al., *Increased efficiencies on CdTe solar cells via luminescence down-shifting with excitation energy transfer between dyes.* Solar Energy Materials and Solar Cells, 2012. **98**: p. 486-490.

19. Le Donne, A., et al., *Encapsulating Eu3+ Complex Doped Layers to Improve Si-based Solar Cell Efficiency.* Progress in Photovoltaics, 2009. **17**(8): p. 519-525.

20. Li, Y.L., et al., *Increasing the power output of a CdTe solar cell via luminescent down shifting molecules with intramolecular charge transfer and aggregation-induced emission characteristics.* Energy & Environmental Science, 2013. **6**(10): p. 2907-2911.

21. Liu, J., et al., *Improving spectral response of monocrystalline silicon photovoltaic modules using high efficient luminescent down-shifting Eu3+ complexes.* Progress in Photovoltaics, 2013. **21**(4): p. 668-675.

22. McIntosh, K.R., et al., *Increase in External Quantum Efficiency of Encapsulated Silicon Solar Cells from a Luminescent Down-Shifting layer.* Progress in Photovoltaics, 2009. **17**(3): p. 191-197.

23. Yoon, J., et al., *GaAs photovoltaics and optoelectronics using releasable multilayer epitaxial assemblies.* Nature, 2010. **465**(7296): p. 329-U80.

24. Campo, A.d. and C. Greiner, *SU-8: A Photoresist for High-Aspect-Ratio and 3-D Submicron Lithography.* Journal of Micromechanics and Microengineering, 2007. **17**: p. 81-95.

25. Smy, T., S.K. Dew, and R.V. Joshi, *Modeling 3D effects of substrate topography on step coverage and film morphology of thin metal films.* Thin Solid Films, 2002. **415**(1–2): p. 32-45.

26. Moudam, O., et al., *Europium complexes with high total photoluminescence quantum yields in solution and in PMMA.* Chemical Communications, 2009(43): p. 6649-6651.

27. Kaushika, N.D. and K. Sumathy, *Solar transparent insulation materials: a review.* Renewable & Sustainable Energy Reviews, 2003. **7**(4): p. 317-351.

28. Kato, H., et al., *OPTICAL-PROPERTIES OF (ALXGA1-X)(0.5)IN0.5P QUATERNARY ALLOYS.* Japanese Journal of Applied Physics Part 1-Regular Papers Short Notes & Review Papers, 1994. **33**(1A): p. 186-192.

29. Liu, Y.M., Y. Sun, and A. Rockett, *A new simulation software of solar cells-wxAMPS.* Solar Energy Materials and Solar Cells, 2012. **98**: p. 124-128.

30. Sheng, X., et al., *Doubling the Power Output of Bifacial Thin-Film GaAs Solar Cells by Embedding Them in Luminescent Waveguides.* Advanced Energy Materials, 2013. **3**(8): p. 991-996.

31. http://www.ioffe.ru/SVA/NSM/Semicond/.

32. Palik, E., *Handbook of optical constants of solids*. 1998: Academic Press

33. Richards, B.S., *Luminescent layers for enhanced silicon solar cell performance: Down-conversion.* Solar Energy Materials and Solar Cells, 2006. **90**(9): p. 1189-1207.

34. Sukhovatkin, V., et al., *Colloidal Quantum-Dot Photodetectors Exploiting Multiexciton Generation.* Science, 2009. **324**(5934): p. 1542-1544.

35. *Technology Brief - Single Solar Cell*, A. Devices, Editor. 2013: Sunnyvale, CA.

Chapter 5

Future Directions with Spectrum Splitting and Other Photon Management Strategies

5.1 Abstract

This chapter outlines design principles for incorporating spectrum splitting with photovoltaic devices. Two spectrum splitting setups are proposed: one in which a prism/lens system is used to split and concentrate sunlight onto two adjacent cells and another that uses chromatic aberration to focus light onto two, mechanically stacked cells. Optical modeling is presented and preliminary results are discussed. This chapter ends with future directions towards light management that can be applied towards III-V photovoltaic devices. The optical modeling presented herein was performed by Junwen He using LightTools by Synopsis.

5.2 Introduction

Today's single-junction solar cells are capable of achieving conversion efficiencies of 28.8% under one sun and over 40% for multijunction devices under concentrated sunlight [1], as indicated by Figure 5.1. Thermodynamics has played an important role in assessing the limits of performance and being aided by advances in materials science and electrical engineering [2]. Table 5.1 lists the types of devices and their typical energy conversion efficiency ranges. (It should be noted that, when cells are assembled into a module, module efficiencies are ~5% lower (for one sun modules) and ~10% lower (for concentration modules). The reason for these differences is that the devices reported in Figure 5.1 are hero cells and there is some sample variance when fabricating devices. For concentrators, the optical elements employed in concentrator systems do not have optical efficiencies of 100%, so that is the main reason for discrepancies reported for lab-tested multijunction cells and real-world concentrator modules.)

Figure 5.2 details the loss mechanisms for a solar cell. The maximum efficiency achieved for a single-junction solar cell under one sun illumination is ~28% (shown in green). Dark blue and light blue bars to the right are the various entropy- and energy-related loss mechanisms, respectively. The main loss process in a solar cell is due to thermalization and/or lack of absorption. Thermalization losses occur when the light absorbed by the solar cell is well above the material's band gap. The excess energy is lost as heat as the electron-hole pairs thermalize to the material's band gap. Incomplete absorption occurs when light is below the band gap and, therefore, cannot be absorbed. These processes are outlined in the lower part of Figure 5.2. A common solution to overcome these challenges in industry is to use multijunction solar cells.

5.2.1 Multijunction Solar Cells

The concept of a multijunction solar cell has been around since the 1950s; the first mention of using multiple junctions was suggested in 1955 [3], just after the development of silicon solar cell technology. Multijunction technology known today was first studied in the 1980s beginning with InGaP/GaAs dual-junction devices that later evolved to studying triple-junction InGaP/InGaAs/Ge devices [4], as depicted in Figure 5.3. For excellent overviews of multijunction devices, readers are encouraged to review references [4-9]. Multijunction devices consist of compound semiconductor alloys with different band gaps and the different epi-layers that are often grown by varying the composition of ternary and quaternary alloys. As stated previously, these multilayer structures may be produced by either metal-organic chemical vapor deposition (MOCVD), liquid phase epitaxy (LPE), as well as molecular beam epitaxy (MBE). MOCVD growths have improved in quality over the years and have proven to achieve the best economics of growth that also provide for a high degree of crystal perfection, homogeneity, and interface control [10]. Because maximum efficiency is desired, a material possessing very low defects is necessary. As such, the lattice constants for all of these devices need to match in order to maintain the device's integrity. This imposes restrictions on the choice of materials– as well as ranges in the band gaps – that can be used. While there exists research into slightly lattice mismatched devices [11-13], the last sub-cell grown in these devices is the only portion that is mismatched.

There are further constraints when working with traditional multijunction devices. Current matching must be imposed, as shown from the current-voltage curve in Figure 5.3. Because the cells are connected in series, the current of the complete multijunction device is limited to the current produced by the sub-cell with the lowest current density. Additionally, multijunction devices connected in series are generally tolerant to only 2 – 4 band gaps. Increasing the number of sub-cells above this value can prove difficult and cause problems with the overall power output since the solar spectrum can change as the day progresses [4]. This altered spectrum throughout the day will change the power output of each sub-cell.

A different approach to working with traditional, monolithically grown multijunction cells is to work with separate junctions. These can allow for different materials with optimal band gaps and there are no constraints with series or parallel connection schemes. This also entails more complex assembly and – if not working in a mechanical stack configuration – requires optics for spectrum splitting.

5.2.2 Mechanically Stacked Solar Cells

Mechanically stacked multijunction solar cells consist of different band gaps stacked above each other, as shown in Figure 5.4. Table 5.2 details a comparison between mechanical and monolithically stacked solar cells. Mechanically stacked devices are discussed here since in the future directions section, one idea is proposed where InGaP and GaAs cells are mechanically stacked through transfer printing. The main problems that are associated with mechanically stacked solar cells are that the interfaces between each cell can cause reflections, so optical losses need to be minimized. This problem is overcome with anti-reflective coatings on each surface of each sub-cell. This technique originally involved bulky wafers of different band gaps stacked above each other [14-16], but more recent reports are using thin-film cells [17, 18]. A more recent mechanical stacking study looked into using a chalcogenide-based, index-matching material between sub-cell interfaces [19]. A triple-junction, thin-film (~ 10 μm thick) solar cell was transfer printed above a Ge subcell to achieve an energy conversion efficiency of ~43.5% at ~1100 suns under standard test conditions. The novel techniques and ideas employed in this worked could alleviate the higher costs traditionally associated with mechanical stacking.

5.2.3 Spectrum Splitting by Employing Optical Elements

An alternative approach over mechanical stacking or monolithically grown cells uses an optical element (or elements) to divide and concentrate the solar spectrum into different and unique spectral bands that are directed to an array of cells of different band gaps that are electronically independent of each other. Reports have looked into spectral splitting with holographic filters [20-22], dichroic mirrors with a concentrating lens [23-25], or dichroic mirrors that reflect the light to a series of cells [26]. Herein, two separate optical elements are modeled for splitting the solar spectrum by either using a prism/lens design or an aspheric lens to use chromatic aberration to split the solar spectrum.

Spectrum splitting overcomes two key energy loss mechanisms that are common in photovoltaics (PV) – thermalization losses and incomplete absorption of light. For a given semiconductor, upon absorption of light, an electron-hole pair is created that relaxes down to the band-edge of the semiconductor. As a consequence of this process, light with an energy of $E = \hbar\omega$ – that is, for light above the semiconductor's band gap – can only create a photo-voltage, V_{oc}, so that the mismatch energy, $E-qV_{oc}$, is lost to heat [2]. Furthermore, photons can be lost by incomplete absorption of the solar spectrum. These effects are particularly true for single junction devices. The proposed set-ups divide the spectrum into two different spectral bands that directs the light to two cells. Our proposed approaches do not require current matching or any of the integration challenges associated with traditional monolithic epitaxial designs. This aspect enables the use of a more diverse set of materials that can facilitate better photon management strategies.

For the two cases presented, the proposed designs have features that overcome the limitations of current monolithic multijunction cells to yield more robust designs. For our proof-of-concept designs, we use InGaP (band gap of ~1.9 eV) and GaAs (band gap of 1.43 eV) solar microcells. The first optical element we will be incorporating into this project is an aspheric lens that has a high degree of chromatic aberration. This chromatic aberration causes the light to have different focal points. These different focal points make it possible to direct the light onto each of the cells for optimal photon utilization. The other technique involves a prism/lens configuration where the prism disperses the light and the lens focuses the light. In this set up, the optical elements spread the light horizontally onto solar cells adjacent to each other.

These techniques will minimize thermalization losses and allow for better collection and utilization of the solar spectrum. This design is amendable to different and additional band gaps as well as different concentrations ratios, and can be fabricated into arrays for module-level electronic devices. The design is also extremely compact and ultra-portable, allowing for assimilation as a power source for portable electronic devices.

5.3 Materials and Methods

LightTools from Synopsis was used for the optical modeling. Solar cell measurements were performed on the solar simulator in a manner as described in Chapter 1. For the modeling with the prism/lens configuration, a CaF_2 equilateral dispersive prism (part number PS862; Thorlabs; minimum angle of deviation 31.6° at 633; Abbe number: 95.00) was studied along with an N-BK7 aspheric lens (part number AL7560-A; focal length = 60 mm; numerical aperature =0.619, anti-reflective coating from 350-700 nm). For the aspheric lens studies, the aspheric lens modeled was a precision aspheric lends (Edmund Optics; part number 67-250; diameter = 15.00 mm; numerical aperture = 0.83; effective focal length = 9.00 mm; material = N-SF5). The angle of incidence upon the optical element was maximized to allow for the greatest transmission and dispersion. The light entering each optical element was modeled after sunlight – which has a semi-angle of 0.25 degrees. Experimental measurements with the aspheric lens were performed using an ABET 2000 Class A solar simulator. The spectrometers used for the characterization were Avantes spectrometers [part numbers: ULS2048-USB2 (280-450 nm) and ULS2048x16-USB2 (380-1100 nm)]. Concentrator measurements for a GaAs solar cell are performed with the solar simulator discussed in Chapter 1 and calibrated using the procedures discussed in Chapter 1.

5.4 Results and Discussion

5.4.1 Prism/Lens Configuration

Figure 5.5a is an outline of the prism and lens configuration. Since InGaP has a band gap of 1.9 eV (~ 650 nm), this optical model is set up to have the cell absorb light just up to the band gap of InGaP and direct the remaining photons between 650 and 900 nm to GaAs. Because of how the light is spread, it is difficult to have a sharp cut-off at 650 nm. This set-up is amendable to different concentration ratios. In this case, this set-up has an aperture such that the geometrical concentration ratio (size of the lens relative to the size of the cell) is ~ 250 suns. The design is also ~ 100 mm from the top of the prism to the lower cells, making it very compact for a concentration module. In this design the InGaP and GaAs cells are adjacent to each other such that the light is spread to each cell for optimal light collection. The optical efficiency for this set-up is around 85%, as shown by the lens transmission data in Figure 5.5b, and can be set up to accompany additional cells of different band gaps. One potential problem with this design is that the intensity of the light is not evenly distributed across each cell. It is known that having non-uniform illumination across a solar cell can have an adverse effect on the device’s fill factor and, therefore, overall system performance. Another optical element can be integrated into the system, such as placing parabolic concentrators above each cell, in order to more uniformly distribute the light across each cell. This, of course, will add further complications to the overall system design.

Another method for spreading the light is to place a lens above a prism. In this instance, the prism is closer to the cells and the cost can be lowered since the prism used is smaller. This idea, however, is not practical, as shown in Figure 5.6a. When the light is focused to a point and passed through a prism, it nearly comes out as white light. When light is focused to a point, there is a decrease of translational entropy that must be compensated for somewhere in the system. Decreasing the areal “spread” of the light by focusing it to a point causes the distribution of angles of light to increase after passing through a lens – as shown in the illustration in Figure 5.6b. This phenomenon can be related to what is known as the concept of etendue. For a more rigorous discussion of etendue, readers are encouraged to review reference [27]. Briefly, the concept of etendue, for an apt analogy, can be associated with the second law of thermodynamics. Etendue can be best described as the characteristic property of light which links how spread out light is in both space and angle; these two features of light are inter-related. Modifying the distribution of light in space will modify its angular distribution and vice-versa. Because a prism is very sensitive to the angle of incident light, having a large distribution of angles enter the prism causes the light to refract in different spatial positions and, upon leaving the prism, come out as white light. For this reason having the lens as the first optical element is not practical. It is possible, however, to focus and disperse the light simultaneously with a single optical element – for example, by employing an aspheric lens.

5.4.2 Aspheric Lens

Figure 5.7a is a schematic illustration of a spectrum splitting design with an aspheric lens. The chromatic aberration from the lens causes the light to have different focal points. As such, it is possible to focus light from 400 – 650 nm to the top InGaP cell while the lower cell receives light after 650 nm. The optical element employed offers a geometric concentration ratio of approx. 260 suns with an optical efficiency of ~90% from 400 to 900 nm, as shown in Figure 5.7b. It should also be observed from Figure 5.7b that a significant portion of light after 650 nm passes through the InGaP cell. This is not too big of a problem as InGaP is transparent to light after 650 nm. The bottom contact, however, is composed of a 100 nm layer of GaAs which will absorb a small amount of this light. This problem is not too great of a problem as traditional multijunction devices use GaAs-based tunneling junctions which are 100 to 200 nm in thickness between the InGaP and GaAs sub-cells [1, 4, 6, 8]. Additionally, utilizing greater geometrical concentration ratios will make less of the light after 650 nm pass through the InGaP sub-cell.

The modeling performed assumes that the light entering the optical element is direct sunlight with a high degree of collimation; to be exact, the semi-angle of the light is ~0.25 degrees, which is consistent with the direct part of the solar spectrum. The solar simulator in our laboratory, unfortunately, produces light that is not as collimated as that from the direct spectrum of the sun. Figure 5.8 details how the optical element splits light based upon different degrees of collimation – ± 0.25°, ± 1.3°, and ± 4°. As can be seen, under a collimation of ± 4°, light is not effectively separated. This is the limitation of the solar simulator in our laboratory. Another simulator from the Atwater laboratory at Caltech offers a light source with a collimation of ± 1.3°. As is observed from this figure, a simulator with a collimation of ± 1.3° is adequate for demonstrating our proof-of-concept spectrum splitting device. The lens was tested under experimental conditions with a light source having ± 1.3° of collimation. An aperture was placed over the system (Figure 5.9a) and an optical fiber was placed over the device and a detector was mounted behind the lens; Section 5.3 goes into further details for this experimental setup. From Figure 5.9b, experiment agrees quite well with theory and the light is able to be adequately separated. More specifically, 1000 nm light is able to be separated from 400 nm light by 700 µm. Figure 5.9c shows the peak focal points from the data in Figure 5.9b and how experiment agrees with the modeled results. With this, it is possible to have the InGaP cell above a GaAs cell and focus the higher energy photons to the InGaP cell and the lower energy photons to the GaAs cell. This is another method of spectrum splitting with a solar concentrator device.

Another method for spectrum splitting would be to have the cells adjacent to each other in a similar manner to the prism and lens configuration. Figure 5.10a gives details on such a design. Here, a true color distribution of the light is presented and Figure 5.10b presents a plot of radiant intensities. As in the prism and lens configuration, adjacently spreading the light across an array of cells can cause the intensity of light to non-uniformly cover the surface of a cell. Parabolic concentrators may be used to overcome this challenge. The research path chosen for this project, however, is to mechanically stack InGaP and GaAs with a separation of ~ 1 mm and focus the light on the different sub cells with an aspheric lens – as outlined in Figure 5.7a.

5.4.3 GaAs under a 665 nm Long-Pass Filter

In order to assess the GaAs cell performance in this concentration system, a GaAs cell was tested with a 665 nm long-pass filter placed above the cell. Figure 5.11 details these results of the GaAs cell under 235 suns. Under 235 the suns the photocurrent is just over 12 mA. With the 665 nm long-pass filter above the cell, the photocurrent drops to just over 3 mA. The efficiency for the cell under the 665 long-pass filter is ~ 3.5%. Therefore, from these preliminary results the combined efficiency of an InGaP/GaAs system is ~ 14 %. If the fill factors were able to be maintained, the overall device efficiency could slightly over 15 %. These are raw efficiency values where the microcells do not have passivation or anti-reflection coatings. With anti-reflection coatings employed, this set up could be closer to 20 %. These are approximations for the mechanically stacked cell with an aspheric lens and serve as an estimate for real-world performance values.

5.5 Conclusions

This chapter has focused on the rationale for spectrum splitting and two unique spectrum splitting devices. The direction chosen is to place an aspheric lens above a mechanically stacked cell design. With the current device set up, efficiencies around 15 % are possible that can be improved to nearly 20 % with the implementation of anti-reflection coatings. This microcell module will use InGaP and GaAs cells, but the design is amendable to different, as well as additional, cells with different band gaps.

5.6 Future Directions

Transfer printing is very attractive technique for working with microcells in a spectrum splitting set up and the technique also has opportunities for application in mechanically stacked solar cells. Dual-junction InGaP/GaAs technology is a very mature technology with efficiencies under one sun approaching 32%. Even with such a mature technology, there exist possibilities to improve upon their key performance values. These dual-junction InGaP/GaAs cells typically exist as a monolithic stack. Better performance can be obtained with a mechanically stacked configuration. For a mechanically stacked InGaP/GaAs cell set, anti-reflection coatings would need to be deposited on the front and back surfaces of the InGaP cell and on the front surface of the GaAs cell. With thin-film cells this would be a very difficult (and potentially cost-prohibitive) process. There are methods which can be employed that can minimize the number of antireflective coatings. For example, by applying a thin adhesive layer (~ 230 nm) between the InGaP/GaAs cell interface (Figure 5.12a), no antireflective coatings are needed between the bottom InGaP face and the top surface of the GaAs cell. Figure 5.12a details an illustration of this mechanical stacking set up. No anti-reflection coatings are needed at this interface since the adhesive is sub-wavelength in thickness and can be tuned to minimize reflections between 650 and 900 nm (Figure 5.12b) – where the GaAs sub-cell absorbs light. An adhesive such as SU-8 should be adequate as it has the desirable optical properties – it is transparent in the visible – and the dielectric constant of SU-8 is large enough to permit this mechanical stack to operate with relatively large amounts of current before the onset dielectric breakdown [28]. Placing the layer of SU-8 at this interface can be a challenging task. The method adopted for preliminary studies uses detachment lithography [29]. By carefully spinning a thin layer of SU-8 onto PDMS stamp, the SU-8 can be transferred to the GaAs cell's surface. Other methods such as printing the ink, however, are available.

For these cells to be of practical use, they must be implemented in some sort of concentrator system. As such, a grid pattern must be applied to the surface which could interfere with the thin SU-8 film. Typically for concentration to ~1000 suns, grid fingers have metallization thicknesses on the order of 1 µm [8]. Therefore, this poses a problem with transfer printing the InGaP sub-cell above the GaAs sub-cell. There exist two options for overcoming this problem: (1) as outlined in Figure 5.12c, a wide-band gap material, such as AlInP (E_g ~ 2.3 eV), can be grown above the GaAs contacting layer. AlInP can be lattice matched to GaAs and is already used as the window layer for multijunction devices [4]. The light passing through the AlInP layer will be absorbed by the GaAs subcell – despite this AlInP layer being over 1 µm in thickness. Another potential remedy is to (2) have the InGaP cell be smaller in width than the top contact grid of the GaAs cell (Figure 5.12d). Depending on the level of concentration the cell is designed to tolerate, grid fingers can be hundreds of microns apart or down to only ~100 µm. It is feasible to fabricate InGaP cells with such dimensions and transfer print then onto the surface of the GaAs sub-cell. There is the issue with microcells of this small size having a high degree of edge recombination. As discussed previously, however, at the high-carrier injection limit – that is, when the amount of generated carriers is greater than the background dopant density of the material, the primary method of recombination becomes Auger recombination. In the high-carrier injection limit, sidewall recombination becomes less of an issue. As calculated by Algora and Diaz [30], a 0.1 mm^2 solar cell under 1000 sun concentration (Figure 5.12e) has great performance which suggests making devices of this size ideal for concentrator applications.

Another potential avenue to exploit with mechanically stacked InGaP/GaAs devices is to take advantage of their extremely high radiative efficiencies [31]. When InGaP/GaAs are in a monolithic stack, the light is emitted isotropically. Because all of the materials in the stack have similar indices of refraction, the light emitted in each sub-cell is not collected efficiently. This is also the case for the aforementioned mechanically stacked devices discussed above; there can be potential "cross-talk" for the emitted light between the InGaP and GaAs cells. That is, light emitted by the InGaP cell can go to the GaAs cell and light emitted from the GaAs can escape to the InGaP cell. An alternative strategy, as shown in Figure 5.12f, is to have a dielectric spacer layer between the cells to take advantage of total internal reflection. This spacer layer will be on the order of microns and the most ideal spacer material is air, but a photo-curable epoxy having a refractive index around 1.3 or 1.4 may also work. This mechanical stack configuration is substantially different from the other proposed methods discussed above as this spacer will be thicker than the wavelength of light. Anti-reflection coatings will need to be employed to minimize interface reflections, but the light emitted by each sub-cell will be trapped inside their respective cells leading to improved energy conversion efficiencies.

Another possibility to explore with mechanical stacking is to employ high-refractive index chalcogenides. As has already been discussed, a As_2Se_3 material at the interface between thin-film, mechanically stacked cells has achieved an energy conversion efficiency of 43.5% [19]. Finding chalcogendies with higher refractive indices (> 3) that are (semi-)transparent in the desired wavelength range open up new avenues for mechanical stacking. For example, a five junction solar cell proposed by Spectrolab (Figure 5.12g) needs to be wafer bonded together [7]. A chalcogenide material might be a much more attractive alternative to conventional, high-temperature wafer bonding. This type of five junction cell is just one possibility. The possibilities with the different materials and number of junctions are endless given suitable chalcogenide materials.

With all of these new technologies being able to take advantage of the repertoire of conventional materials, it should be feasible to have a solar cell that has an energy conversion efficiency that is greater than 50 % within the coming decade. What is very interesting is that transfer printing offers the ability for these solar cells to be bonded together at room temperature. There is plenty of room to explore solar cells with new and unconventional methods for improving energy conversion efficiency.

5.7 Figures and Tables

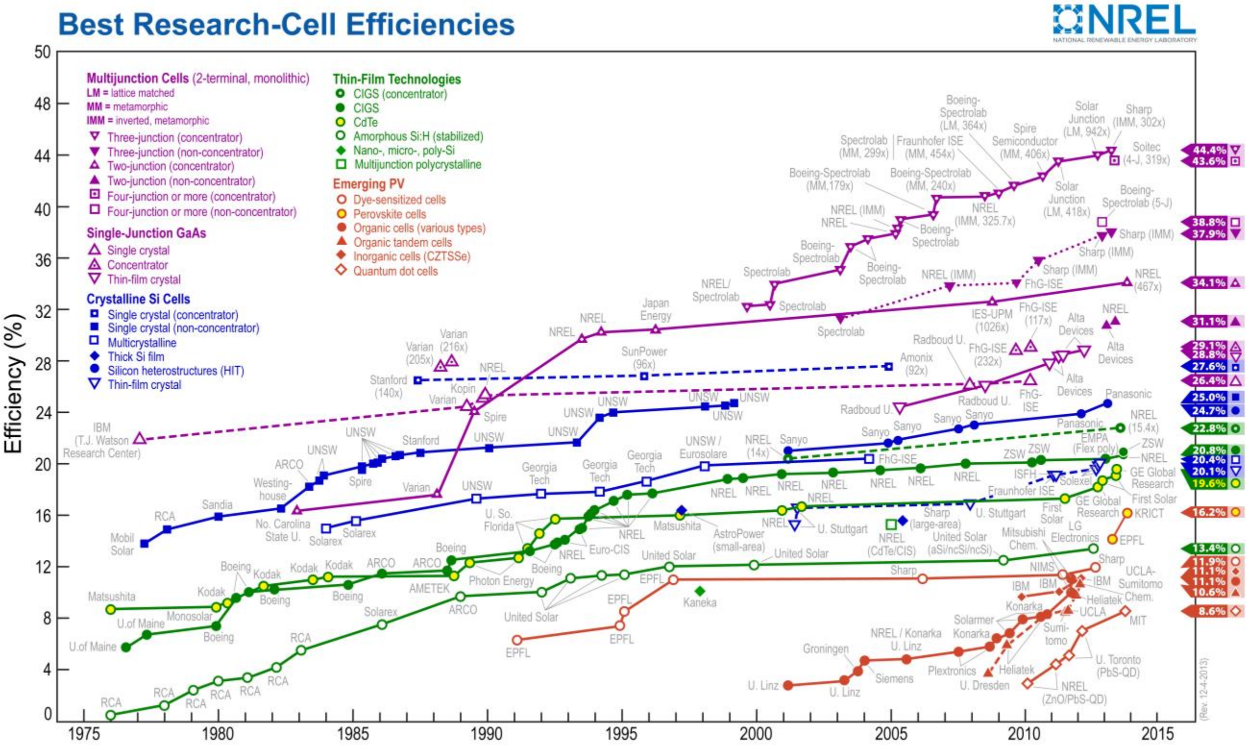

Figure 5.1 Chart published by NREL detailing key photovoltaic technologies and their record-setting efficiencies. Figure taken from reference [32].

Cell Efficiency Range	Type of Material
1-10%	Organic, Dye, and Nanostructured cells
6-12%	a-Si, micro-crystalline Si thin-film cells
10-20%	CIS, CIGS, CdTe thin-film cells
20-28%	Single junction high-performance Si and GaAs
36-45%	High-performance multijunction cells under concentration

Table 5.1 Typical solar cell efficiencies for several photovoltaic technologies that are available on the market. Note: when assembled into a module, module efficiencies are ~5% lower (for one sun modules) and ~10% lower (for concentration modules). Information is adapted from reference [32].

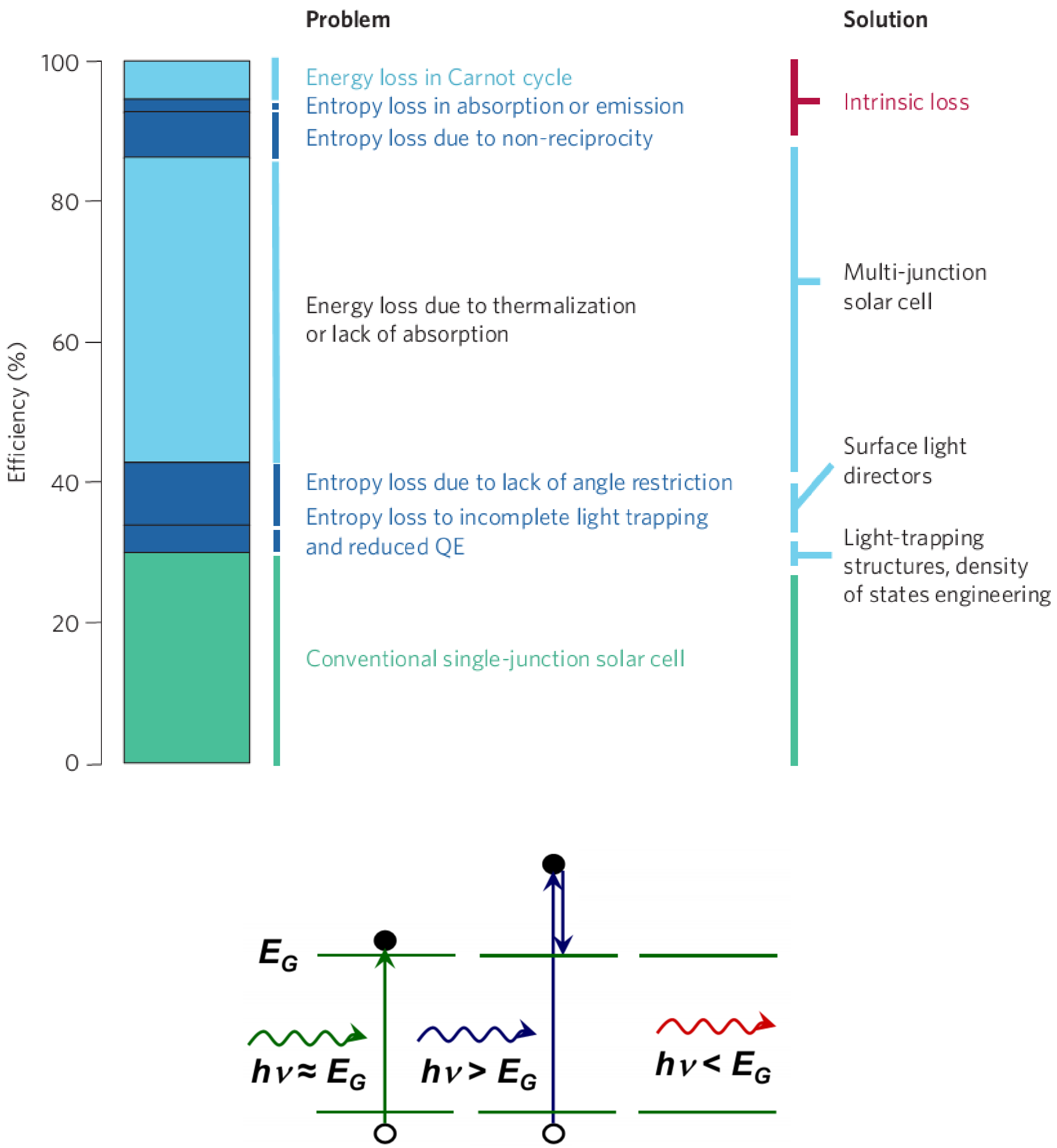

Figure 5.2 Outline of the various thermodynamic loss processes in a solar cell and the potential solutions. To date, the maximum efficiency achieved for a single junction solar cell at one sun illumination is ~28% (shown in green). Dark blue and light blue bars to the right are entropy-related and energy-related losses, respectively. The main energy loss process in a solar cell is due to thermalization and/or lack of absorption. The lower figure details these processes. Figure taken from reference [2].

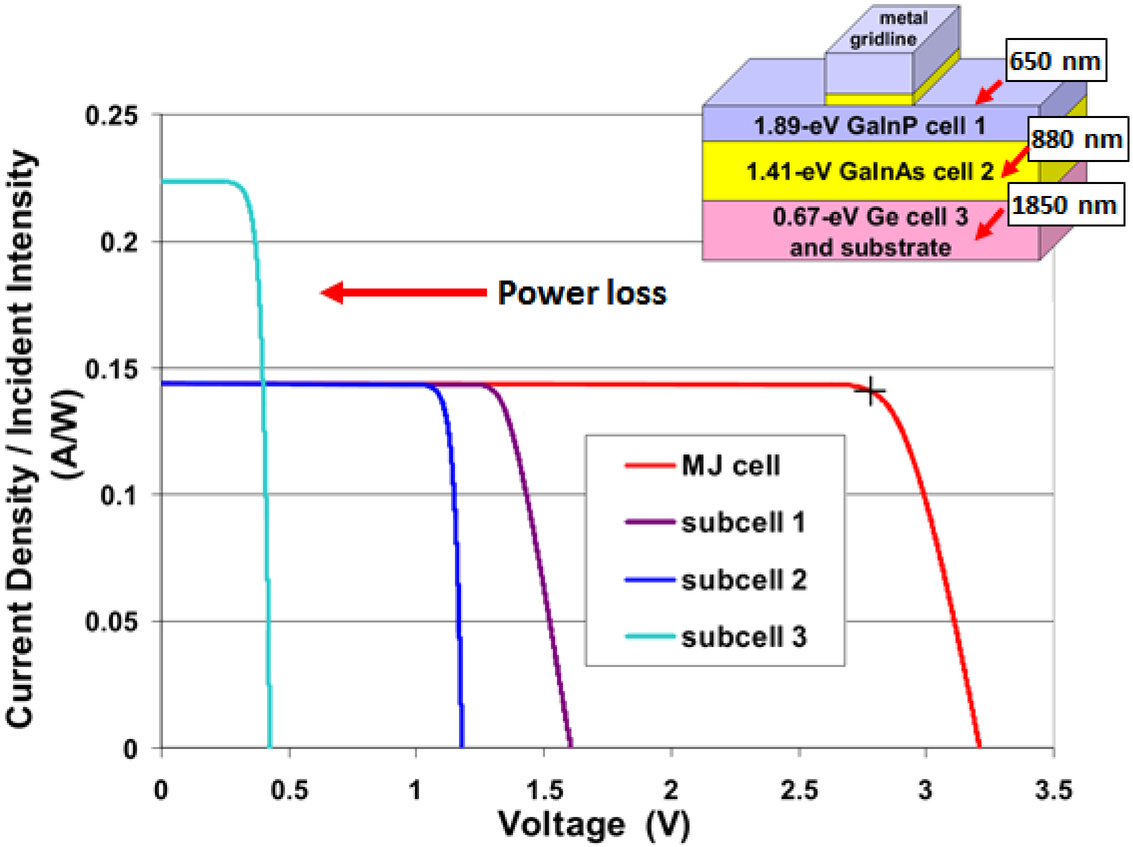

Figure 5.3 Image of InGaP/(In)GaAs/Ge triple-junction solar cell and I-V curves. The I-V curve demonstrates current-matching between sub-cells 1 and 3. The Ge sub-cell draws a greater current, but, there are power losses due to the cells being connected in series. Figure adapted from reference [7].

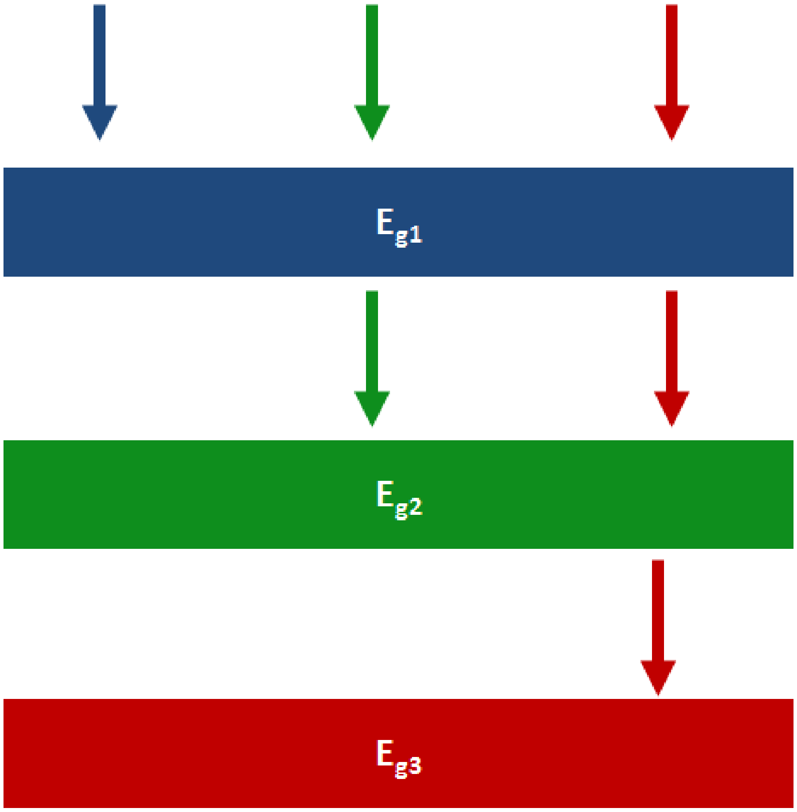

Figure 5.4. Diagram of a mechanically stacked solar cell with three band gaps partitioning the solar spectrum. The high-energy photons (blue) are absorbed by E_{g1}, the mid-energy photons (green) are absorbed by E_{g2}, and the low-energy photons (red) are absorbed by E_{g3}.

	Monolithically Stacked Cell	Mechanically Stacked Cell
cell processing	simple	complex
growth	complex criteria involving lattice matching	multiple growths for junctions; much easier
intermediate layer	tunneling junctions (slight optical losses)	bonding layers (need multiple anti-reflection coatings on each surface)
interconnection	2 terminals; series connected from tunnel junctions; need to employ current matching (limits to 2-4 band gaps for practical purposes)	potentially >2 termials; greater flexibility for interconnection
performance	spectral variation throughout the day can affect performance; current matching is imposed	insensitive to spectral variation
costs*	relatively lower efficiency; need tracking; only need on inverter	potential for higher efficiencies; need tracking; higher costs could come from multiple inverters and other balance of system components

Table 5.2. A comparison of monolithically and mechanically stacked multijunction solar cells. The table details the strengths and limitations of each technology. Information is adapted from references [17, 33].

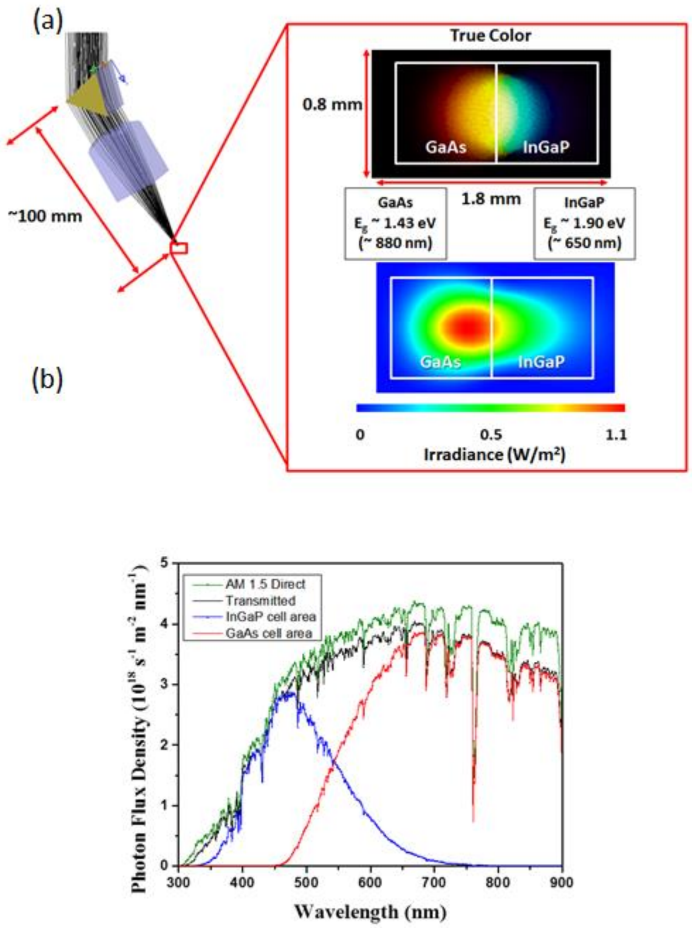

Figure 5.5 (a) Prism and lens configuration spreading light across the InGaP and GaAs cells that is (b) able to achieve an optical efficiency of close to 85% as shown in the lens transmission data. Part (b) describes which cell the light is directed towards with respect to the AM 1.5D solar spectrum.

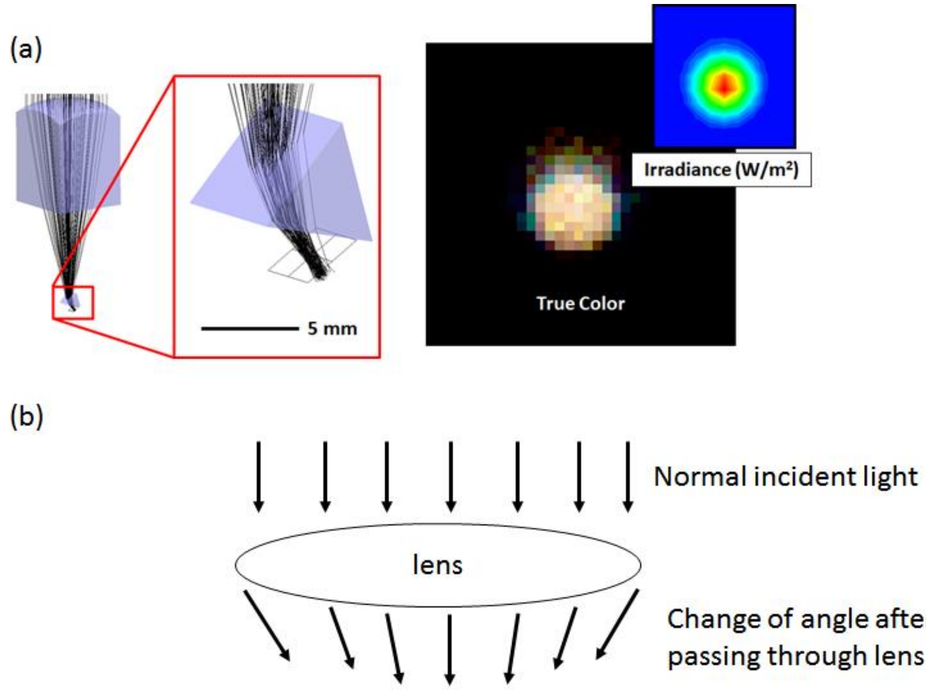

Figure 5.6 (a) A lens focusing light that is passed through a prism showing the true color and irradiance plots. Because of the concept of etendue, the light cannot be effectively refracted when traveling through the prism. Because the angle the light travels is modified when passing through the lens (b), this modifies how the prism can handle the light.

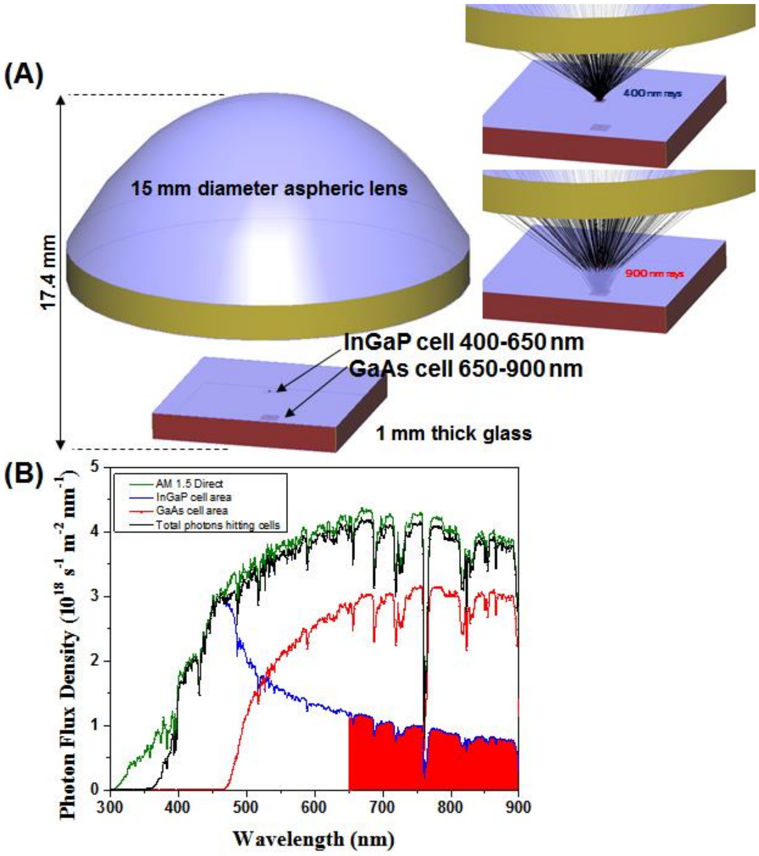

Figure 5.7 Outline of the spectral splitting aspheric lens along with the InGaP and GaAs cells (a). The total design has an overall height of ~17.4 mm. The inset to the right shows where light at 400 and 900 nm is focused. Photon flux density of the light that will project onto the InGaP and GaAs cells (b). The light highlighted in red is transmitted through the InGaP subcell and is collected by the GaAs sub-cell.

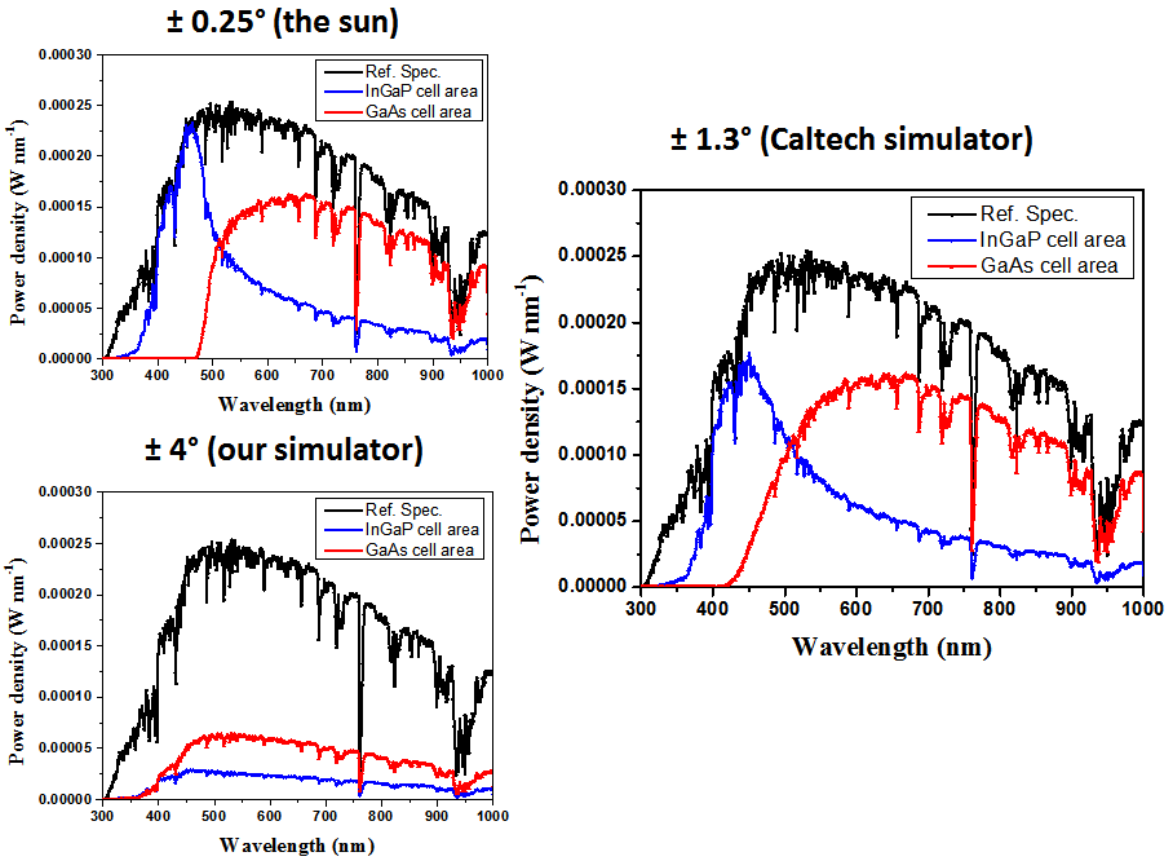

Figure 5.8 Light with varying degrees of collimation passing through the aspheric lens in Figure 5.7a is modeled. In the top left, the level of collimation from the sun (±0.25°) is depicted followed by ±1.3° (right) and ±4° (lower left). When the level of collimation increases, the separation of light is hindered such that at ±4° of collimation, white light is spread out from the lens.

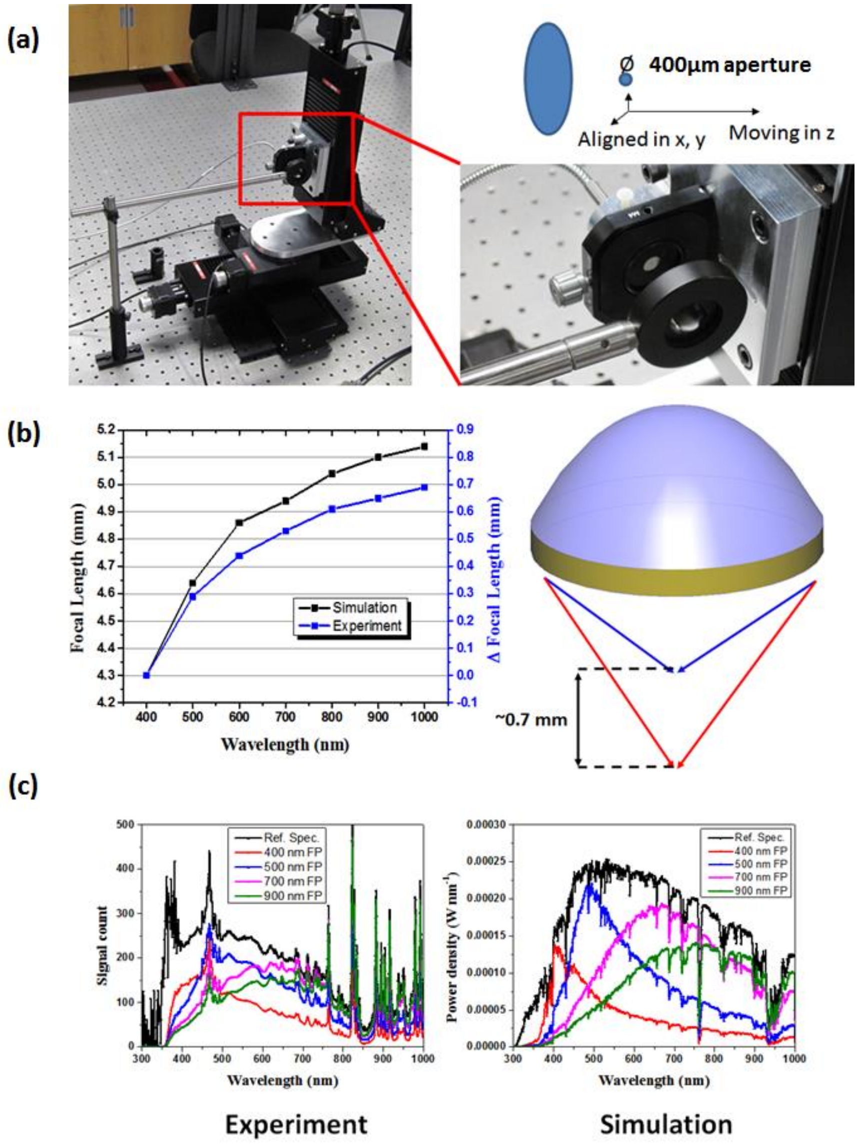

Figure 5.9 (a) Optical set up used for characterizing the aspheric lens. (b) The focal points for given wavelengths from experiment and theory. (c) Spectra of the focal points and the peak wavelengths from the solar simulator as compared to the modeled spectra.

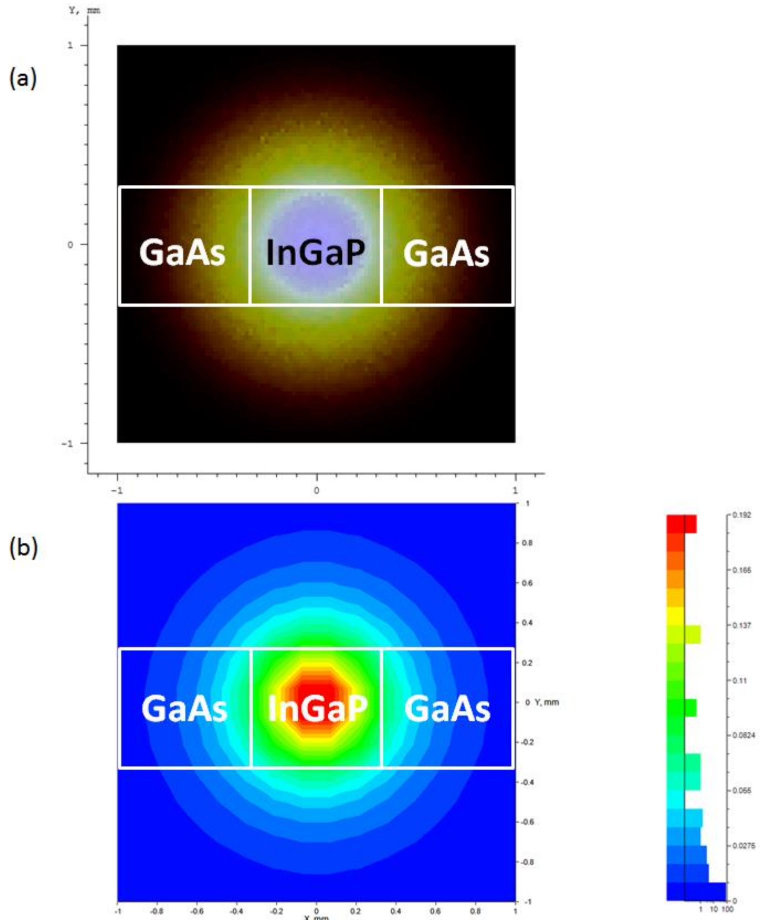

Figure 5.10 (a)True color diagram showing the various colors from 400 nm to 900 nm as the aspheric lens focuses light onto a surface. 400 nm light appears in the center and 900 nm light appears along the outer darkened edges. (b) Irradiance plots showing the distributions of intensities across the surface. The outline of the cells is to just show one potential set-up. There is more than one possible combination. The x-y axises for each graph are ± 1 mm.

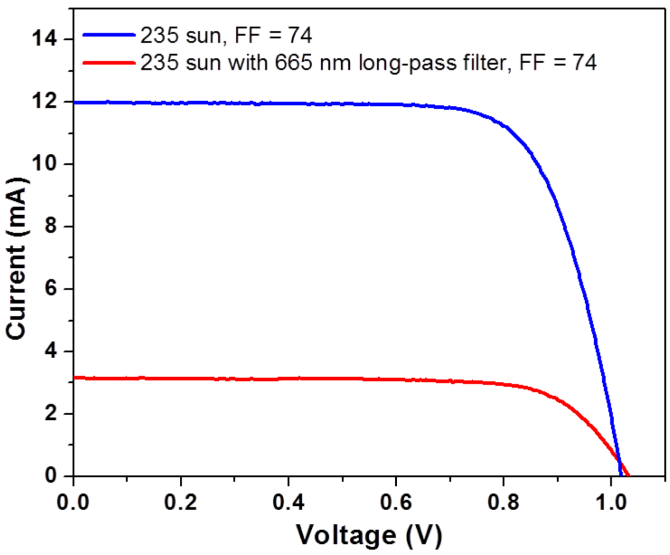

Figure 5.11 GaAs microcell at 235 sun concentration (blue line) and with a 665 nm long-pass filter (red line).

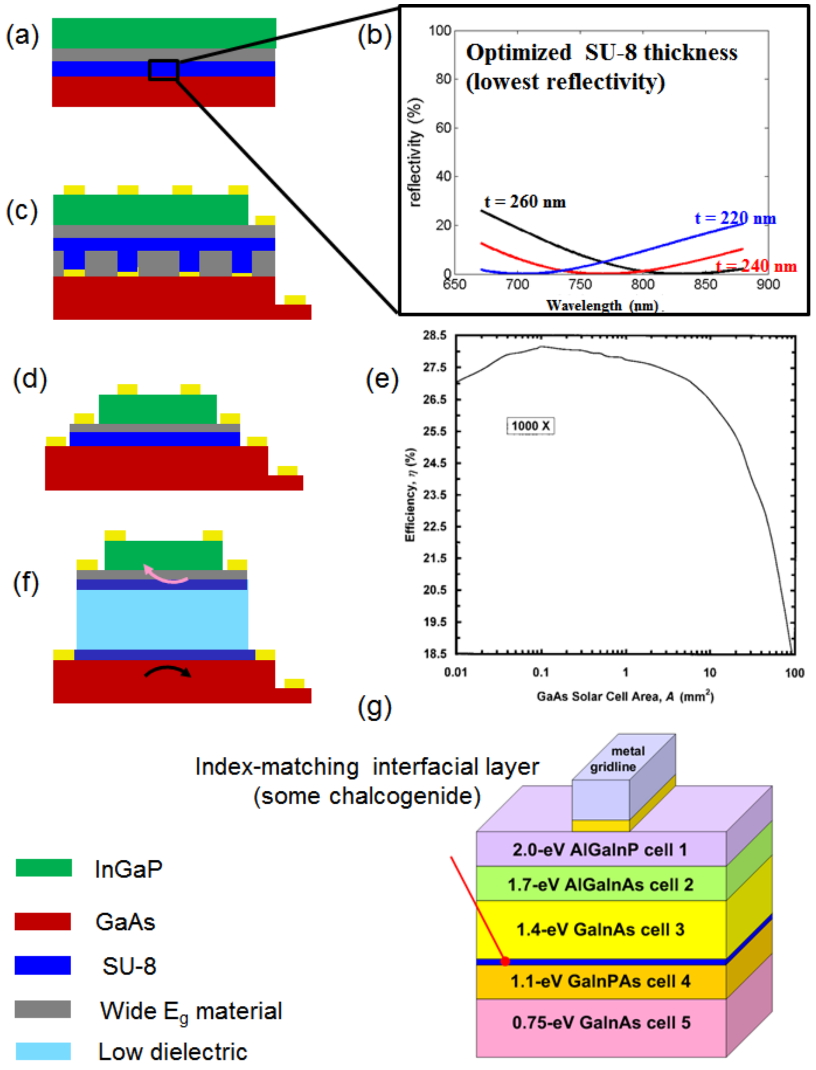

Figure 5.12 InGaP and GaAs solar cells mechanically stacked above each other with a thin film of SU-8 separating the two cells (a) with the thickness modeled showing the different reflectivity values (b). Since the SU-8 layer is on the order of 300 nm in thickness, in order to have a device that is tolerate to high concentration, contacts a micron in thickness are necessary. Different configurations are possible for high-concentration devices: (c) a wide band gap (grey) material can be used to offset the thick contacts or the upper cell can be roughly the same size as the grid fingers (d). Typically grid finger are spaced 100 µm apart for high concentration devices. Cells of this size can perform adequately as pictured by the figure in (e). Another possibility for an InGaP/GaAs mechanical stack is to place anti-reflective coatings on the top cell's lower surface and the upper cell's front surface and have a low refractive index material between them such that the radiated light is more effectively collected (f). Using an index-matching chalcogenide can also be used to transfer print cells with different lattice constants together such that ultra-high efficiencies are achieved (g). The figures in (e) and (g) are from references [7, 34].

5.8 References

1. Green, M.A., et al., *Solar cell efficiency tables (version 43).* Progress in Photovoltaics, 2014. **22**(1): p. 1-9.

2. Polman, A. and H.A. Atwater, *Photonic design principles for ultrahigh-efficiency photovoltaics.* Nature Materials, 2012. **11**(3): p. 174-177.

3. Jackson, E.D., *Trans. Conf. On the Use of Solar Energy*. Vol. 5. 1955, Tuscon, AZ: U. of Arizona Press.

4. Luque, A. and S. Hegedus, eds. *Handbook of Photovoltaic Science and Engineering -- 2nd Ed.* 2011, John Wiley & Sons: West Sussex.

5. Shahrjerdi, D., et al., *High-Efficiency Thin-Film InGaP/(In)GaAs/Ge Multijunction Solar Cells Enabled by Controlled Spalling Technology*. 2012 38th Ieee Photovoltaic Specialists Conference. 2012, New York: Ieee. 974-977.

6. Chiu, P., et al., *InGaP/GaAs/InGaAs Triple Junction Concentrators Using Bi-Facial Epigrowth*, in *High and Low Concentrator Systems for Solar Electric Applications V*, L.E. Greene and R.A. Sherif, Editors. 2010, Spie-Int Soc Optical Engineering: Bellingham.

7. King, R.R. *Raising the Efficiency Ceiling on Multijunction Solar Cells*. in *Stanford Photonics Research Center Symposium*. 2009. Stanford, CA.

8. Cotal, H., et al., *III-V multijunction solar cells for concentrating photovoltaics.* Energy & Environmental Science, 2009. **2**(2): p. 174-192.

9. Karam, N.H., et al., *Recent developments in high-efficiency Ga0.5In0.5P/GaAs/Ge dual- and triple-junction solar cells: steps to next-generation PV cells.* Solar Energy Materials and Solar Cells, 2001. **66**(1-4): p. 453-466.

10. Luque, A. and V.M. Andreev, eds. *Concentrator Photovoltaics*. Spriner Series in optical sciences. 2007, Springer.

11. Geisz, J.F., et al., *40.8% efficient inverted triple-junction solar cell with two independently metamorphic junctions.* Applied Physics Letters, 2008. **93**(12).

12. Geisz, J.F., et al., *INVERTED GaInP/(In)GaAs/InGaAs TRIPLE-JUNCTION SOLAR CELLS WITH LOW-STRESS METAMORPHIC BOTTOM JUNCTIONS*, in *Pvsc: 2008 33rd Ieee Photovoltaic Specialists Conference, Vols 1-4*. 2008, Ieee: New York. p. 466-470.

13. Wanlass, M.W., et al., *Lattice-mismatched approaches for high-performance, III-V photovoltaic energy converters*, in *Conference Record of the Thirty-First IEEE Photovoltaic Specialists Conference - 2005*. 2005, Ieee: New York. p. 530-535.

14. Chung, B.C., et al., *25.2-PERCENT EFFICIENCY (1-SUN, AIR MASS-0) ALGAAS/GAAS/INGAASP 3-JUNCTION, 2-TERMINAL SOLAR-CELL.* Applied Physics Letters, 1992. **60**(14): p. 1691-1693.

15. Takamoto, T., et al., *InGaP/GaAs and InGaAs mechanically-stacked triple-junction solar cells*, in *Conference Record of the Twenty Sixth Ieee Photovoltaic Specialists Conference - 1997*. 1997, Ieee: New York. p. 1031-1034.

16. Bett, A.W., et al. *Development of high-efficiency mechanically stacked GaInP/GaInAs-GaSb triple-junction concentrator solar cells*. in *Proceedings of the 17st European Photovoltaic Solar Energy Conference and Exhibition*. 2001. Munich.

17. Zhao, L., et al., *Novel Mechanically StackedMulti-junction Solar Cells Applying Ultra-thin III-V Cells and Wafer Based Germanium Cell.* ECS Transactions, 2010. **27**(1): p. 1123-1128.

18. Zhao, L., *High Efficiency Mechanically Stacked Multi-junction Solar Cells for Concentrator Photovoltaics*, in *DEPARTEMENT ELEKTROTECHNIEK*. 2011, Katholieke Universiteit Leuven: Heverlee, Belgium. p. 235.

19. Sheng, X., et al., *Printing-based assembly of quadruple junction, four-terminal microscale solar cells and their use in high-efficiency modules* Accepted in Nature Materials, 2014.

20. Frohlich, K., et al., *DEVELOPMENT AND FABRICATION OF A HYBRID HOLOGRAPHIC SOLAR CONCENTRATOR FOR CONCURRENT GENERATION OF ELECTRICITY AND THERMAL UTILIZATION*. Optical Materials Technology for Energy Efficiency and Solar Energy Conversion Xii, ed. C.M. Lampert. Vol. 2017. 1993. 311-319.

21. Ranjan, R., et al., *Use of holographic lenses recorded in dichromated gelatin film for PV concentrator applications to minimize solar tracking*. Energy Problems and Environmental Engineering, ed. L. Perlovsky, et al. 2009, Athens: World Scientific and Engineering Acad and Soc. 49-52.

22. Kumar, A., et al., *Analysis of Design Parameters for Wavelength Selective Holographic Solar Concentrators*, in *Pvsc: 2008 33rd Ieee Photovoltaic Specialists Conference, Vols 1-4*. 2008, Ieee: New York. p. 318-321.

23. Barnett, A., et al., *50% efficient solar cell architectures and designs*. Conference Record of the 2006 IEEE 4th World Conference on Photovoltaic Energy Conversion, Vols 1 and 2. 2006, New York: Ieee. 2560-2564.

24. Barnett, A., D. Kirkpatrick, and C. Honsberg, *Very high efficiency solar cells - art. no. 63380N*, in *Nonimaging Optics and Efficient Illumination Systems III*, R. Winston and P. Benitez, Editors. 2006, Spie-Int Soc Optical Engineering: Bellingham. p. N3380-N3380.

25. Barnett, A., et al., *Very High Efficiency Solar Cell Modules.* Progress in Photovoltaics, 2009. **17**(1): p. 75-83.

26. Mitchell, B., et al., *Four-junction spectral beam-splitting photovoltaic receiver with high optical efficiency.* Progress in Photovoltaics: Research and Applications, 2011. **19**(1): p. 61-72.

27. Winston, R., J.C. Minano, and P. Benitez, *Non-Imaging Optics*. 2005, Burlington, MA: Elsevier Academic Press.

28. *Permanent Epoxy Photoresist for Dielectrics in Organic TFT Back-Planes*. 2014; Available from: microchem.com/Appl-PermEpoxInterLayer.htm.

29. Yeom, J. and M.A. Shannon, *Detachment Lithography of Photosensitive Polymers: A Route to Fabricating Three-Dimensional Structures.* Advanced Functional Materials, 2010. **20**(2): p. 289-295.

30. Algora, C. and V. Díaz, *Influence of series resistance on guidelines for manufacture of concentrator p-on-n GaAs solar cells.* Progress in Photovoltaics: Research and Applications, 2000. **8**(2): p. 211-225.

31. Green, M.A., *Radiative efficiency of state-of-the-art photovoltaic cells.* Progress in Photovoltaics: Research and Applications, 2012. **20**(4): p. 472-476.

32. *Best Research-Cell Efficiencies*. 2014; Available from: http://www.nrel.gov/ncpv/images/efficiency_chart.jpg.

33. Rockett, A.A., *Photovoltaics: The Engineering, Technology and Application of Solar Cells*. 2010.

34. Algora, C. and V. Diaz, *Influence of series resistance on guidelines for manufacture of concentrator p-on-n GaAs solar cells.* Progress in Photovoltaics, 2000. **8**(2): p. 211-225.